Large Eddy Simulation of Labyrinth Seals and Rib Shapes for Internal Cooling Passages

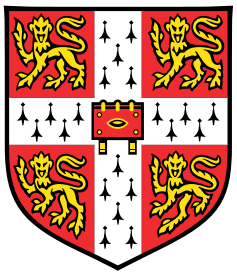

Yushuang Dai

Department of Engineering
University of Cambridge

This dissertation is submitted for the degree of
Doctor of Philosophy

Queens' College

February 2018

I would like to dedicate this thesis to my loving parents.

Declaration

The work presented in this thesis was conducted in the Department of Engineering, University of Cambridge, under the supervision of Professor P. G. Tucker. I declare that except where specific reference is made to the work of others, the contents of this thesis are original and have not been submitted in whole or in part for consideration for any other degree or qualification in this, or any other university. This thesis is my own work and contains nothing which is the outcome of work done in collaboration with others, except as specified in the text and Acknowledgements. This thesis contains fewer than 45,000 words including appendices, bibliography, footnotes, tables and equations and has around 100 figures.

Yushuang Dai
February 2018

Acknowledgements

First and foremost, I want to express my utmost thanks to my supervisor, Professor Paul Tucker, for providing me with the opportunity of joining his group and also for his professional guidance, unstinting patience, and constant support. I consider myself fortunate to have had such a supervisor.

Special thanks to Dr. James Tyacke, who has provided me a great deal of helpful assistance and support during all these years. Whenever I found problems to be insurmountable, my questions were always answered with patient explanation. I would also like to thank Dr. Rob Watson for his guidance on the optimisation design of labyrinth seals and Dr. Adam Preece for his help with the *IBM* implementation. Also, thanks to the members of our research group.

Finally, I would like to thank my wonderful family for their endless support and encouragement during the course of this study. I would also like to thank my friends, Fong, Janny, Mingfei, Qian and Qiyu, for all the emotional support, entertainment, and caring they provided.

This research has been funded by *CSC* (China Scholarship Council), for which I am most grateful.

Abstract

The turbine is one of the key components in gas turbine engines. To prevent the turbine blades from being badly damaged by their harsh working environment, it is necessary to keep them cool. This can be achieved by enhancement of the heat transfer performance through internal cooling passages. However, the large quantity of flow within this internal cycle inevitably results in mass flow loss, which is a major source of loss in turbomachinery. Therefore labyrinth seals are also investigated in this study, attempting to reduce the flow leakage and further increase the turbine efficiency.

Large Eddy Simulation (*LES*) is used for its capability to capture the complex unsteady flow features in this study. Different rib shapes in a fully developed ribbed channel are investigated, aiming to improve the heat transfer performance. An immersed boundary method (*IBM*) is used with *LES* to generate complex geometries. With the use of *IBM*, the range of geometries can be represented on a background Cartesian grid.

To obtain the best sealing performance, an investigation is undertaken into the possibility of optimising labyrinth seal planforms using a genetic algorithm (*GA*). By making use of the large number of populations, a much faster calculation can be achieved toward the objective function. Three hundred *LES* calculations are carried out, and an optimised design is generated that maximises the sealing effectiveness. The optimised design shows a leakage reduction of about 27.6% compared to the baseline geometry.

The optimisation process employing a *GA* will be continued. It is expected that automated optimisation as presented will become increasingly important in the design process of future turbomachines, particularly for flows with strong parameter interactions, with an aim to further improve the overall efficiency of gas turbines.

Table of contents

List of figures

List of tables

Nomenclature

Latin Symbols

c_k, c_ε	Yoshizawa constant
c_p	Specific heat capacity, $J/(kg \cdot K)$
c_s	Smagorinsky constant
d	Groove depth, m
D_h	Hydraulic diameter, m
e	Rib height, m
H_1, H_2, H_3	Rib geometrical parameters, m
k	Thermal conductivity, m^2/s^2
L	Seal width, m
L_R	Reattachment length, m
l	Groove width, m
l_I	Integral length scale
n	Number of grooves
Nu	Nusselt number, $Nu = \frac{q''}{T_s - T_b} \frac{D_h}{k}$
p	Instantaneous static pressure, Pa
p'	Fluctuating component of static pressure, Pa
P	Mean static pressure, Pa

PR	Pressure ratio
P_{in}	Intet pressure, Pa
P_R	Rib pitch, m
Pr	Prandtl number
Pr_t	Turbulent prandtl number
q''	Heat flux, W/m^2
R	Radial fraction of cavity height
R_f	Correlation coefficient
R_r	Rotor radius, m
r_1, r_2	Rib radius, m
Re	Reynolds number
Re_a	Axial Reynolds number
Re_r	Rotational Reynolds number
S_{ij}	Strain rate tensor, s^{-1}
T	Temperature, K
T_b	Bulk temperature, K
T_{in}	Turbine inlet temperature, K
T_{out}	Turbine outlet temperature, K
T_s	Wall temperature, K
t	Time, s
t^*	Dimensionless time step
u, v, w	Velocity components in x, y, and z directions, m/s
u_i'	Fluctuating component of velocity in direction x_i, m/s
$\overline{u_i'u_j'}$	Reynolds stress tensor, m^2/s^2

v_r	Rotational speed, m/s
x	Streamwise direction
y^+	Non-Dimensional Wall Distance, $\rho y u_\tau/\mu$

Greek Symbols

α	Under-relaxation factor
Δ	Filter width, m
δ	Seal clearance, m
δ_s	Shear layer thickness, m
Δt	Time step
ε	Dissipation rate of turbulent kinetic energy, m^2/s^3
η	Heat transfer performance, $(Nu/Nu_0)/(f/f_0)^{1/3}$
κ	von Karman constant
μ	Dynamic viscosity, $kg/(m \cdot s)$
μ_t	Turbulent dynamic viscosity, $kg/(m \cdot s)$
ν	Kinematic viscosity, m^2/s
ν_t	Turbulent kinematic viscosity, m^2/s
ϕ	Flow property
ρ	Density, kg/m^3
τ_{ij}	Stress tensor
τ_w	Wall shear stress, Pa
θ	Tooth inclination angle, $^\circ$
Ω	Vorticity magnitude

Acronyms and Initials

ANN	Artificial neural network

CDS	Central differencing scheme
CFD	Computational Fluid Dynamics
CFL	Courant-Friedrichs-Lewy
CPU	Central Processing Unit
DES	Detached Eddy Simulation
DNS	Direct Numerical Simulation
GA	Genetic algorithm
HI	Holographic interferometry
IBM	Immersed boundary method
LANS	Lagrangian Averaged Navier-Stokes
LCT	Liquid crystal thermography
LDV	Laser Doppler velocimetry
LES	Large Eddy Simulation
RANS	Reynolds-Averaged Navier-Stokes
SA	Simulated annealing
SFC	Specific Fuel Consumption
SGS	Subgrid scale
TI	Turbulent intensity
TKE	Turbulent kinetic energy
ZLES	Zonal Large Eddy Simulation

Superscripts

$'$	Correction or fluctuation value
$\overline{(\ )}$	Time averaged value
$\hat{}$	Filtered value

Subscripts

E	East nodal value
e	East face value
N	North nodal value
n	North face value
P	Central point value
S	South nodal value
s	South face value
W	West nodal value
w	West face value

Other Symbols

$< \quad >$	Averaged quantities

Chapter 1

Introduction

1.1 Background

Gas turbines have been used extensively in modern aircraft and also for the generation of power. The overall efficiency of turbine engines is strongly dependent on its components, which are exposed to a high pressure and high temperature operating environment. In 2008, the turbine inlet temperature in advanced engines reached $2400K$. Operating at this harsh environment, the performance of turbine blades is highly deteriorated. Thus, turbine blades must be cooled in order to operate in a proper environment, and to extend their durability.

The internal cooling system is used in the turbine blades to promote rapid heat transfer between the blade surfaces and to prevent them from reaching dangerously high temperatures. However, this internal cooling system requires large quantity and rate of flow, which inevitably results in loss of mass flow through the cycle. Thus, efforts are needed to control the leakage and keep it to a minimum. Labyrinth seals are the most typical sealing technologies. They operate within the internal cooling system and are used to increase the turbine efficiency by reducing the flow leakage. Figure 1.1 shows the internal cooling system and labyrinth seals in a modern bypass engine section.

1.1.1 Internal Cooling Passages

The ideal behaviour of a gas turbine is described by the thermodynamic Joule-Brayton cycle. Figure 1.2 shows the $T-s$ diagram for the Joule-Brayton cycle. The efficiency of this cycle is determined by the ratio of temperatures at engine and compressor inlets, as expressed by the equation $\eta_{JOULE} = 1-(T_1/T_2)$. The highest temperature in the cycle comes at combustion chamber exit T_3 (equal to turbine inlet temperature in the ideal cycle). Although the efficiency of the ideal Joule cycle is independent of T_3, this is no longer the

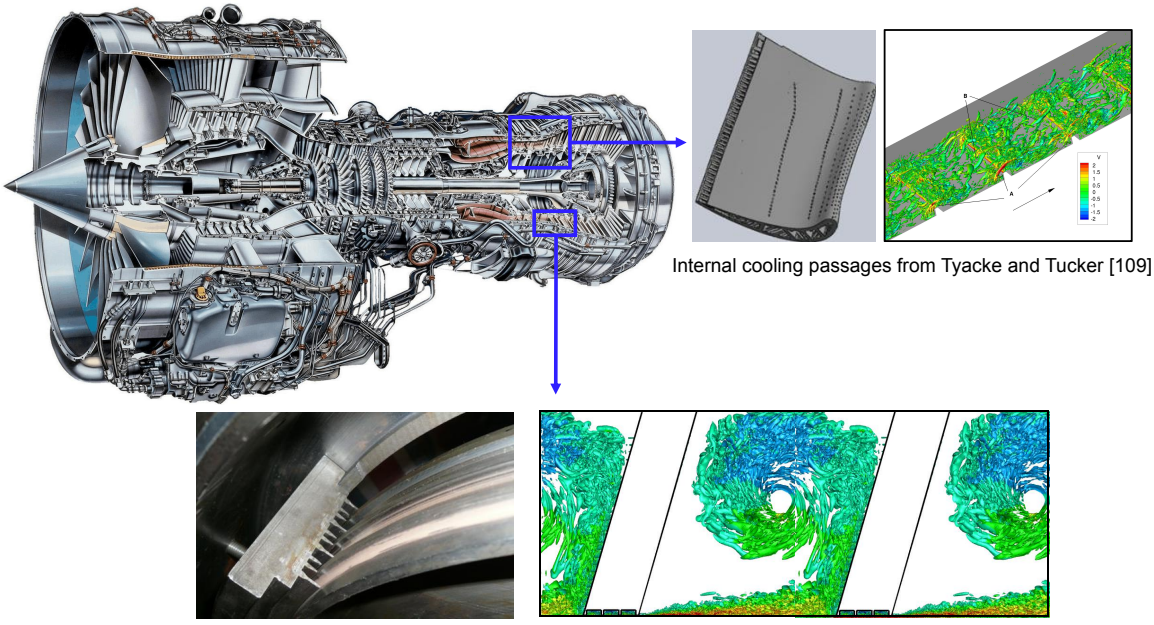

Fig. 1.1 Internal cooling system and labyrinth seals shown in a modern bypass engine section.

case when account is taken of losses in the turbomachinery. In this case, both the efficiency and specific thrust can be increased by increasing the turbine inlet temperature. Thus the engine efficiency would be improved through increasing the inlet temperature. The pursuit of better engine performance requires the turbine blades to withstand huge temperatures. To confront the thermal challenges, advanced cooling technology is developed to reduce the blade temperature.

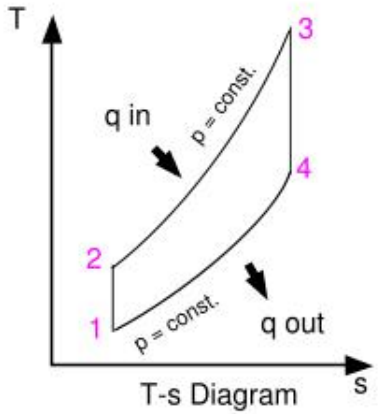

Fig. 1.2 Temperature-entropy plot of the Joule/Brayton ideal gas turbine cycle.

Figure 1.3 shows the historical trends of increasing turbine inlet temperature and how the turbine blades have been better designed to withstand the temperature. Modern turbine

blades apply a composite cooling system, incorporating impingement cooling, film cooling and convection cooling, as shown in Figure 1.4. The cooling air passes through a circuit of serpentine passages. Turbulence is generated after passing through ribs and pin fins. The air then exits through film cooling holes at the surface of the blade. This study focuses on investigating the convection cooling in the internal cooling system. Convection cooling enhances heat transfer by casting internal passages with ribs into the turbine blades, as shown in Figure 1.4. When air passes through the ribbed internal passages, the original laminar sub-layer is broken and then turbulence is created due to flow separation and reattachment from the ribs. This complex phenomenon helps to enhance the heat transfer, decrease the temperature and further to prevent breakdown. The separating and reattaching shear layers behind the ribs make the turbulent and thermal field extremely complex. These complex features of flow cause a big challenge to the numerical prediction of this type of flow. Therefore, accurate prediction of turbulent flow and heat transfer characteristics is necessary to cool the blades effectively.

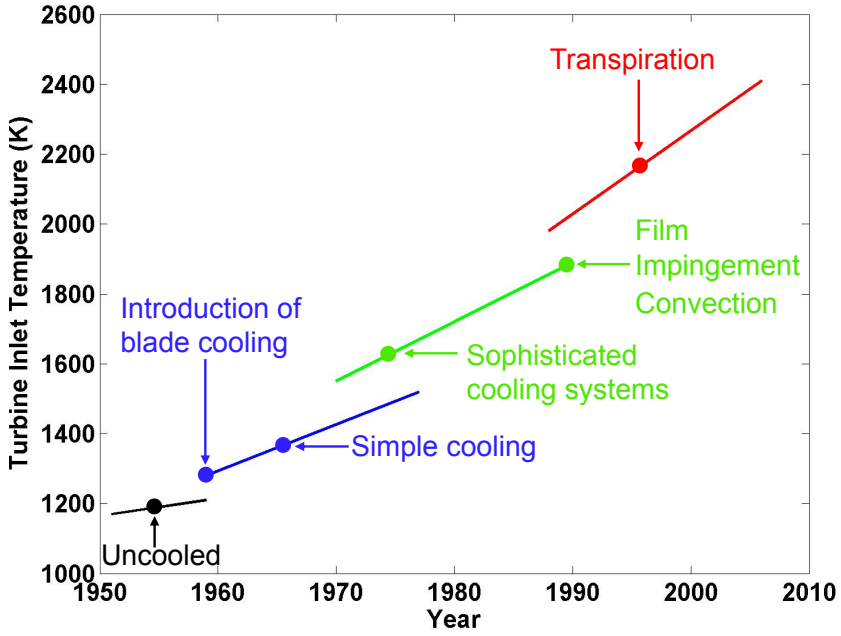

Fig. 1.3 Historical trends of increasing turbine inlet temperatures by Lakshminarayana [40].

1.1.2 Labyrinth Seals

Labyrinth seals are non-contacting seals, widely used to reduce internal leakage of the working fluid. Sturgess and Datta [96] reported that among all technologies to improve the turbine engine performance, half of the improvements benefited from the development

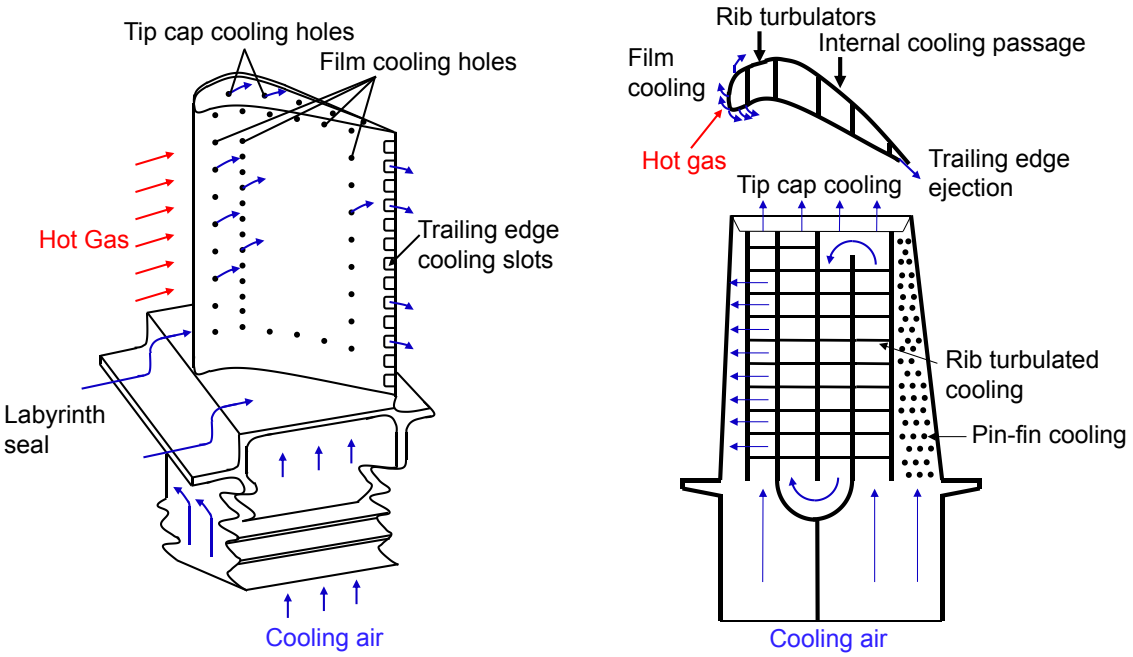

Fig. 1.4 Schematic of turbine internal cooling system.

of sealing technologies. Benvenuti and Tomasini [7] proposed that in large centrifugal compressors the leakage through the final stage labyrinth could result in a loss of 14–16% of the total capacity of the flow. Chan et al. [10] found that a reduction of 4% in leakage could help to reduce *SFC* by 2%. Hence, the performance of these seals plays an important role in improving the performance of the turbomachinery. Because of the increasing pressure ratio and turbine inlet temperature, it becomes increasingly crucial to improve the sealing technology.

Figure 1.5 shows the schematic of the labyrinth seal in this study. The labyrinth seal works by throttling flow through small clearance. During this process a large part of the pressure is converted into kinetic energy and further dissipated in the intervening cavities. The sealing effect of labyrinth seals mainly depends on the configuration of the seal structures. This study focuses on investigation of the optimisation design of labyrinth seals to obtain the best sealing performance. The design uncertainties, combined with the increasing complexity of the labyrinth seal structure (e.g., inclined tooth, honeycomb surfaces), have led to gaps of knowledge in the design process. In the traditional design for a given problem, the variables are selected from limited numbers of discrete values. The obtained solution is just a practical design rather than an optimal design. To improve the optimisation efficiency, a powerful optimisation algorithm is needed which supplies rapid, accurate, and trusted data. The leakage flow generated by the labyrinth seal is complex, including regions of high

acceleration, streamline curvature and recirculations of different scales. This typical flow in the labyrinth seal is so complex, and the range of possibilities for its performance so varied, that an improved and more reliable approach for prediction and optimisation could help to significantly improve the sealing performance.

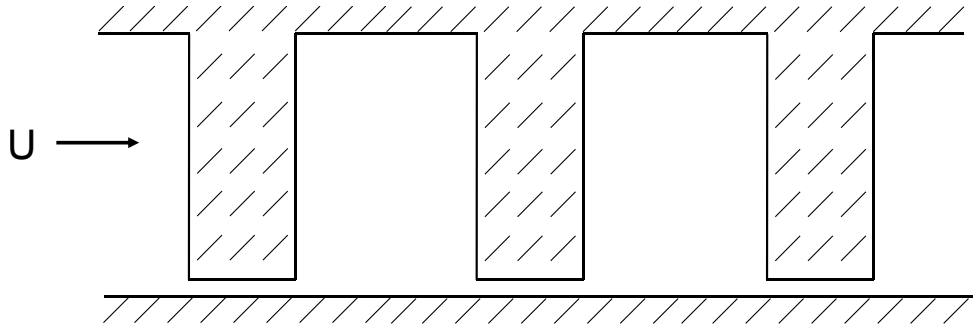

Fig. 1.5 Section of the straight labyrinth seal.

1.2 Numerical Methods

1.2.1 Computational Fluid Dynamics

With the development of computer technology, Computational Fluid Dynamics (*CFD*) has made great progress and has proved itself to be an incredibly valuable tool within both the industrial and academic domains. It is now possible to take all aspects of performance into account, which has helped to reduce the design uncertainty. One of its great benefits is that one piece of hardware can be used to solve a huge array of problems. It can greatly improve the design efficiency and reduce the design costs, especially for large and complex tasks. Combined with numerical calculation and an optimisation algorithm, an automatic optimisation design can be achieved.

1.2.2 Numerical Modelling

CFD is used to simulate the flow field and heat transfer by solving the governing equations. The flows in internal cooling passages and labyrinth seals are highly complex and unsteady. Such complex flow is difficult to be simulated accurately. Baelmans (2002) pointed out that highly accurate modelling approaches are needed to capture the complex flow characteristics, such as unsteadiness and vortex shedding. Such numerical methods include Reynolds Averaged Navier-Stokes (*RANS*) (based on time averaging of the Navier-Stokes equations),

Large Eddy Simulation (*LES*) (based on spatial filtering of the Navier-Stokes equations) models, and so on.

Because of its low computational costs relative to *LES*, *RANS* prediction is widely used for engineering applications. *RANS* modelling is based on time averaging of the Navier-Stokes equations and was first proposed by Reynolds [71]. *RANS* is commonly used for the calculation of stationary turbulence. However, complex turbulent flows, when also combined with unsteady phenomena, are typically not suited to *RANS* [105, 105, 109].

LES has gained importance for its ability to capture most of the important flow features precisely, as indicated by Sewall and Tafti [89]. Leschziner [43] also proposed that *LES* is able to accurately capture the dynamics of turbulence in a free shear problem, such as mixing shear layer, wake separation area and heat transfer, which is difficult to achieve using *RANS*. In *LES*, only large, unsteady, geometry-dependent scales are fully resolved in space and time, while the effects of small scales are modelled. Hence, *LES* is capable of capturing the dynamics of turbulence.

However, its application to complex geometry flows is costly due to its higher grid requirements. Thus, the immersed boundary method (*IBM*) is used in this study. The advantage of *IBM* is that simulations can be performed on almost arbitrary shapes with the same mesh without, or with just minimal, grid reconstruction. It is an ideal approach as hundreds of labyrinth seals will be tested in the optimisation design.

1.3 Objective of Study

This study aims to improve the heat transfer performance in internal cooling passages and sealing performance in labyrinth seals using *LES*. *IBM* will be combined with *LES* for generation of different complex geometries for both the rib cases and labyrinth seals.

According to Han et al. [30], the local flow and heat transfer in the internal cooling passages are a function of several geometric parameters. This study mainly focuses on the effects of different rib shapes (see Figure 1.5) on the heat transfer performance. Here, H_1, H_2, H_3, r_1 and r_2 denote the characteristic parameters of the rib that can be changed to get different geometries. A detailed analysis of the characteristic mechanisms of the heat transfer performance of each case will be evaluated. The results using *LES* will be compared with experiments by Acharya et al. [1] to validate the accuracy of the current numerical model.

This study also concentrates on the better understanding and quantifying of the sealing performance in labyrinth seals, attempting to obtain the best sealing performance through optimisation. As shown in Figure 1.5, labyrinth seals are composed of alternating teeth and cavities. A variety of other geometrical parameters can also have a significant effect on the

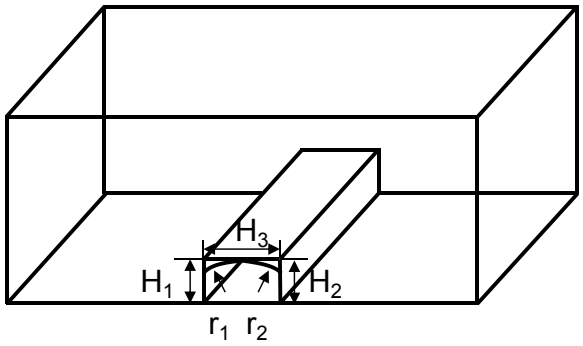

Fig. 1.6 *LES* and *IBM* for arbitrary geometries.

sealing performance. The effects of clearance size (δ), tooth width (L), tooth inclination angle (θ), number of grooves (n), and groove width (l) are considered in this study, as shown in Figure 1.7. These influencing parameters provide reference for the efficient and realistic optimisation design of labyrinth seals. However, these various geometrical parameters interact, making the problem of optimisation a challenging task. Thus, an intelligent optimisation algorithm, the genetic algorithm (*GA*), is chosen for automatic optimisation.

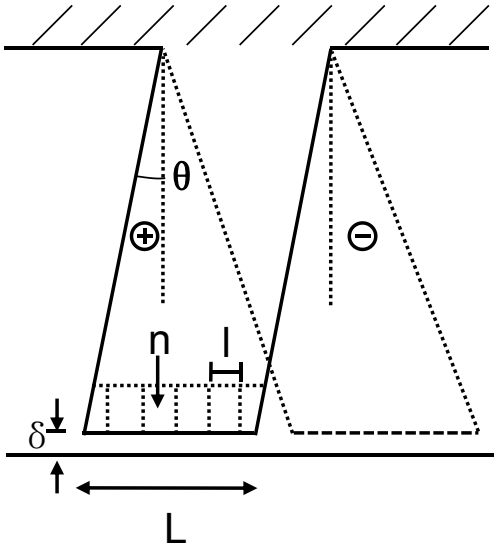

Fig. 1.7 Schematic model for the *GA* parameters.

1.4 Thesis Outline

Chapter 2 reviews the literature that investigate the complex geometry flow in the internal cooling passages and labyrinth seals. Chapter 3 describes the numerical methods, the numerical procedures and *IBM* theory employed in this study. Chapter 4 presents studies of the geometrical impact for internal cooling passages. The validations of *LES* and *IBM* are also included in this chapter. A large scale optimisation study on the labyrinth seals using *GA* is presented in Chapter 5. Chapter 6 continues the study on the labyrinth seals and focuses on the sealing mechanisms. The flow features and loss mechanisms are discussed in detail. Final conclusions and suggestions for future work are contained in Chapter 7.

1.5 Contribution of the author

The basic code for *LES*, *IBM* and *GA* already existed but have been extended by the author in the following ways to be used within this project:

1. The basic existing *IBM* was generalised for more complex geometries. Validation of this improved *IBM* was also performed by the author using the following cases:

Case I – Flow in an Inclined Channel
Case II – Lid-driven Inclined Cavity Flow
Case III – Flow Over a Circular Cylinder

2. Coupling of *LES*, *IBM* and *GA*:

The genetic algorithm code was further developed to link with the main *CFD* code (including the *IBM*). In this way, the advantages of *LES*, *IBM* and *GA* are coupled together, and are combined into an optimisation framework to improve the sealing performance of labyrinth seals and performance of internal cooling passages.

3. Calculation of the turbulent kinetic energy (TKE) budget in the labyrinth seal study:

The code for the TKE budget was also added in the main code and, critically, was used to explore the mechanisms in the turbulent mixing process.

Chapter 2

Literature Review

2.1 Introduction

In this chapter, section 2.2 presents the investigations on the internal cooling passages. Section 2.3 reviews the investigations on the labyrinth seals, and mainly focuses on the effect of different seal geometries on the sealing performance. The gap in a systematic optimisation of the labyrinth seals is also pointed out. The immersed boundary method (*IBM*) to help generate complex geometries is introduced in section 2.4. This is an ideal approach for dealing with the geometries described in this section.

2.2 Internal Cooling Passages

2.2.1 Introduction

The flow field in the internal cooling passages varies based on different rib geometries and arrangements, including pitch ratios, blockage ratios and orientations. Hence, detailed investigations have been carried out to find the relation between these parameters and the heat transfer performance. The ability to investigate these effects using an analytical method is limited, because the large scale eddy structure is highly geometrically dependent, and hence hard to characterise. Therefore, a review of literature is presented for the turbulent flow in internal cooling passages through experimental and numerical studies.

Table 2.1 Experimental investigations on rib geometries

Authors	Geometry	Data measured	Level of data	Core conclusion
Rau et al. [70]	p/e=6, 9, 12	*LDV*	*Nu*, friction factors	data are insufficient
Taslim et al. [99]	45°, 90°	thermocouples	*Nu*, friction factors	45° rib is better
Lockett and Collins [50]	square, rounded	*HI*	*Nu*	*Re* is independent
Hwang [34]	slit, solid		mean velocity, $T.I$, *Nu*, ΔP	slit rib is better than solid one
Liou and Hwang [48]	triangular square semi-circular	*HI*	*Nu*, friction factors	square rib is best
Ahn [3]	square triangular circular semi-circular	*LCT*	*Nu*, friction factors, ΔP	triangular rib is best
Cho et al. [14]	square, semi-circle	thermocouples	*Nu*, friction factors	semi-circle rib is better
Chandra et al. [11]	square triangular circular semi-circular	thermocouples	*Nu*, friction factors, ΔP	sharp corners are useful
Wang and Sundén [118]	square triangular trapezoidal	*LCT*	*Nu*, friction factors	strong sensitivity to geometry

2.2.2 Experimental Investigations

Numerous experiments have been conducted to investigate the effect of different rib configurations. Table 2.1 summarises the major works that investigate different rib geometries. Rau et al. [70] studied three different pitch to height ratios (p/e = 6, 9, 12) in a square cross-sectional duct. The blockage ratio (e/D_h) was 0.1. The schematic of these parameters in the ribbed-channel is shown in Figure 2.1. The local heat transfer distributions were measured between the ribs on the bottom wall. For local heat transfer performance, ribs with p/e = 12 were about 5% higher than ribs with p/e = 9. When considering the overall data, ribs with p/e = 9 provided the maximum heat transfer. Similar experiments have been conducted by Taslim and Wadsworth [100] with different blockage ratios and pitch to height ratios. The blockage ratios were set as 0.133, 0.167 and 0.25, and the pitch to height ratios were 5, 7, 8.5 and 10. The results showed that for heat transfer between the ribs, the average heat transfer coefficient increased with the blockage ratio. Additionally, for ribs with high blockage ratios, there was no significant change (less than 4%) in heat transfer performance with different pitch to height ratios. Taslim et al. (1998) investigated the effect of blockage ratios and rib angles (see Figure 2.2). The blockage ratios were 0.083, 0.125, 0.167, and with two different rib angles of 45° and 90°. For the 90° ribs, their heat transfer performance did not change significantly (around 10%) with the blockage ratio. Amongst all other geometries with blockage ratios of 0.125 and 0.167, the 45° ribs showed the highest heat transfer enhancements.

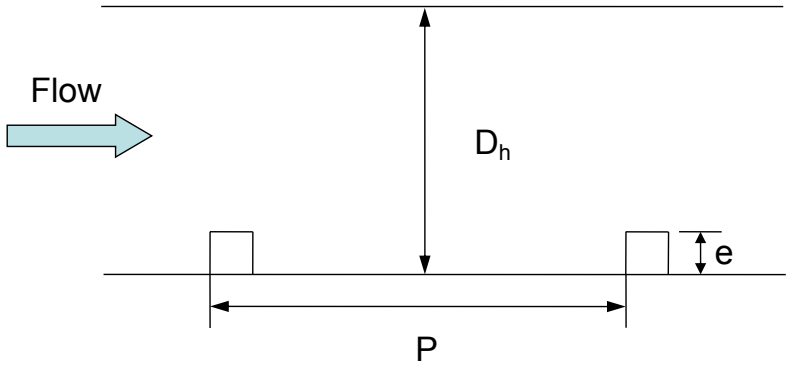

Fig. 2.1 Schematic of parameters in a ribbed channel.

Lockett and Collins [50] applied holographic interferometry (*HI*) to study the effect of rib-roughness on heat transfer in a turbulent flow channel. In their study, the heat transfer distribution of two different ribbed geometries were investigated, namely the square and rounded ribs. The results showed that, for the square rib, the heat transfer distribution was independent of the Reynolds number. Additionally, the maximum heat transfer was found to

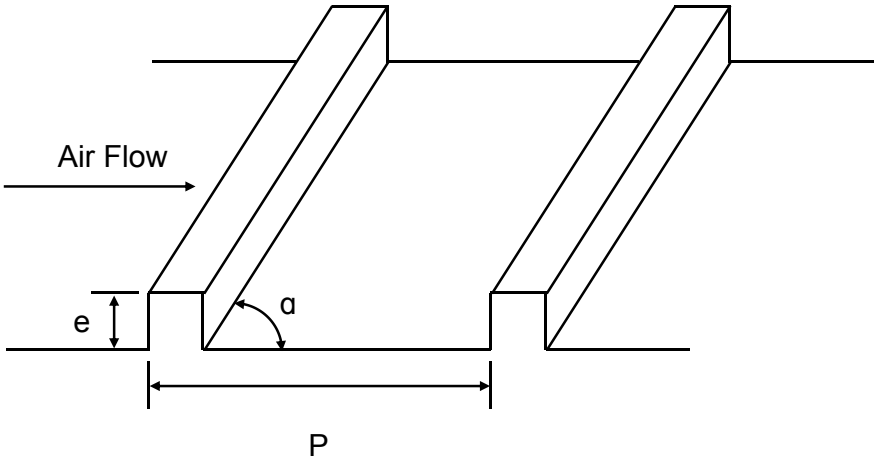

Fig. 2.2 Schematic of angled ribs in a cooling channel.

occur at the leading edge of the top of the rib, and the base of the rear facing rib for both geometries. From the investigations, hot spots in the recirculation region downstream of the rib were found. This is because the unsteady fluid flow was nearly stagnant relative to the mainstream in this area. However, the effect of rib geometries on the heat transfer performance was not conclusive in their study.

Many experiments then have been conducted to assess whether the rib geometry could have an effect on the heat transfer performance. In the experiments of Han et al. [30], the effects of rib shape on thermal characteristics were taken into consideration. Two different shapes (see Figure 2.3) were created by applying modelling clay to the corners of the rectangular ribs. The clay was found to have a much more modest effect on the heat transfer coefficients than on the friction factor. However, Wang and Sundén [118] showed that rib geometry had a significant effect on the flow separation and reattachment, thus consequently on the heat transfer results, especially in the region just downstream the rib. In their study, the heat transfer performance of square ribs, equilateral-triangular ribs, trapezoidal ribs with decreasing height in the flow direction, and trapezoidal ribs with increasing height in the flow direction were investigated. The local and average heat transfer coefficients were measured by liquid crystal thermography (*LCT*). The trapezoidal ribs with decreasing height in the flow direction were found to produce the highest average heat transfer with around 14% higher than the trapezoidal ribs with increasing height in the flow direction, and were likely to be used to suppress the local hot spot which usually occurs in the region just behind the ribs.

Liou and Hwang [48] compared the measured heat transfer and friction coefficients between the square, triangular and semi-circular ribs. The semi-circular rib was found to produce the lowest friction factor due to having a more streamlined shape. All three rib

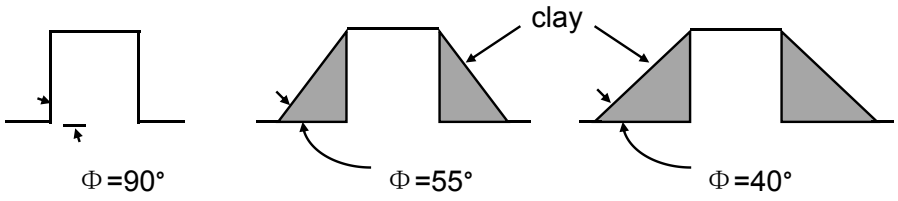

Fig. 2.3 Model of rib shapes by Han et al. [30].

geometries showed comparable thermal performance, with about a 1.6–2.1 fold, a 1.7–2.2 fold and a 1.9–2.7 fold increase in the average heat transfer coefficients compared to the smooth-wall results for the semi-circular, triangular, and square rib walls, respectively. The square rib geometry was found to be the most likely one to yield the hot-spots around the concave corner behind the rib. Chandra et al. [11] evaluated the heat transfer performance of four different rib geometries, namely square, triangular, circular and semi-circular. They also indicated that the square rib provided the highest heat transfer performance. Small differences in the heat transfer performance were found between the triangular, circular and semi-circular ribs.

However, different conclusions were derived by Ahn [3]. Five different rib shapes were studied in a similar experiments conducted by Ahn [3]. These tests involved the following geometries: square, triangular, circular, and semi-circular. The results showed that the triangular rib had the highest heat transfer coefficient. This is because the mixing between the recirculating fluid flow and the fluid flow over the ribs was most active for the sharp triangle-shaped geometries. As a consequence, the radial turbulent fluctuating components which closely relate to heat transfer mechanisms were the highest. The square rib provided the highest friction factor because of the strong turbulent mixing caused by the ribs. Contrary to all the above findings, in the study of Wang and Sundén [118], the square-shaped ribs were found to have nearly the same heat transfer and friction characteristics as the triangular-shaped ribs.

Chung et al. [15] examined the flow and heat transfer characteristics in a rectangular channel with different rib shapes, namely square and semi-circular. The local heat transfer along the wall was measured between these two ribs. They found that the Nusselt number ratio of the semi-circular ribs was about 8% higher than that of the square ribs. This is consistent with Cho et al. [14]. However, in the study of Liou and Hwang [48], the square rib resulted in almost 20% higher average heat transfer rate than the semi-circular rib. Taslim and Korotky [98] also showed that rounded-corners deteriorated the heat transfer performance.

From all these experimental results, we can say that there is still no certain relation between different rib shapes and heat transfer characteristics. This may be because the limited

information obtained from experiments cannot help with achieving general conclusions for this very complex flow field, as provided in Table 2.1. Rau et al. [70] thus pointed out the importance of further developments in numerical analysis that are not limited to global performance estimations but capture local effects and complex unsteady interactions. Thus investigations should be further pursued by numerical methods with high fidelity turbulence modelling. However, first, lower fidelity turbulence models are reviewed.

2.2.3 Numerical Investigations

RANS Methods

Computational cost has limited most applications of *CFD* to using the Reynolds averaged Navier-Stokes (*RANS*) models (based on time averaging of the Navier-Stokes equations). However, *RANS* models are not reliable for all flow regimes, and can lead to poor flow and heat transfer predictions in complex geometries with separated flow [105, 106, 109]. In the present study, the flow in a ribbed duct has complex flow features: boundary layer separation, primary and secondary recirculation, reattachment of boundary layer, etc. *RANS* is not suitable for modelling this kind of flow because it is poor at predicting separated flows with large scale coherent structures. The accuracy of *RANS* and other *CFD* methods are compared in Table 2.2.

Previous studies have shown that the turbulent viscosity and the turbulent shear stress are usually over predicted by *RANS* in such flows [22, 4]. Eddy viscosity models which assume isotropy of turbulence [67], fail to capture key flow features accurately. In order to understand the physics of turbulence, Driver and Seegmiller [22] conducted a detailed experiment and compared the results with the standard k-ε model (this model solves two transport equations for turbulent kinetic energy (k) and dissipation (ε)). The mean and turbulent fluctuations in the flowfield were measured using a laser Doppler velocimeter (*LDV*). The standard k-ε model failed to locate the peak of turbulent Reynolds stresses. In some cases, the differences in heat transfer between *RANS* models can vary by approximately 100% [109].

Table 2.2 Comparison of *CFD* models

Authors	Method	Advantages (A) / Disadvantages (D)
Liou et al. [47]	k-ε model	(D) cannot predict Reynolds stresses accurately
Acharya et al. [1]	k-ε model	(D) underpredicted local Nusselt numbers by more than 20% (D) underpredicted Reynolds stresses by around 18%
Rigby [81]	$k-\omega$ model	(D) cannot predict reattachment at $Re < 5000$
Saidi and Sundén [84]	k-ε model	(D) overpredicted velocity fields up to 100% (D) cannot predict heat transfer accurately with around 15% discrepancy
Iacovides and Raisee [35]	*EVM*	(D) cannot predict heat transfer accurately with around 20% discrepancy
Ooi et al. [57]	v^2-f, k-ε, $S-A$ models	(D) failed to predict heat transfer (up to 100% discrepancy)
Tafti [97]	quasi *DNS*, *LES*	(A) predicted heat transfer to within 10–15%
Ahn et al. [2]	*LES*	(A) predicted flow characteristics within 5% discrepancy (A) predicted heat transfer within 15% discrepancy
Sewall et al. [90]	*LES*	(A) predicted the turbulent mechanism within 10–15% discrepancy
Liu et al. [49]	*ZLES*, *DES*	(A) captured complex unsteady flow features within 8% discrepancy
Viswanathan and Tafti [117]	*LES* *DES* *RANS*	(A) captured shear layer transition better than *DES* (A) predicted heat transfer more accurately than *RANS*
Tyacke and Tucker [113]	*LES*	(A) predicted heat transfer with 2.2% discrepancy

Liou et al. [47] and Acharya et al. [1] pointed out that the inability of common *RANS* models to correctly predict the Reynolds stresses in regions of high anisotropy is one of the main reasons for their failure. Acharya et al. [1] used the standard k-ε model and non-linear k-ε model to investigate the flow and heat transfer predictions in a fully developed ribbed duct. Comparisons were made with the experimental data, and revealed that the local Nusselt numbers were underpredicted by both models by more than 20%. Both models also poorly underpredicted the reattachment length ($\approx$ 18% error), where the Reynolds stresses were grossly underpredicted. They believed that this is because both models do not directly account for the large-scale effects in this region.

Rigby [81] employed *RANS* models to study heat and mass transfer in a ribbed channel. It was observed that the *RANS* models did not predict the reattachment between ribs at low Reynolds numbers (< 5,000). Iacovides and Raisee [35] used *RANS* models to simulate the flow and heat transfer in a periodic ribbed duct. The results showed that, even though the effective viscosity model (*EVM*, solves the turbulence stresses by augmenting the molecular viscosity with an eddy viscosity) could account for anisotropic turbulence, it could not predict heat transfer accurately (with around 20% discrepancy). Saidi and Sundén [84] used k-ε models in a periodic ribbed channel. The results of local and mean thermal characteristics were predicted using two low *Re*, k-ε turbulence models. The models used in this study could not provide accurate predictions of the velocity and thermal fields. The discrepancy for the fluctuation components is up to 100%.

Ooi et al. [57] used the v^2-f (this model solves the eddy viscosity and anisotropic wall effects), k-ε and Spalart-Allmaras *RANS* models to calculate the turbulent flow field and heat transfer in three-dimensional ribbed ducts. However, the heat transfer predictions do not compare well with the experiments (up to 100% discrepancy). This is because the eddy viscosity cannot adequately model the presence of strong secondary flow structures along with the separated flow around the ribs. Similar findings were reported by Phibel et al. [65] who investigated ribbed channels with high blockage ratios and pointed out that the isotropy assumption was not valid in ribbed channels because of the unsteady nature of the large separated flow generated by the ribs. Fransen et al. [26] used different *RANS* models (k-l, k-ε and v^2-f) in the ribbed channel. They also found that the *RANS* models were not able to correctly predict the flow because of the massive separations and recirculations present. In contrast, Fransen et al. [26] found that Large Eddy Simulation (*LES*) (based on spatial filtering of the Navier- Stokes equations) reproduced all the features of the flow inside the channel well.

Therefore, more reliable turbulence model is required for unsteady flows with high streamline curvature. Recently, *LES* has been widely used. This is due to its advantage of

accurately capturing most of the important flow features. The following section presents a literature reviews where *LES* has been carried out to investigate the characteristics of flow and heat transfer in ribbed channel configurations.

LES Methods

One of the first studies using *LES* for a ribbed channel geometry was performed by Murata and Mochizuki [54]. The heat transfer in a bi-periodic ribbed channel was investigated. Locations of the high heat transfer regions predicted by *LES* were found in front of the rib and were in good agreement with the measurements (within 10% discrepancy). Tafti [97] investigated a periodic rib-roughened duct using quasi *DNS* (quasi-Direct Numerical Simulation) (resolving the energy containing eddies but with no *SGS* model) and *LES*. The results showed that *LES* predicted the heat transfer and friction coefficient within 5–10% of the experimental data, whereas quasi-*DNS* underpredicted these quantities by around 20%.

Liu et al. [49] conducted numerical simulations for a ribbed channel flow using a *k-l* based zonal large Eddy simulation (*ZLES*) (only non-equilibrium regions are solved using *LES*) method and the *S-A* based Detached Eddy Simulation (*DES*) (*LES* with an extensive near wall *RANS* region) [93] approach. Comparisions were made with *RANS* and measurements, and showed that *ZLES* and *DES* were able to capture complex unsteady flow features more accurately than *RANS*, and had good agreement with the measurements (within 8% discrepancy). Similar conclusions were made for heat transfer predictions. *DES* was also found to improve predictions over *RANS* by Viswanathan and Tafti [117]. Comparisons of *LES* and *DES* were made in the same ribbed duct by Tafti [97]. Although *DES* was more accurate than *RANS*, it did not capture shear layer transition accurately, predicting a development length around two rib pitches greater than the *LES*.

Sewall et al. [90] predicted turbulent flow and heat transfer in a ribbed duct with180° bend using *LES*. The configuration is shown in Figure 2.4. The flow features in terms of transition, mean velocities, Reynolds stresses and heat transfer were calculated and compared with the measurements. The results showed that *LES* was able to predict the turbulent mechanism correctly in both qualitative and quantitative manners with a deviation of 10–15% from the experiments. *LES* and *RANS* methods were then applied by Tyacke and Tucker [113] to investigate the turbine blade ribbed internal duct with a 180° bend containing 24 pairs of ribs. Flow and heat transfer predictions from *LES* were compared with experimental data and found to be in excellent agreement, with 2.2% deviation even with a relatively modest grid ($982 \times 92 \times 117$). The linear *RANS* models were shown to perform poorly for heat transfer. Therefore, Tyacke and Tucker [113] concluded that *LES* is a relatively cheap method for obtaining accurate heat transfer predictions for these types of flows.

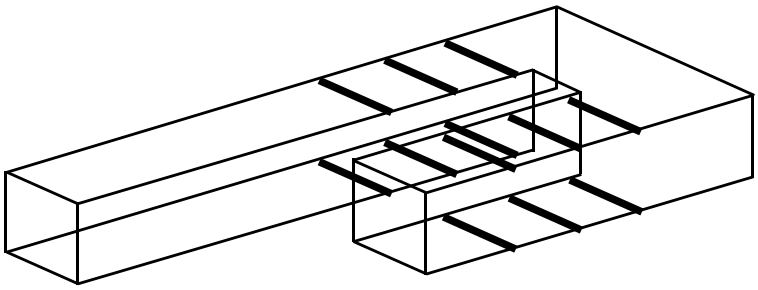

Fig. 2.4 The calculations of a 180° bend region used by Sewall et al. [90].

From the above review it can be seen that *LES* is more accurate than *RANS*, especially for this type of flow that is governed by large scales of turbulence. Hence, in this study, *LES* is used to investigate the complex flow in internal ribbed passages. Table 2.3 summarises some of the investigations just described using *LES*. Comparison with the experimental results in Table 2.1 shows that with *LES* much more detailed data can be obtained.

Table 2.3 Iinvestigations on rib geometries using *LES*

Authors	Level of data	Accuracy
Tafti [97]	*Nu*, friction factors, turbulent energy	*LES* within 5–10% discrepancy
Sewall et al. [90]	*Nu*, turbulent quantities transition, secondary flows	*LES* within 10–15% discrepancy
Liu et al. [49]	*Nu*, unsteady flow feature	*LES* within 8% discrepancy
Tyacke and Tucker [113]	*Nu*, Reynold stress whole velocity fields	*LES* within 2.2% discrepancy

2.3 Labyrinth Seals

High speed turbomachinery produces power in a high temperature and pressure environment. Because of the increasing pressure ratio and turbine inlet temperature, it becomes increasingly crucial to improve sealing technology. Labyrinth seals are the most typical sealing technologies. They are used to control the internal leakage of the working fluid by throttling flow through small clearances.

2.3.1 Analytical Investigations

The analytical prediction of leakage flow in labyrinth seals can be traced back to Vermes [116]. The effect of different tooth configurations on the flow rate through labyrinth seals was studied analytically by Fasheh [24]. In this work comparisons were made between labyrinth seals with rectangular and tapered tooth profiles (Figure 2.5). The results showed that seals with tapered teeth had lower leakage values than flat-tipped seals. Scharrer [86] investigated the flow in a labyrinth seal through experimental and theoretical methods. Jet flow theory was used for the calculation of the recirculation velocity in the cavity. This is a theory for the flow of a two-dimensional, turbulent, and isoenergetic jet. The flow pattern in a labyrinth seal cavity by Scharrer [86] is shown in Figure 2.6. Teeth-on-rotor and teeth-on-stator labyrinth seals with different radial clearances were investigated. In this report, the theoretical results for leakage were lower than the test results by 25%. The leakage was found to increase as clearance increased for both seal types.

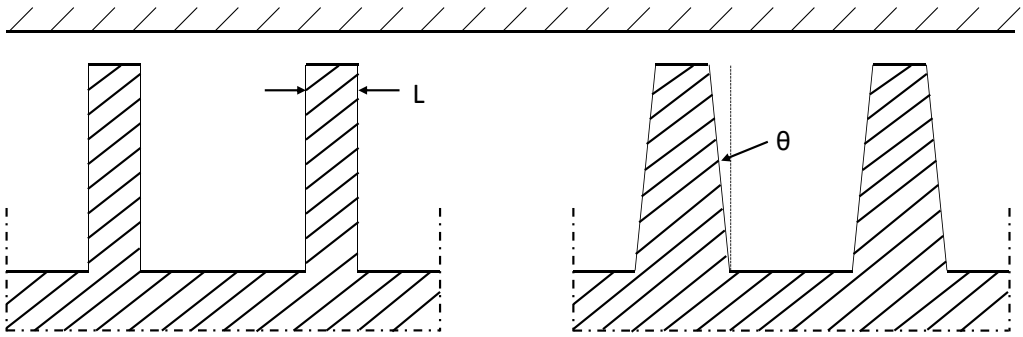

Fig. 2.5 Labyrinth seals with square and tapered blades by Fasheh [24].

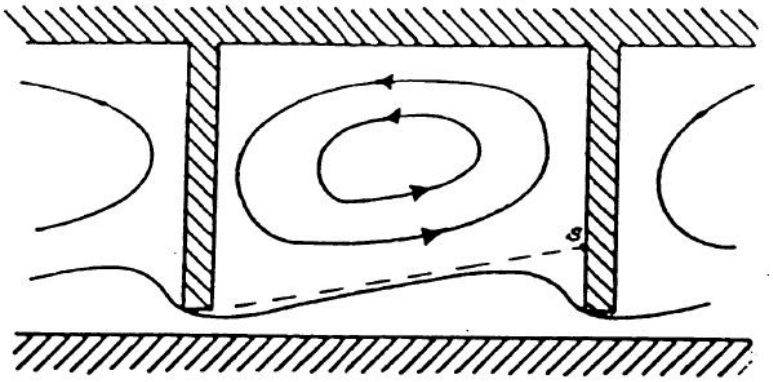

Fig. 2.6 Flow pattern in a labyrinth seal cavity by Scharrer [86].

Despite these efforts, it was proved that analytical models to predict satisfactory seal performance remain difficult to set up. Thus, conducting experiments to study the leakage characteristics under real engine conditions is the recent research trend [58].

2.3.2 Experimental Investigations

Wittig et al. [124] initially conducted experiments to investigate the influencing factors on the leakage features of labyrinth seals. The results showed that, under static conditions, the amount of leakage was mainly affected by the tooth geometries and pressure ratio. Waschka et al. [119] investigated the effect of rotational speed on labyrinth seal leakage. They found that the effect of rotational speed can be negligible (less than 2%) at Reynolds numbers between 5,000 to 10,000. For most labyrinth seals, they are under the condition of Reynolds number less than 10,000. Thus, it is reasonable to claim that, under realistic operating conditions, leakage is only slightly affected by the rotational speed. Yu and Childs [127] conducted experiments to investigate the mass flow coefficients in labyrinth seals with a grooved honeycomb stator. Similar conclusions to Waschka et al. [119] were also given by Yu and Childs [127]. Yu and Childs [127] found that, given a substantial increase in the rotational speed, the mass flow coefficients decreased only slightly by around 4%.

2.3.3 Numerical Investigations

The experimental approach still has its limitations. When Zimmermann [131] studied secondary air systems, only the global aerodynamics were studied. This was partially due to restricted access to instrumentation. With the development of *CFD*, the knowledge of component performance has been extended. *CFD* is then mainly used as the numerical method to predict the leakage performance and reveal flow characteristics. *RANS* has long been used, however, *RANS* models tend to fail in regions of large-scale unsteadiness and high streamline curvature. Note, streamline curvature effectively gives centrifugal body forces, which modify the turbulence that is not represented by most *RANS* turbulence models. Examples are flows around bluff bodies [112] and many flows found in turbomachinery [105, 106]. The sealing flows studied here involve vortex shedding, streamline curvature, and regions of high acceleration, which present significant challenges to *RANS* models. A more accurate and reliable approach for modelling complex flows in arbitrary geometries is hence needed. For this type of unsteady flow with high streamline curvature, Large Eddy Simulation (*LES*) is more reliable, as demonstrated by Tyacke et al. [111]. In the work of Tyacke et al. [111], *LES* and hybrid $RANS-LES$ were chosen to use in straight-through and stepped labyrinth seals. Comparisons were made between different *RANS* models and

LES model. The results showed that *LES* predicted the flow in a labyrinth seal with greater consistency than *RANS*.

Certain situations were not considered in the 2-D tests conducted by Zimmermann [131], like rotational effects. Thus, Zimmermann [131] suggested that correlations should be sought that cover the effects of geometry, entry conditions, pressure ratio, and distorted geometries like start up and worn conditions. Next, a literature review on investigations into the effects of different seal geometries is given.

2.3.4 Effect of Labyrinth Seal Geometry

Labyrinth seals are designed with a variety of different geometries. The wide variety of geometries and flows generated by labyrinth seals extend to other components and applications [25]. Much recent work has been focused on investigating the effects of complex seal configurations on leakage performance [62–64]. The results show that a significant increases in turbine efficiency can be obtained by careful modification of the sealing zones.

Clearance Size

An early experimental study on the effects of seal geometry on the mass flow rate was conducted by Zabriskie and Sternlicht [129] in straight-through labyrinth seals. The results showed that the ratio of tooth thickness to clearance has a significant effect on the coefficient of discharge. For a constant pressure ratio the leakage coefficient varied as much as 20%. Later, Stocker [94] started to investigate new labyrinth seal configurations using water flow visualization in the first phase of their labyrinth seal geometry investigation. For a given seal concept, the best performance was achieved by decreasing the seal clearance, increasing the tooth pitch and varying the step height. Wittig et al. [124] investigated the effects of seal geometry on leakage rates using straight-through labyrinth seals. They found that the effects were most evident for small clearances. Childs and Vance [13] conducted experiments to review the theories of labyrinth seal mechanisms and also indicated that clearance can significantly affect the leakage rates. The results showed that decreasing the clearance by 50% would result in a 20% leakage reduction.

Tooth Configuration

Variations in the geometries of teeth are common. In an experimental investigation with non-rotating labyrinth seals, Gamal and Vance [27] studied a variety of seal configurations focusing on the effects of tooth profile and tooth thickness (L) (see Figure 2.5) on leakage. By doubling L a leakage reduction of up to 20% was achieved, possibly due to an increase

in frictional losses. However, when decreasing the cavity depth, no impact on leakage was found. Gamal and Vance [27] also noted that different trends could be found for different numbers of teeth, due to complex interactions. However, different conclusions were drawn by Rhode and Hibbs [73]. They found that for straight-through seals leakage was almost independent (less than 2%) of tooth thickness. Thus, the effect of tooth thickness on leakage cannot be clarified yet.

Rhode and Guidry [72] analysed labyrinth seal performance using the standard k-ε model. They found that with perfectly sharp corners, mass flow can be reduced by up to 30%. In order to understand the leakage reduction and total pressure loss mechanisms, Vakili et al. [114] investigated various tooth configurations in a straight through labyrinth seal both experimentally and numerically. The leakage rates and total pressure loss were calculated using the k-ε model. They mainly focused on factors such as turbulence induced losses, and cavity flow topology. The best configuration was obtained with inclined teeth (θ) (see Figure 2.5). The results showed that stagnation, flow curvature and turbulent throttling were increased, causing maximising energy losses through the seal.

Groove Geometry

Rhode et al. [74] used a 2D planar flow visualization facility to investigate the feature of "annular grooves" in labyrinth seals. Annular grooves resulted in higher leakage resistances, 26% higher than the baseline seal. Rhode and Allen [78] studied grooves (see Figure 2.7) in straight-through labyrinth seals. They found that the leakage resistance was only slightly (around 5%) affected by rounded concave corners compared to sharp concave corners. However, the leakage resistance decreased sharply (more than 80%) with increasing groove depth. Rhode and Allen [79] continued to compare the groove sizes with the same clearances and groove combinations for stepped labyrinth seals as Rhode and Allen [78] used for straight-through labyrinth seals. In this case, the leakage resistance decreased as step height increased. To understand the geometry-leakage relationship, Michaud et al. [52] conducted experiments using a 2D stepped labyrinth seal. The mass flow can be reduced by up to around 20% with moderately modified geometry.

Rhode and Adams [76] numerically investigated the effect of tooth location in straight-through labyrinth seals using the k-ε turbulence model. The investigated grooves were rectangular and with similar sizes to Zimmerman et al. [130] and Stocker et al. [95]. The tooth location was varied upstream and downstream of the groove centreline. The centred tooth axial position was found to provide the highest leakage rate. The most sensitive groove to tooth axial location was the deep-wide groove, with the shallow-narrow groove being the least sensitive. Later, with the same technique, Rhode and Adams [77] investigated

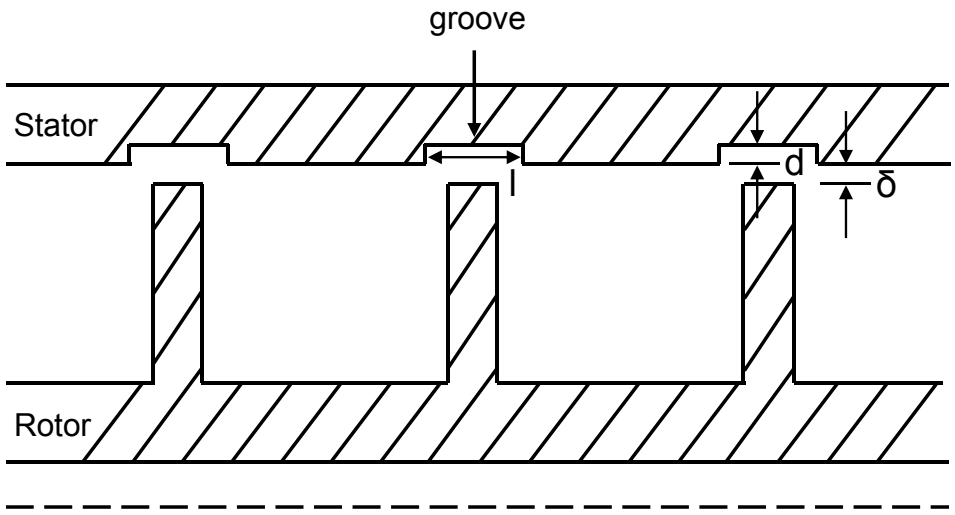

Fig. 2.7 Schematic of the straight-through seal grooves used by Rhode and Allen [78].

the effects of clearance size (δ), groove width (l) and groove depth (d) on leakage rates in straight-through labyrinth seals. These paremeters are presented in Figure 2.7. The results showed that the groove width and clearance size were the dominant variables with respect to the cavity flow pattern. The effect of groove depth reduced as the groove width narrowed.

Honeycomb Seals

Several investigators have reported the high performance of labyrinth honeycomb seals. The honeycomb seal, was originally introduced in the 1960s [92]. Comprehensive investigations on the leakage performance of labyrinth seals with honeycomb lands have been conducted by Stocker et al. [95] through experiments. The results showed that with the use of honeycomb lands, the leakage flow rate was decreased by up to 24% when compared with the smooth land. Similar findings were reported by Childs et al. [12] who observed that the leakage of honeycomb seals was about a third less relative to a standard labyrinth seal. The honeycomb structure in the study of Childs et al. [12] is shown in Figure 2.8. However, different conclusions were given by Schramm et al. [88] and Yan et al. [125]. Schramm et al. [88] investigated the leakage and velocity field through stepped labyrinth seals (see Figure 2.9) with honeycomb using a standard k-ε model. They claimed that the presense of honeycomb enlarged the effective clearance width and resulted in an increased mass flow rate of around 30%. The same kind of findings were reported by Yan et al. [125] who also used the standard k-ε model to calculate the leakage rate in the honeycomb labyrinth seals. In the study of Yan et al. [125], the leakage flow rate of the honeycomb configuration was higher than the smooth

configuration by more than 10%. They also explained that this is because the honeycomb facing caused the effective clearance to increase.

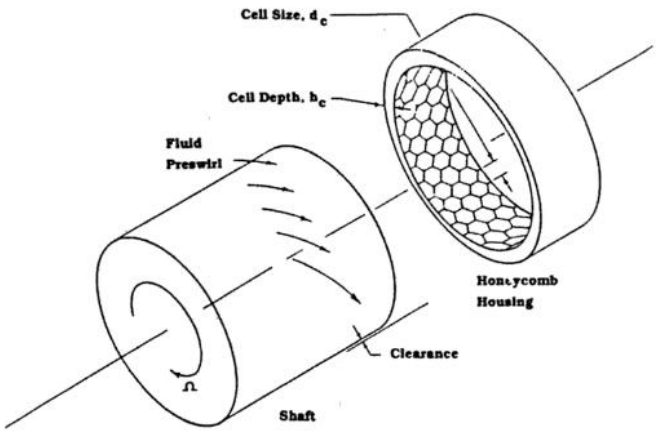

Fig. 2.8 Honeycomb structure in the study of Childs et al. [12].

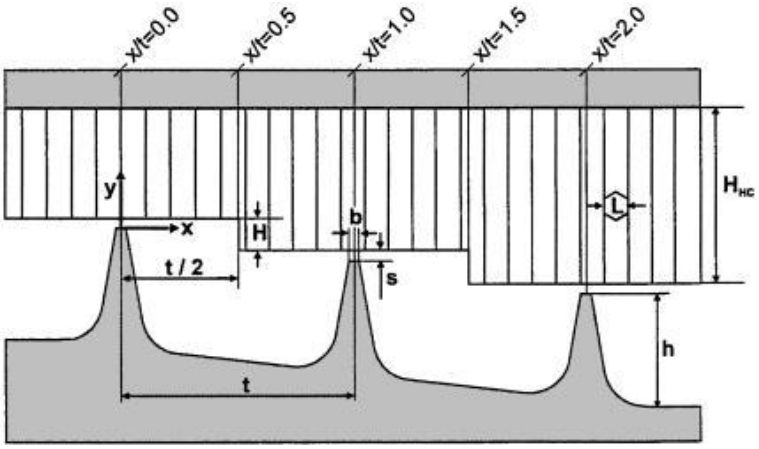

Fig. 2.9 Geometry of stepped labyrinth seal by Schramm et al. [88].

2.3.5 Design Optimisation

Rhode et al. [75] attempted to optimise the labyrinth seal through experiments. The seal width, step width, step height, and clearance size were chosen as the variables. An optimal seal was then obtained. With an increased number of cavities the turbulence dissipation in this optimal seal was increased, and reduced the leakage performance by 60% compared to the baseline design.

Current computing capacity allows the use of *CFD* to optimise designs automatically, by calculating the performance of a variety of different geometries within a tolerable computing

time. Schramm et al. [87] optimised labyrinth seals to minimise the leakage in stepped labyrinth seals using a simulated annealing (*SA*) optimisation algorithm, developed from the process of annealing in metal work, as detailed in Chapter 3. Two variables were taken into consideration in the optimisation process: the step position and the height of the step. The best leakage performance was achieved when combining a large step height and a large step distance to the upstream knife, as shown in Figure 2.10. An artificial neural network (*ANN*) (a computational approach based on a collection of neural units loosely modelling the way a biological brain solves problems) was used by Asok et al. [5] to identify the optimal configuration of a square cavity seal. The pressure drop was analysed using the standard k-ε model. The results showed that the geometrical configuration of the grooves played a major role in defining the pressure drop. Figure 2.11 shows the schematic of the optimal seal. The pressure drop ratio of the optimal seal increased by more than 75% over the optimal square cavity seal. The reason for the improvement was identified to be a counter rotating, double vortex structure within the cavity, which promoted higher turbulent dissipation of leakage flow momentum.

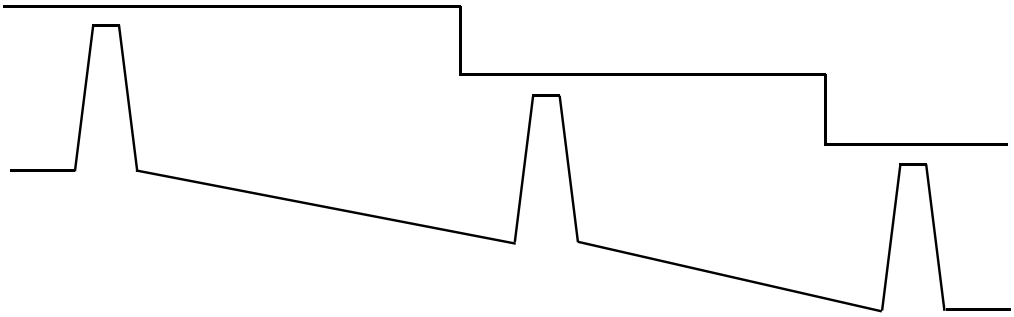

Fig. 2.10 Best configuration in the study of Schramm et al. [87].

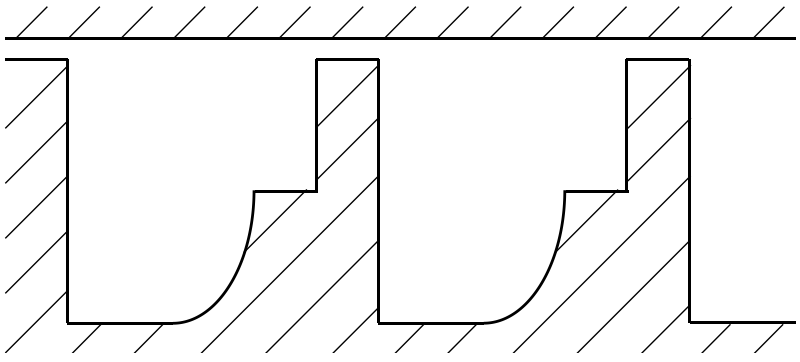

Fig. 2.11 The curved cavity labyrinth seal used by Asok et al. [5].

Few publications on optimisation design of labyrinth seals can be found, and a systematic optimisation based on various geometrical parameters has not been reported so far. However,

design optimisation has been successfully applied to other areas of turbomachinery. A detailed study of optimisation methods for a variety of applications was given in Jin et al. [36]. Obayashi and Takanashi [56] employed a genetic algorithm to help design turbine blades more efficiently enabling a gradual convergence towards the best possible solution through a process of evolution. The use of genetic algorithms is becoming increasingly common. For example, Pierret [66] explored the ability of genetic algorithms to optimise a compressor blade design, which was found to perform well. Watson and Tucker [121] optimise the performance of film-cooling slots for cutback trailing edges using a genetic algorithm. Six hundred *LES* simulations were conducted. The optimised design showed a considerable improvement over the previous experimental geometries. Significant benefits of using a genetic algorithm are that a wide design space can be explored, reducing the possibility of designs becoming trapped in local minima and providing a large data set for lower order modelling.

RANS has been extended to undertake design optimisations by Lee et al. [41]. However, Watson [120] showed that *RANS* can provide opposite trends to those found physically. Thus, *LES* is used to more deeply understand the flow patterns generated by complex seal configurations.

2.4 Immersed Boundary Methods

As discussed earlier, *LES* is able to reveal the flow physics. Even though *LES* is typically computationally expensive compared to *RANS* by a factor of at least 100 [110], it provides greater physical insights. However, when it is used with complex geometries and curved shapes, a complicated grid system needs to be built to fit the computational mesh exactly to the body as shown in Figure 2.12(a). On the other hand unstructured solvers have a substantial computational overhead having the need to solve connectivity information.

An approach called the immersed boundary method (*IBM*) has been developed to use with *LES* in complex rigid geometries. *IBM* was first put forward by Peskin [61] to simulate blood flow in heart valves. Yun et al. [128] simulated the flow around a cylinder using *IBM* with Re = 3,700 and 10,000. Results such as lift coefficients and drag coefficients were in line with the theoretical results, which validated the accuracy and feasibility of *IBM*. Further development of the method was presented by Tseng and Ferziger [104]. The accuracy of *IBM* has been validated by Tseng and Ferziger [104] using the flow past a circular cylinder and *LES* of turbulent flow over a wavy surface. A similar investigation to that of Tseng and Ferziger [104] was conducted by Preece [68]. Preece [68] combined the use of *IBM* with *LES* for higher Reynolds number flows. The flow around a circular cylinder was used to

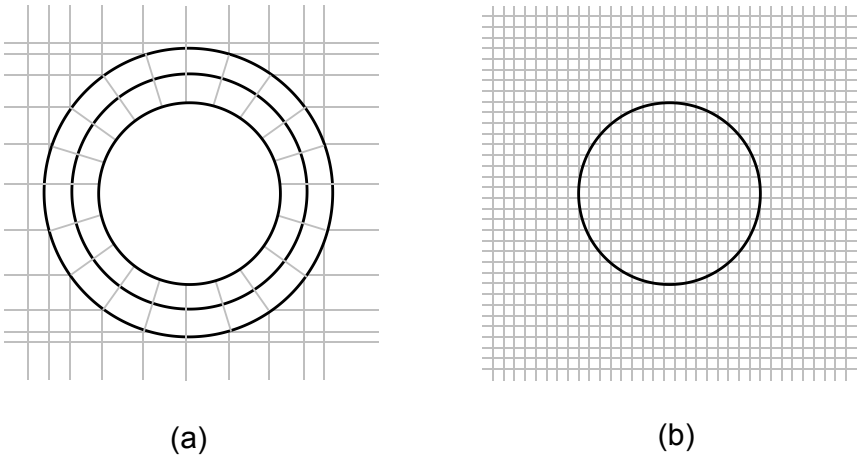

Fig. 2.12 Comparision of mesh with or without *IBM*.

validate the *IBM* and the results were comparable in accuracy to the work of Tseng and Ferziger [104], Kim et al. [38], and Lai and Peskin [39]. A new Cartesian cut cell method was employed on the solid boundaries by Tucker and Pan [107], who also applied surface cell interpolation using a novel hybrid technique. Three cases were investigated to test the accuracy of this approach: flow in a plane channel skewed to the computational grid lines, wall-driven flow in an inclined box, and flow past a cylinder. The results were in agreement between the analytical method and experimental data.

Thus, *IBM* will be used to eliminate the effort for complex grid generation and the overhead of unstructured grids - this being especially significant for *LES*. Figure 2.12(*b*) shows a simple Cartesian structured grid which can be used to create a surface non-coincident with the grid mesh. The advantage of this method is that with the same mesh, simulations can be performed on almost arbitrary shapes without, or with just minimal, grid restructuring. This allows for a resonable computational cost, as multiple geometries of ribs and labyrinth seals will be tested further in this study.

2.5 Conclusions

At present, with the improvement of the engine power, turbine inlet temperature is increasing rapidly, and materials cannot bear such a high temperature without additional cooling. Hence, advanced designs for turbine cooling structures are necessary. Sections 2.2 and 2.3 show that *RANS* models are poor at predicting flow and heat transfer in complex geometries with separated flow. Thus *LES* is used to investigate the large scale unsteady flow in internal cooling passages, and flows with high streamline curvature in labyrinth seals. The literature

in section 2.1 shows that conclusions about the effects of some rib shapes are not consistent, such as the triangular rib, semi-circular rib and slit rib. Even though the sharp corners of the triangular ribs are not easy to manufacture or cannot be maintained throughout the blades lifetime, it is necessary to investigate whether a triangular rib, for example, is able to provide better thermal performance, and if so why this is. *IBM* will be used to eliminate the effort for complex grid generation, both for the ribbed passages and the labyrinth seals.

Section 2.3 shows that although the effects of labyrinth seal geometry (clearance size, tooth thickness, tooth configuration and groove shape) have been examined by many investigators, an optimised design based on various labyrinth parameters has not been reported so far. The objective of this study is to investigate the effects of geometry on leakage performance, and to find the optimal seal geometry with the best sealing performance.

Chapter 3

Turbulence Modelling and Numerical Methods

3.1 Turbulence Modelling

The overwhelming majority of fluid motion in nature is turbulent. Most industrial fields involve turbulent problems, especially in the field of aerospace. Tennekes and Lumley [102] identified irregularity, diffusivity, vorticity fluctuations, dissipation and large Reynolds numbers as the key features of turbulence. Turbulence is a complex nonlinear multi-scale phenomenon. There is a wide range between the maximum and minimum scales at high Reynolds numbers. Taylor [101] first put forward a statistical method to describe the structure of motions, to reveal the various eddies that comprise turbulent flow. Turbulence energy is transfered from large eddies to small eddies, and then finally being dissipated to heat. This kinetic energy dissipation is mainly determined by the small eddies, which tend to be universal and isotropic.

Because of its complexity, turbulence is difficult to describe. Traditionally design tasks were improved by experiments, but this is increasingly being replaced by Computational Fluid Dynamics (CFD). With the rapid development of computer technology, CFD has made great progress and has been widely used in studying turbulent flow. As shown in Chapter 2, LES is chosen in this study to investigate the complex flow in internal cooling passages and labyrinth seals. The details will be presented in the following.

3.2 Large Eddy Simulation

In *LES*, turbulence scales can usually be divided into resolved and unresloved scales. The basic idea is described by Bradshaw [9] and Rogallo and Moin [82]: the resolved scale of the field represents the large eddies, which is greatly influenced by boundary conditions; while the contribution of the unresovled small scales is simulated by the sub-grid scale (*SGS*) model. By modelling the smallest scales, the computational cost for *LES* is much smaller than for *DNS*. According to A.N. Kolmogorov's similarity hypothesis, the small scales tend to be more isotropic and less affected by boundary conditions, thus simple sub-grid scale (*SGS*) models for small scales can perform well.

3.2.1 Governing Equations

LES uses a spatial filtering operation to separate the large and small eddies. The method starts with a filtering function (and a certain filter width) in order to resolve scales greater than the filter width. The grid resolution itself acts as a filter and is often used alone. Explicit filters come in many forms [108] and if used, move normally seperate the large and small scales. In this case the grid acts as a secondary filter. In all cases an *SGS* model is used to model the overall dissipative effect of the small scales. The *SGS* model also aims to sensibly model the interaction between the resolved and unresolved scales.

For the internal cooling passages considered, the ratio of Grashof number to the Reynolds number is small ($Gr/Re^2 < 0.01$). Therefore, buoyancy effects are negligible and cooling is dominated by forced convection. The flow can therefore be assumed incompressible (and constant density) without serious error. For incompressible flows, the governing equations for *LES* can be written in the following common forms:

$$\frac{\partial \overline{u}_j}{\partial x_j} = 0 \tag{3.1}$$

$$\rho \frac{\partial \overline{u}_i}{\partial t} + \rho \frac{\partial \overline{u}_i \overline{u}_j}{\partial x_j} = -\frac{\partial \overline{p}}{\partial x_i} + \frac{\partial}{\partial x_j}[\mu \frac{\partial \overline{u}_i}{\partial x_j}] - \frac{\partial \tau_{ij}}{\partial x_j} \tag{3.2}$$

$$\rho \frac{\partial \overline{T}}{\partial t} + \rho \frac{\partial \overline{u}_j \overline{T}}{\partial x_j} = \frac{\partial}{\partial x_j}[\frac{\mu}{Pr} \frac{\partial \overline{T}}{\partial x_j}] - \frac{\partial h_j}{\partial x_j} \tag{3.3}$$

where τ_{ij} is the subgrid-scale stresses, P_r is the Prandtl number, h_j is the subgrid-scale heat fluxes and can be expressed as

$$h_j = \overline{u_j t} - \overline{u}_j \overline{T} \tag{3.4}$$

A detailed derivation of the governing equations is given in Appendix *A*.

3.2.2 Sub-grid Scale Models

SGS models are mainly used to simulate the small scales of motion in turbulent flow by connecting the *SGS* stresses τ_{ij} to the resolved variables. Some major *SGS* models are provided in the following section.

Smagorinsky Model

The Smagorinsky model was first introduced by Smagorinsky [91] and is still widely used currently. A length scale l_{SGS} is chosen as l_{SGS}=$C_s\Delta$, where C_s is the Smagorinsky constant, and Δ represents the filter width. The velocity scale is expressed as V_{SGS}=$l_{SGS}|S|$.

The eddy viscosity is then modelled as

$$\nu_t = l_{SGS}^2|\overline{S}| = (C_s\Delta)^2|\overline{S}| \tag{3.5}$$

where $\overline{S} = \frac{1}{2}(\partial\overline{U}_i/\partial x_j + \partial\overline{U}_j/\partial x_i)$, and $|\overline{S}| = (2\overline{S}_{ij}\overline{S}_{ij})^{1/2}$.

The effect of the filter scale motions are approximated using the eddy viscosity model :

$$\tau_{ij} = -2\nu_t\overline{S}_{ij} \tag{3.6}$$

The Smagorinsky model suffers two major drawbacks. Firstly, the Smagorinsky constant C_s is not certain and depends on the investigated flow and Reynolds number. Secondly, the filter scale stress produced by Smagorinsky model is proportional to the square of the velocity gradient. However, the turbulent fluctuations near the wall are very small and the flow eventually becomes laminar. Therefore, the Smagorinsky model in the vicinity of a wall will produce excessive dissipation, especially for transition problems [45]. To overcome this drawback, the length scale can be modified, according to Van Driest [115], as follows:

$$l_{SGS} = C_s\Delta(1 - e^{-y^+/A^+}) \tag{3.7}$$

where y^+ is the dimensionless wall distance, $y^+ = y\sqrt{\tau_w/\rho}/\nu$, and τ_w represents the wall shear stress. $A^+ = 25$ is a constant.

Yoshizawa Model

Lilly [46] gave a definition of the *SGS* characteristic velocity scale as

$$V_{SGS} = k_{SGS}^{1/2} = \tau_{kk}^{1/2} \tag{3.8}$$

where k_{SGS} is the *SGS* turbulent kinetic energy. Then the eddy viscosity can be rearranged as

$$\nu_t = \nu_{SGS} = C_k \Delta k_{SGS}^{1/2} \tag{3.9}$$

where C_k is a constant and the standard valus is taken as 0.07. Yoshizawa [126] provided the expression of the transport equation for k_{SGS} as

$$\rho \frac{\partial k_{SGS}}{\partial t} + \rho \frac{\partial \overline{u}_j k_{SGS}}{\partial x_j} = \frac{\partial}{\partial x_j}[(\mu + \mu_t)(\frac{\partial k_{SGS}}{\partial x_j})] + P_{k_{SGS}} - \rho\varepsilon \tag{3.10}$$

where $P_{k_{SGS}} = 2\mu_t S_{ij} S_{ij}$ and $\varepsilon = C_\varepsilon k_{SGS}^{1.5}/\Delta$ are production and dissipation terms, respectively. Yoshizawa [126] set the constant value of C_ε as 1.05.

This model contains more information in terms of the subgrid scales and is proved to have better performance than the Smagorinsky model when dealing with large-scale intermittency [83]. In both the internal cooling passages and labyrinth seals cases, the Yoshizawa model is used in conjunction with the *LANS*-α model, creating a mixed nonlinear *SGS* model as identified by Tyacke [109].

LANS-α Model

In *LES*, the energy transfer could involve nonlinear interactions between the resolved and unresolved scales. The shear layers generated by rib turbulators are unstable and anisotropic. The complex flow in labyrinth seals involves flow separation, high streamline curvature and numerous other unsteady phenomena. Therefore, a nonlinear *SGS* model is needed to model turbulence anisotropy and energy backscatter to make the prediction more accurate. A nonlinear model called the Lagrangian averaged Navier-Stokes (*LANS*)-α model has been proposed by Domaradzki and Holm [21], which is mathematically asymmetric and nonlinear. As reported by Geurts and Holm [29], the *LANS*-α model is able to capture turbulent shear layers better than the dynamic Smagorinsky model.

The stress τ_{ij} can generally be expressed as

$$\tau_{ij} = L + \overline{NL} \tag{3.11}$$

where L and $\overline{NL}$ represent the linear and nonlinear terms, respectively. The linear contribution to the *SGS* model stress is provided by the Yoshizawa model. The eddy viscosity μ_t for the *LANS*-α model is expressed as

$$\mu_t = \rho C_k \Delta k^{1/2} \tag{3.12}$$

Here an additional nonlinear term is added as *NL*. As provided in Kerr and Tucker [37], the nonlinear part for the stress τ_{ij} in this model can be expressed as

$$C_\alpha \rho \alpha^2 \left(\frac{\partial u_i}{\partial x_l}\frac{\partial u_l}{\partial x_j} + \frac{\partial u_i}{\partial x_l}\frac{\partial u_j}{\partial x_l} + \frac{\partial u_l}{\partial x_i}\frac{\partial u_l}{\partial x_j}\right) \tag{3.13}$$

where $\alpha = \Delta$ and l is an implicit summation. This nonlinear term is derived from the convection of *SGS* vorticity by the resolved scales. The process for this complex transformation can be found in Domaradzki and Holm [21].

The value of C_k is given in the Yoshizawa model. In this way, the contribution of the nonlinear components to the linear ones can be easily assessed.

3.3 NEAT Solver

For the flow in the internal cooling passages and labyrinth seal cavities in the current study, the governing equations are solved using the in-house *NEAT* code [108]. This *CFD* solver uses the finite volume method, and is presented by Tucker [108]. The first step in the finite volume method is to divide the domain into a grid. These discrete control volumes are compatible with the numerical techniques used to solve the governing flow equation. Structured grids are used in this study. With the use of *IBM*, the requirement to model complex geometries that contain curved surfaces can also be realized with little effort. Certainly, the unstructured grid systems can also fulfill the requirement, the overall computational cost, however, is greatly increased so as to deal with the transformed coordinates and grid systems [16].

After generating the grid, the main procedures are discretisation of the governing equations and solution of the algebraic equations with an iterative method. To parallelise the code, OpenMP (Open Multi-Processing) and *MPI* (Message Passing Interface) are implemented to speed up the simulation as provided by Tyacke [109].

3.3.1 Discretisation

The spatial discretisation in this code is performed using the finite volume method on a staggered grid system due to good conservation properties as required in *LES*. Figure 3.1 shows a one-dimensional grid system.

In the staggered grid system, the faces of control volumes are positioned mid-way between the adjacent nodes. The pressure is placed at the grid nodes whereas the velocity components

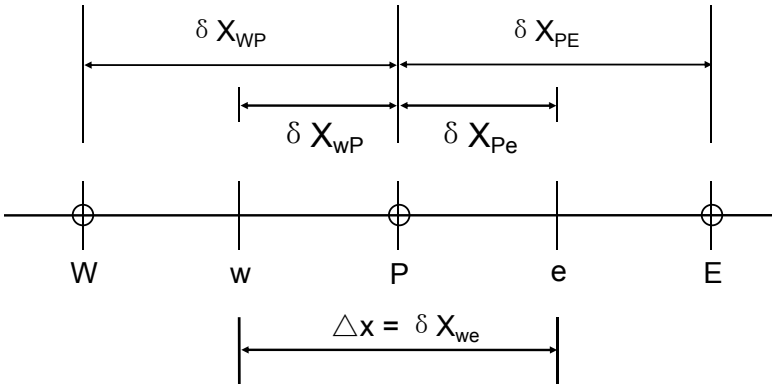

Fig. 3.1 A one-dimensional grid system.

are placed on the cell faces. Here P indicates the general nodal point and W and E indicate the nodes on its neighbours at the west and east respectively. Then the small w and e refer to the west and east face of the control volume. δX_{WP} and δX_{PE} show the distances between the nodes W and P, P and E respectively, and δX_{wP} and δX_{Pe} have the equivalent meaning. The control volume width in Figure 3.1 is $\Delta X = \delta X_{we}$.

After generating a suitable mesh, integration and discretisation of the governing equations over a control volume results in a discretised equation at the general point P. The integral form of the Navier-Stokes equations on finite volumes is fairly complex and will not be given in details here. After integration of all the partial differential equations, the general discretisation form for a two-dimensional system can be expressed as

$$a_P\phi_P = a_W\phi_W + a_E\phi_E + a_N\phi_N + a_S\phi_S + S_u \tag{3.14}$$

This equation is in a two-dimensional system, where ϕ is a general flow variable that represents velocity, pressure or temperature, a indicates the coefficients of the neighbouring nodes of the central node P: a_P represents the coefficient for cell P, a_W represents the coefficient for cell to the west of cell P, a_E represents the coefficient for cell to the east of cell P, a_N represents the coefficient for cell to the north of cell P, a_S represents the coefficient for cell to the south of cell P.

S_u is the source term of the control volume. In this study, periodic boundary conditions are applied for both flow and temperature fields in the streamwise direction. The mean temperature and pressure gradients for the periodic streamwise direction are given by α and β (see [59]). These are calculated using the following equations.

$$\beta_{new} = \beta_{old} - \rho\left(\frac{(Q_{new} - Q_0) - 0.5(Q_{old} - Q_0)}{0.5\Delta t Hz_{max}}\right) \tag{3.15}$$

$$\alpha = \frac{q''_w}{\rho c_p H U_0} \tag{3.16}$$

Here, Q_0 represents the volume flow rate, and Hz_{max} represents the cross sectional area of the channel. The subscripts "new" and "old" represent new and old time levels.

In the ribbed channel, the mean pressure gradient in Eqn (3.15) is used to drive the periodic flow. Heat from the streamwise direction is removed to prevent heat build up in the system via the constant heat flux q''_w. This constant heat flux is applied to the channel floor, whilst the surfaces of the rib and top wall of the channel are treated as adiabatic. At walls, no-slip and impermeability conditions are applied.

The derivation of the coefficients a_P, a_W, a_E, a_N, and a_S in Eqn (3.14) depends on the spatial and temporal discretisations used.

3.3.2 Spatial Discretisation

In order to obtain the estimation of the flow properties at the faces of the control volume and other terms, the second order central differencing scheme in *NEAT* is used and presented in the following.

The central differencing approximation has been used to compute the cell face values of property ϕ by linear interpolation - this is essential for high quality *LES*. For a uniform grid or control volume located in a distance between main nodes, the property ϕ are determined as

$$\phi_e = (\phi_P + \phi_E)/2 \tag{3.17}$$

$$\phi_w = (\phi_W + \phi_P)/2 \tag{3.18}$$

This scheme is simple to implement and has second-order accuracy. However, the utility of this scheme is restricted by the limitation of the Peclet number. This is because for high Peclet numbers, the Central Differencing Scheme (*CDS*) tends to be unstable and can cause oscillations into the flow. The Peclet number *Pe* is required to be less than 2 to ensure that the coefficients of the equations are positive, and thus the solution is stable and accurate. The Peclet number is defined as a measurement of the ratio of strengths between convection to diffusion:

$$Pe = \frac{\rho u}{\Gamma/\delta x} \tag{3.19}$$

where δx is the characteristic length.

However, often the solution may remain stable if this restriction is violated, as long as any instability does not grow too large. This is because the effective *Pe* induces the subgrid scale viscosity.

3.3.3 Temporal Discretisation

In the discretisation process of unsteady flows, an assumption is made to demonstrate how variables change with time. These assumptions can be written mathematically as

$$\phi = (1-\lambda)\phi^{old} + \lambda\phi^{new} \tag{3.20}$$

where λ is the weighting function, ϕ_{new} and ϕ_{old} are the corresponding values at new time and old time respectively. These different schemes can be determined based on the value of λ with 0, 0.5, 0.6 and 1 represent the explicit scheme, Crank-Nicolson scheme, Galerkin scheme and implicit scheme respectively.

In this study, the Crank-Nicolson scheme is used, which is second-order accurate in time and neutrally dissipative - essential for high quality *LES*. For unsteady flows, integrating over a control volume using the numerical methods for spatial and temporal terms, linear algebraic equations can be obtained. Although the Crank-Nicolson is regarded as stable for all values of time step, a small time step is necessary to ensure the accuracy of results. A Courant-Friedrichs-Lewy (CFL) number, $\Delta t U_{av}/\Delta x_{av} \approx 1$, is maintained thoughout the simulations.

3.3.4 The SIMPLE Algorithm

For imcompressible flow solvers, the velocity and pressure fields require coupling. The pressure velocity linkage can be resolved by employing an iterative solution strategy, namely the *SIMPLE* (Semi Implicit Method for Pressure-Linked Equations) algorithm, which was originally put forward by Patankar and Spalding [60]. In this algorithm the pressure field is first guessed to solve the momentum equations, then the guessed velocity field can be obtained. Furthermore, a pressure correction field is deduced from the continuity equation and is in turn used to find the velocity and pressure fields. To start the iteration process, the velocity or pressure fields are estimated initially and the process is iterated until converged solutions are obtained. In a two-dimensional flow, the discretised momentem euqations can be written as

$$a_{i,J}u_{i,J} = \Sigma a_{nb}u_{nb} + (p_{I-1,J} - p_{I,J})A_{i,J} + b_{i,J} \tag{3.21}$$

$$a_{I,j}v_{I,j} = \Sigma a_{nb}v_{nb} + (p_{I,J-1} - p_{I,J})A_{I,j} + b_{I,j} \tag{3.22}$$

where $A_{i,J}$ is the cell face area of the control volume and $b_{i,J}$ is the momentum source terms. By using the guessed pressure, P^*, the discretised momentum equations can be solved and yield the estimated velocity components u^* and v^* as follows:

$$a_{i,J}u^*_{i,J} = \Sigma a_{nb}u^*_{nb} + (p^*_{I-1,J} - p^*_{I,J})A_{i,J} + b_{i,J} \tag{3.23}$$

$$a_{I,j}v^*_{I,j} = \Sigma a_{nb}v^*_{nb} + (p^*_{I,J-1} - p^*_{I,J})A_{I,j} + b_{I,j} \tag{3.24}$$

To correct the variables u, v and p and the guessed variables u^*, v^* and P^* can be calculated. The corrections u', v' and p' can be expressed as:

$$u = u^* + u' \tag{3.25}$$

$$v = v^* + v' \tag{3.26}$$

$$p = p^* + p' \tag{3.27}$$

Substitution of the correct pressure field p into the momentum equations yields the correct velocity field u and v. Subtraction of the guessed field Eqn.(3.23) and (3.24) from the exact field Eqn.(3.21) and (3.22), the correction field can be found from:

$$a_{i,J}u'_{i,J} = \Sigma a_{nb}u'_{nb} + (p'_{I-1,J} - p'_{I,J})A_{i,J} \tag{3.28}$$

$$a_{I,j}v'_{I,j} = \Sigma a_{nb}v'_{nb} + (p'_{I,J-1} - p'_{I,J})A_{I,j} \tag{3.29}$$

To simplify these equations for the velocity corrections, a main approximation of the *SIMPLE* algorithm is made: the terms $\sum a_{nb}u'_{nb}$ and $\sum a_{nb}v'_{nb}$ can be neglected. This is because all of the coefficient contributions should roughly balance anyway. Thus the velocity correction can be expressed as:

$$u'_{i,J} = d_{i,J}(p'_{I-1,J} - p'_{I,J}) \tag{3.30}$$

$$v'_{I,j} = d_{I,j}(p'_{I,J-1} - p'_{I,J}) \tag{3.31}$$

where $d_{i,J}$= $A_{i,J}/a_{i,J}$ and $d_{I,j}$= $A_{I,j}/a_{I,j}$.

Substituting these equations into Eqns. (3.25)–(3.26), the actual velocity distributions are expressed as:

$$u_{i,J} = u^*_{i,J} + d_{i,J}(p'_{I-1,J} - p'_{I,J}) \tag{3.32}$$

$$v_{I,j} = v^*_{I,j} + d_{I,j}(p'_{I,J-1} - p'_{I,J}) \tag{3.33}$$

Similar expressions for $u_{i+1,J}$ and $v_{I,j+1}$ are:

$$u_{i+1,J} = u^*_{i+1,J} + d_{i+1,J}(p'_{I,J} - p'_{I+1,J}) \tag{3.34}$$

$$v_{I,j+1} = v^*_{I,j+1} + d_{I,j+1}(p'_{I,J} - p'_{I,J+1}) \tag{3.35}$$

This shows that the velocity field is subject to the pressure correction field p', it then can be further corrected by iteration of the procedure. Thus the momentum equations can be solved. To satisfy the continuity equation, the discretised form is given as:

$$[(\rho uA)_{i+1,J} - (\rho uA)_{i,J}] + [(\rho vA)_{I,j+1} - (\rho vA)_{I,j}] = 0 \tag{3.36}$$

Substituting the corrected velocities in Eqns. (3.32)–(3.35) into discretised continuity Eqn. (3.36) gives the pressure correction as:

$$a_{I,J}p'_{I,J} = a_{I+1,J}p'_{I+1,J} + a_{I-1,J}p'_{I-1,J} + a_{I,J+1}p'_{I,J+1} + a_{I,J-1}p'_{I,J-1} + b'_{I,J} \tag{3.37}$$

The coefficients are given below:

$$a_{I,J} = a_{I+1,J} + a_{I-1,J} + a_{I,J+1} + a_{I,J-1} \tag{3.38}$$

$$a_{I+1,J} = (\rho dA)_{i+1,J} \tag{3.39}$$

$$a_{I-1,J} = (\rho dA)_{i,J} \tag{3.40}$$

$$a_{I,J+1} = (\rho dA)_{I,j+1} \tag{3.41}$$

$$a_{I,J-1} = (\rho dA)_{I,J} \tag{3.42}$$

$$b'_{I,J} = (\rho u^* A)_{i,J} - (\rho u^* A)_{i+1,J} + (\rho v^* A)_{I,j} - (\rho v^* A)_{I,j+1} \tag{3.43}$$

By solving Eqn (3.37), the pressure correction field p' can be obtained at all points. Furthermore, the correct pressure field may be obtained using Eqn (3.27) and velocity components through correction Eqns. (3.32)–(3.35).

In practical computations, this method can cause numerical instability, especially for the pressure correction equation, which is susceptible to divergence. Thus some under-relaxation should be employed during the iterative process. The new and improved pressure at the central node P can then be obtained with

$$P^{new} = P^* + \alpha_P p' \tag{3.44}$$

where α_P is the pressure under-relaxation factor, and is considered within (0, 1]. In this work, α_P is taken as 0.7, and is used to add to the guessed field $p*$ a fraction of the correction field p' that is large enough for the iterative improvement process and at the same time small enough to ensure stable computations.

The velocities are also under-relaxed. The corresponding iteratively improved velocity components u^{new}, v^{new}, and w^{new} are expressed as

$$u^{new} = \alpha_u u + (1 - \alpha_u) u^{(n-1)} \tag{3.45}$$

$$v^{new} = \alpha_v v + (1 - \alpha_v) v^{(n-1)} \tag{3.46}$$

$$w^{new} = \alpha_w w + (1 - \alpha_w) w^{(n-1)} \tag{3.47}$$

where α_u, α_v, and α_w are the under-relaxation factors for u, v, and w respectively, and are taken as 0.7 for all these three directions. u, v, and w are the corrected velocity without relaxation and $u^{(n-1)}$, $v^{(n-1)}$, and $w^{(n-1)}$ represent the values obtained in the previous iteration.

In this study, the velocity is specified at the boundary. With the initial conditions, a converged solution can be obtained by repeating this guess-correct procedure with a sufficient number of iterations.

3.3.5 Solution of Equations

There are mainly two solution techniques for the linear algebraic equations, namely direct methods and iterative methods, respectively. As calculations for realistic CFD problems can be very large, the iterative methods can potentially be more computationally economical than direct methods. The solvers used in this code is the tri-diagonal matrix algorithm ($TDMA$).

TDMA Method

The $TDMA$ is able to solve multi-dimensional problems being applied iteratively, line-by-line and is widely used in CFD programs. It is an effective method and saves storage. The discretised equation can be rearranged in the following form

$$a_i\phi_i = b_i\phi_{i+1} + c_i\phi_{i-1} + d_i \tag{3.48}$$

where a_i, b_i, c_i and d_i contain the variable ϕ at node (i) and two neighbours at $(i-1)$ and $(i+1)$. d_i shows the corresponding source terms and the variable values on other nodes. For the geographic notation used previously, these coefficients would correspond to: $a_i = a_p$, $b_i = a_e$, $c_i = a_w$, d_i = remaining coefficients.

Take i = 1, 2, ... n, Eqn. (3.48) can be written as

$$\phi_1 = \frac{b_1}{a_1}\phi_2 + \frac{c_1}{a_1}\phi_0 + \frac{d_1}{a_1} \tag{3.49}$$

$$\phi_2 = \frac{b_2}{a_2}\phi_3 + \frac{c_2}{a_2}\phi_1 + \frac{d_2}{a_2} \tag{3.50}$$

$$\phi_n = \frac{b_n}{a_n}\phi_{n+1} + \frac{c_n}{a_n}\phi_{n-1} + \frac{d_n}{a_n} \tag{3.51}$$

These equations can be solved by forward elimination and back-substitution. For the back-substitution, the general form of relation can be expressed as:

$$\phi_i = P_i\phi_{i+1} + R_i \tag{3.52}$$

For the point left to i, the relation should be changed to:

$$\phi_{i-1} = P_{i-1}\phi_i + R_{i-1} \tag{3.53}$$

Substituting Eqn. (3.53) into Eqn. (3.48) to eliminate ϕ_{i-1}, the recurrence relations between P and Q can be given as:

$$P_i = \frac{b_i}{a_i - c_i P_{i-1}} \tag{3.54}$$

$$R_i = \frac{d_i + c_i Q_{i-1}}{a_i - c_i P_{i-1}} \tag{3.55}$$

This allows P and R at i to be expressed by P and R at point i-1. In order to start solving the system of equations, P and R are first identified at point i = 1 with c_1= 0.

$$P_i = \frac{b_i}{a_i} \tag{3.56}$$

$$R_i = \frac{d_i}{a_i} \tag{3.57}$$

Then cycling from i = 2 to $i = n$, the remaining values of P and R can be subsequently calculated by forward substitution. As the value at point $n+1$ is known through boundary condition, the values of P and R for ϕ can then be obtained in back-substitution (ϕ_n, ϕ_{n-1}, ϕ_{n-2},..., ϕ_2) by using Eqn. (3.53). This procedure is then repeated in each of the coordinate direction to make sure that the entire domain is solved.

As the periodic boundary conditions are employed in the x and z directions for the internal cooling passages and labyrinth seals cases, a corresponding modified algorithm is then applied on the above standard *TDMA*, namely Cyclic *TDMA* and was proposed by Patankar et al. [59].

The Cyclic TDMA

When a periodic boundary conditions is employed

For i = 1, $\phi_{i-1} = \phi_n$

for i = n, $\phi_{i+1} = \phi_1$.

Thus, Eqn. (3.49) can be rewritten as

$$\phi_1 = \frac{b_1}{a_1}\phi_2 + \frac{c_1}{a_1}\phi_n + \frac{d_1}{a_1} \tag{3.58}$$

Substituting Eq. (3.58) into Eq. (3.50), we can get

$$\phi_2 = \frac{b_2}{a_2 - c_2\frac{b_1}{a_1}}\phi_3 + \frac{c_2\frac{c_1}{a_1}}{a_2 - c_2\frac{b_1}{a_1}}\phi_n + \frac{d_2 + c_2 d_1}{a_2 - c_2\frac{b_1}{a_1}} \tag{3.59}$$

Then cycling from i = 2 to $i = n$, the general form can be expressed as:

$$\phi_i = P_i\phi_{i+1} + Q_i\phi_n + R_i \tag{3.60}$$

For $i = 2 \sim n$,

$$P_i = \frac{b_i}{a_i - c_i P_{i-1}} \tag{3.61}$$

$$Q_i = \frac{c_i Q_{i-1}}{a_i - c_i P_{i-1}} \tag{3.62}$$

$$R_i = \frac{d_i + c_i Q_{i-1}}{a_i - c_i P_{i-1}} \tag{3.63}$$

For $i = 1$,

$$P_i = \frac{b_i}{a_i} \tag{3.64}$$

$$Q_i = \frac{c_i}{a_i} \tag{3.65}$$

$$R_i = \frac{d_i}{a_i} \tag{3.66}$$

When $i = n$, Eqn. (3.48) is written as

$$\phi_n = \frac{b_n}{a_n}\phi_{n+1} + \frac{c_n}{a_n}\phi_{n-1} + \frac{d_n}{a_n} \tag{3.67}$$

Substituting Eqn. (3.58) for ϕ_1 into Eqn. (3.67), then successively for ϕ_2, ϕ_3, ... ϕ_{n-1} until ϕ_n is the only unknown coefficient in the equation, then ϕ_n can be expressed as

$$\phi_n = \frac{(F_{n-1} + c_n)R_{n-1} + G_{n-1}}{E_{n-1} - (F_{n-1} + c_n)(P_{n-1} + Q_{n-1})} \tag{3.68}$$

where

$$E_i = E_{i-1} - F_{i-1}Q_{i-1} \tag{3.69}$$

$$F_i = F_{i-1} P_{i-1} \tag{3.70}$$

$$G_i = G_{i-1} + F_{i-1} Q_{i-1} \tag{3.71}$$

For $i = 1$, $E_1 = a_n$, $F_1 = b_n$, and $G_1 = d_n$. Then calcuting backward, ϕ_{n-1}, ... ϕ_1 can be obtained.

3.4 IBM Theory

Immersed Boundary Methods can be used to represent geometry on a simplified background mesh. Take the complex geometry in Figure 3.2 as an example. This curved geometry is superimposed on a structured grid. The resulting cut cell shapes can be a triangle, a quadrangle, or a pentagon. All the structured nodes are divided into three groups: fluid cell, solid cell and ghost cell. The non-boundary nodes that possess only one attribute are prescribed as solid cells or fluid cells. For boundary nodes that possess more than one attribute, the cells which have their centre outside the boundary surface are also taken as fluid cells; the cells which have their centre within the solid domain are defined as ghost cells. However, sometimes solid cells near the boundary are also chosen as ghost cells. Take the cell at $(i+1;\ j)$ as an example. The cells at $(i,\ j)$ and $(i-1,\ j-1)$ are ghost cells. However, the neighbor cells at $(i+1,\ j+1)$ is a fluid cell, and $(i+1,\ j-1)$ is a solid cell. In this situation the cell at $(i+1;\ j)$ is chosen as a ghost cell.

As the computational grid does not coincide with the surface, to generate the complex geometry, the boundary condition at the surface needs to be implicitly imposed. For the fluid cells that are located inside the fluid domain the fluid properties can be easily known from the *NEAT* solver. For the solid cells that are located entirely inside the solid domain nothing needs to be done with these cells as they are not involved in the simulation. Thus an interpolation procedure is required to represent the flow property (e.g. velocity or temperature) at the ghost cells. Given that the flow property of the cell outside the boundary is generally positive, the immersed boundary node will generally need to be negative to ensure the zero contour. This process is repeated to set the velocity at the boundary surface to be zero in all directions. As a result the desired boundary shape is generated. This whole procedure to achieve the value of the flow property at the immersed boundary node is known as 'reconstruction'. Here, two higher order reconstruction methods are introduced, which are:

1. Full linear reconstruction

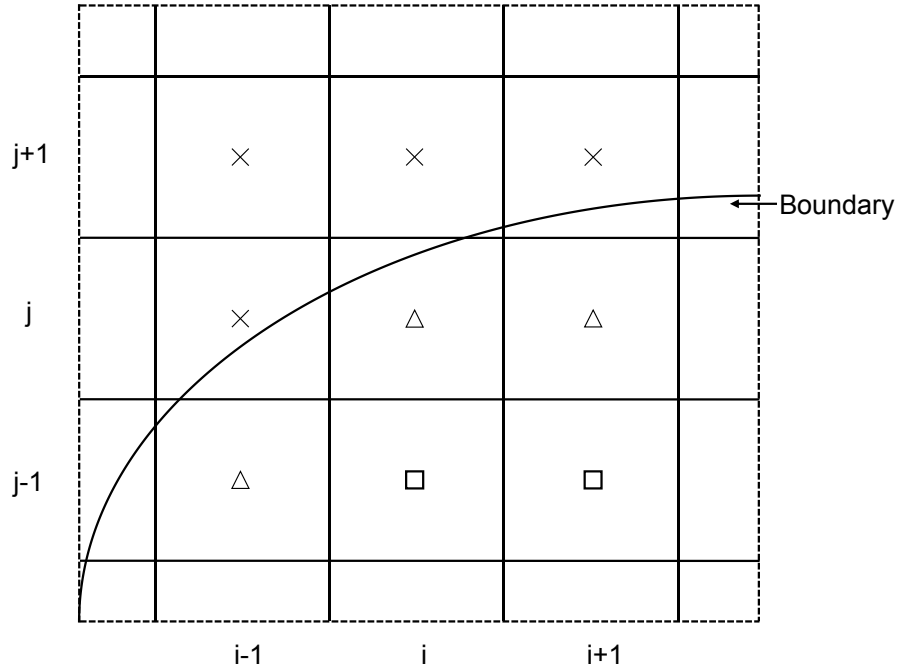

Fig. 3.2 The Immersed Boundary Method: × Fluid Cell, □ Solid Cell, △ Ghost Cell.

2. Quadratic reconstruction

3.4.1 Higher Order Reconstruction Methods

Full Linear Reconstruction

The flow property ϕ in this method is assumed to follow a linear plane near the ghost cell, as shown in Figure 3.3. O is chosen as the nearest interior point on the boundary to G. $X1$ & $X2$ are the two fluid-neighbor point. $GX1X2$ forms a linear plane containing the boundary point O. As $X1$ and $X2$ are among the fluid domain, the corresponding flow property ϕ can be easily known. The value of ϕ at O is set as zero. Recall the definition for a linear plane:

$$\vec{r} \cdot \vec{N} = \vec{a} \cdot \vec{N} \tag{3.72}$$

Here, $\widetilde{r}$ represents the general vector to a point on the plane, $\widetilde{N}$ represents a vector normal to the plane and $\widetilde{a}$ is suggested as a known point on the plane.

Within the context of bilinear interpolation schemes, in the literature, especially the work of Tseng and Ferziger [104], the flow property ϕ at point G is calculated by interpolating the value at the neighboring points $X1$, $X2$ to the no-slip point O by using the above vector equation. This process is repeated to solve the property value for every ghost cell and for every time step. Take the computation time into consideration, a new formulation is hence

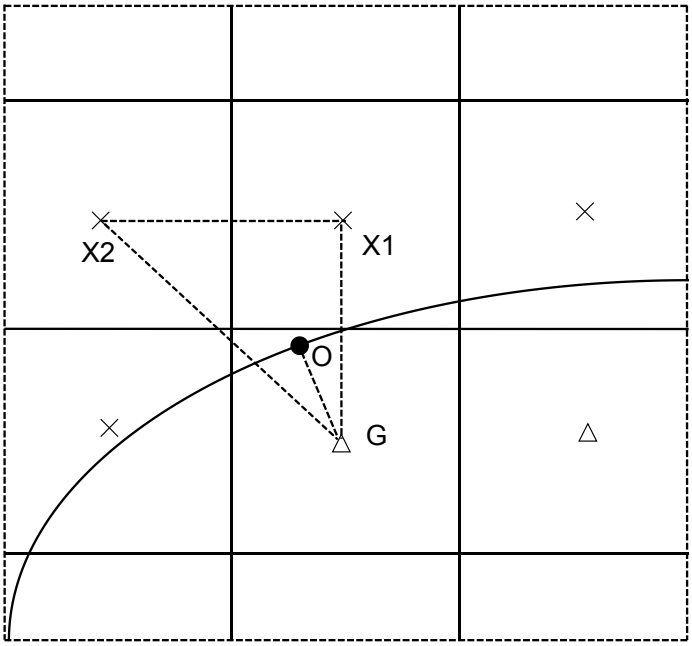

Fig. 3.3 A schematic of full linear reconstruction.

produced to find a general solution to the vector relationship in Eqn. (3.72). The contributions of the surrounding fluid nodes can be simplified into a set of coefficients. In this case these coefficients are calculated at the beginning of the simulation and then can be easily used during the solution process. Eqn. (3.72) then can be represented using the column vector form:

$$\begin{pmatrix} x \\ y \\ \phi \end{pmatrix} \begin{pmatrix} N_x \\ N_y \\ N_\phi \end{pmatrix} = \begin{pmatrix} a_x \\ a_y \\ a_\phi \end{pmatrix} \begin{pmatrix} N_x \\ N_y \\ N_\phi \end{pmatrix} \tag{3.73}$$

The coordinates of points $X1$, $X2$, and O are (x_O, y_O), (x_{X1}, y_{X1}) and (x_{X2}, y_{X2}). Then the vector equation can be expressed as follows:

$$N_x = y_{OX1}\phi_{OX2} - \phi_{OX1}y_{OX2} \tag{3.74}$$

$$N_y = x_{OX2}\phi_{OX1} - \phi_{OX2}x_{OX1} \tag{3.75}$$

$$N_\phi = x_{OX1}yOX2 - xOX2y_{OX1} \tag{3.76}$$

Here, ϕ_O, ϕ_{X1} and ϕ_{X2} are denoted as the flow property at these points, and

$$x_{OX1} = x_{X1} - x_O \tag{3.77}$$

$$x_{OX2} = x_{X2} - x_O \tag{3.78}$$

$$y_{OX1} = y_{X1} - y_O \tag{3.79}$$

$$y_{OX2} = y_{X2} - y_O \tag{3.80}$$

$$\phi_{OX1} = \phi_{X1} - \phi_O \tag{3.81}$$

$$\phi_{OX2} = \phi_{X2} - \phi_O \tag{3.82}$$

The value of ϕ at point G can be obtained using the following relation:

$$\phi_G = C_{X1}\phi_{X1} + C_{X2}\phi_{X2} + C_O\phi_O \tag{3.83}$$

Substitution of the above relations gives the coefficients C_{X1} and C_{X2} as:

$$C_{X1} = \frac{(y_O - y_G)x_{OX2} - (x_O - x_G)y_{OX2}}{x_{OX1}y_{OX2} - x_{OX2}y_{OX1}} \tag{3.84}$$

$$C_{X2} = \frac{(x_O - x_G)y_{OX1} - (y_O - y_G)x_{OX1}}{x_{OX1}y_{OX2} - x_{OX2}y_{OX1}} \tag{3.85}$$

The key point of this method is the selection of the $X1$ and $X2$ points, because there becomes an infinite number of planes that can pass through O, $X1$ and $X2$ if O moves closer to the line $X1X2$. In that situation the coefficients will turn out to be very large. The solution to this problem is either to move $X1$ or $X2$ or set $X1$ or $X2$ as a new ghost cell. Here we opt for the second method.

Quadratic Reconstruction

This method is similar to the full linear reconstruction except a proposed quadratic interpolation is used to correct the values of ϕ at the ghost cell using the values at the five nearest fluid nodes and the boundary point. The computational procedure proposed by Tseng and Ferziger [104] is as follows.

$$\phi = a_0 + a_1 x + a_2 y + a_3 x^2 + a_4 xy + a_5 y^2 \tag{3.86}$$

the coefficients can be found from the matrix equation:

$$a = B^{-1}\phi \tag{3.87}$$

where

$$B = \begin{bmatrix} 1 & x_O & y_O & x_O^2 & x_O y_O & y_O^2 \\ 1 & x_{X1} & y_{X1} & x_{X1}^2 & x_{X1} y_{X1} & y_{X1}^2 \\ \dots & \dots & \dots & \dots & \dots & \dots \\ 1 & x_{X5} & y_{X5} & x_{X5}^2 & x_{X5} y_{X5} & y_{X5}^2 \end{bmatrix} \tag{3.88}$$

$$\phi = \begin{bmatrix} \phi_O \\ \phi_{X1} \\ \dots \\ \phi_{X5} \end{bmatrix} \tag{3.89}$$

The value of ϕ at any point can be represented as a weighted combination of the values of ϕ at the surrounding points:

$$\phi = C_{X1}\phi_{X1} + C_{X2}\phi_{X2} + C_{X3}\phi_{X3} + C_{X4}\phi_{X4} + C_{X5}\phi_{X5} + C_O\phi_O \tag{3.90}$$

Thus, the coefficients can be calculated from the above equation.

The employed scheme determines the degree of accuracy of the *IBM*. In this work, the quadratic reconstruction is used giving 4^{th} order accuracy. With the use of the quadratic reconstruction, a full consistency can be obtained.

3.4.2 Settings on the Boundary

As discussed in section 3.3, the *SIMPLE* algorithm is used to solve the pressure and velocity separately. This allows the velocity and pressure of each ghost cell to be calculated sequentially. The algebraic equation systems are solved iteratively using the *TDMA* algorithm.

Consider the discretized flow equation as follows:

$$A_p\phi_p = A_n\phi_n + A_s\phi_s + A_e\phi_e + A_w\phi_w + S_\phi \tag{3.91}$$

The coefficients at the ghost cell are set as $A_p = 1, A_n, A_s, A_e, A_w = 0$ and $S_\phi = \phi_G$. This has the effect of isolating the ghost cells from surrounding cells numerically. Substitution into the solver equations in Section 3.3.5, a new relationship is obtained:

$$\phi_p = \phi_G \tag{3.92}$$

This process is then updated for every sweep of the solver algorithm to allow the flow properties of the ghost cell to continually impose the position of the boundary. The ghost cells are never more than one sub-iteration behind the main fluid simulation. Thus an accurate surface is preserved.

Pressure Treatment

The pressure can be updated according to the solution of the local flow field without any interference from the *IBM*. Although acceptable results can be obtained, areas of high pressure can be found within the surface. This is because ghost cell values are forced directly to suit the local flow, which resulting in continuity violations. Thus the pressure needs a better treatment. The pressure at the ghost cells could be evaluated using an arithmetic average of the pressures at points in the local pressure field. Take the two fluid nodes, $X1$ and $X2$ (Figure 3.3) as an example. If the surface point lies on the line between the ghost cell and point $X1$ then the pressure at $X1$ will be applied to the ghost cell; if the surface lies on a line between $X2$ and G, the pressure can then be taken as the pressure at the ghost cell. Between these two extreme situations, here, we take the pressure as a weighted combination of the above two situations. As this method has the advantage to eliminate large pressure spots within the surface, it is able to model a surface with much more accuracy.

3.5 Conclusions

The main properties of turbulence and the *LES* model are described in this chapter. The flow involved in the internal cooling passages and labyrinth seals are highly unsteady and complex. Thus, a mixed nonlinear *SGS* model is used which is capable to model this type of flow more accurately. The *CFD* solver, *NEAT*, is also described in detail. The *SIMPLE* algorithm is used to solve coupled velocity and pressure. Two types of *TDMA* solution method used here for systems of algebraic equations are provided (standard *TDMA* and the cyclic *TDMA* depending on boundary conditions considered). A Cartesian grid is used in this study for the sake of saving computational cost. The requirement to model complex geometries that

containing curved surfaces can be easily realized with the use of *IBM*. A particular quatratic reconstruction method is chosen for the higher order of accuracy.

Chapter 4

Geometrical Impact for Internal Cooling Passages

4.1 Introduction

Large eddy simulations (*LES*) are used to explore the impact of different rib shapes on heat transfer in a fully-developed ribbed channel. Different rib shapes are investigated with the aim being to improve the heat transfer rate and reduce the total pressure loss. The rib geometries considered in this study are shown in Figure 4.1, which are square, perforated, triangular with increasing height in the flow direction, triangular with decreasing height in the flow direction, pentagonal with increasing height in the flow direction, pentagonal with decreasing height in the flow direction, house-shaped, groove-shaped, semi-circular, and arc. To validate the accuracy of the current *LES* model, the square rib case is first studied using the *NEAT* code developed by Tucker [108], and the results are compared against the measurements made by Acharya et al. [1]. An immersed boundary method (*IBM*) is used with *LES* for complex rigid geometries. To illustrate the capability of the *IBM*, three benchmark cases have been applied. The results of heat transfer distribution for each case are then discussed in detail. The heat transfer performance is further calculated with respect to the friction coefficient. This shows the best performing rib geometry to be found.

4.2 Computational Setup

4.2.1 Computational Model

Figure 4.2 shows the computational domain used in this study. It is a straight channel with fully-developed flow over the rib surfaces. The ribs are placed perpendicular to the flow

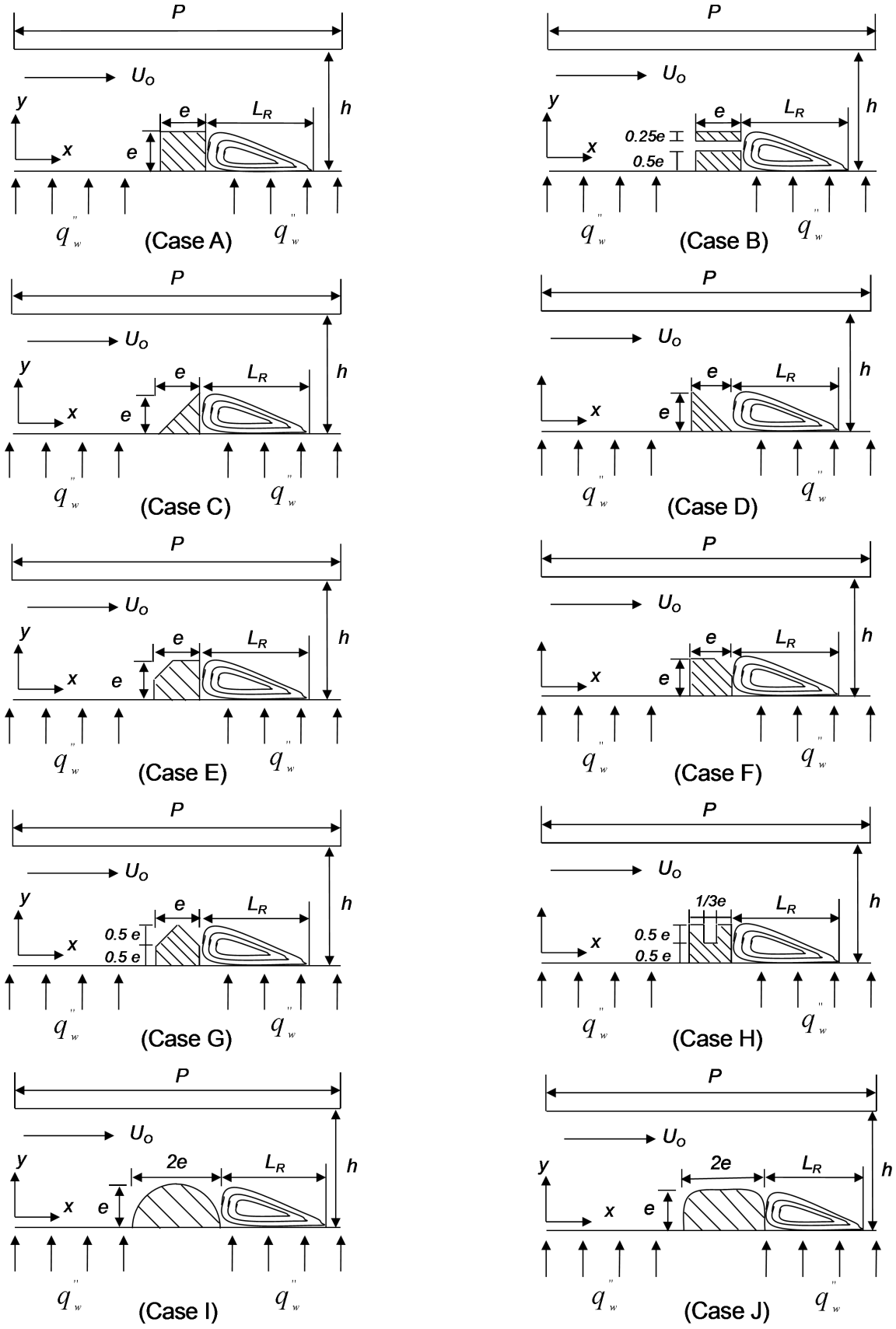

Fig. 4.1 Schematics of the channel with different rib geometries: (Case *A*) Square; (Case *B*) Perforated; (Case *C*) Triangular_up; (Case *D*) Triangular_down; (Case *E*) Pentagonal_up; (Case *F*) Pentagonal_down; (Case *G*) House-shaped; (Case *H*) Groove-shaped; (Case *I*) Semi-circular; (Case *J*) Arc.

direction at the center of the bottom wall. The settings for the flow parameters were chosen to be consistent with the experiments of Acharya et al. [1]. The test conditions are summarised in Table 4.1. Here, e denotes the height of the square rib, as shown in Figure 4.2. The baseline geometry and general case set up is similar to that of Tafti [97] and Liu et al. [49]. Figure 4.1 presents schematics of the symmetrical channel with the different rib geometries considered. Periodic boundary conditions are imposed in both the streamwise and spanwise directions.

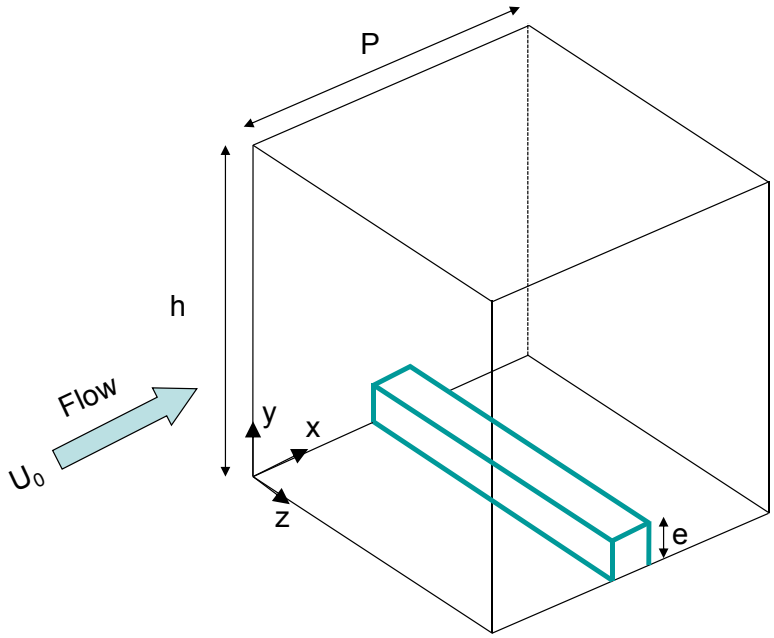

Fig. 4.2 Three-dimensional computational domain (aspect ratio=1).

Table 4.1 Flow parameters for the ribbed channel

Re	P (m)	h (m)	U_0(m/s)	e (m)	D_h (m)
14,200	0.127	0.061	3.5	0.00635	0.1016

Figure 4.3 shows the grid independency with the square rib. The results from the three sizes of grids are almost equivalent except for the coarse one (0.35M) that shows a different behavior further downstream of the rib. Compared with variations of 4% between the coarse grid and the modest grid, variations of 2% between the modest grid and the fine grid are considered acceptable, especially considering that computational costs are doubled. Thus, the modest grid is chosen, with $160 \times 100 \times 62$ nodes in the x, y and z directions, respectively. Note, as also shown by Tyacke [109], such a grid is sufficient for grid independent solutions.

Figure 4.4 shows the structured mesh of the computational domain used in this study. The grid distribution is uniform in the z direction. In the $x-$ and $y-$ directions, more cells are applied around the rib and in the near wall region. The refined grid is intended to capture the turbulent shear layer and smaller scales near the wall. These regions are crucial to accurately predict the turbulence and heat transfer. The simulations for the various rib geometries are carried out in the *NEAT* code using grid spacing similar to this modest grid system.

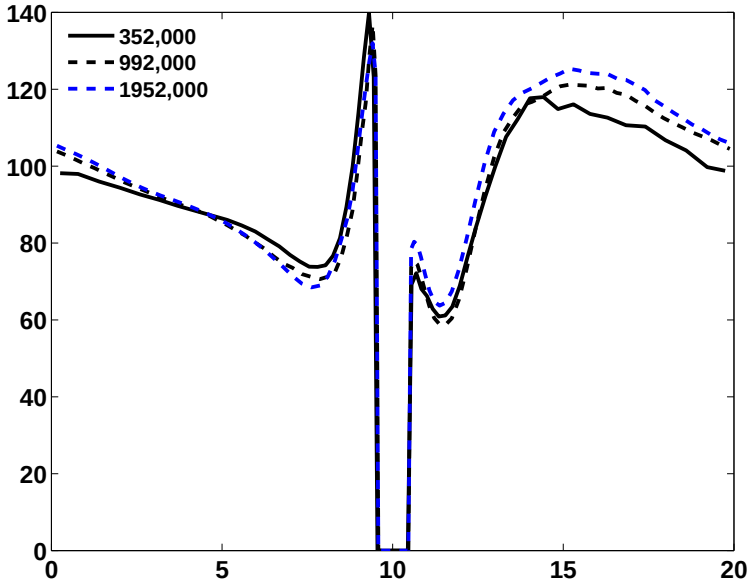

Fig. 4.3 Grid dependency test.

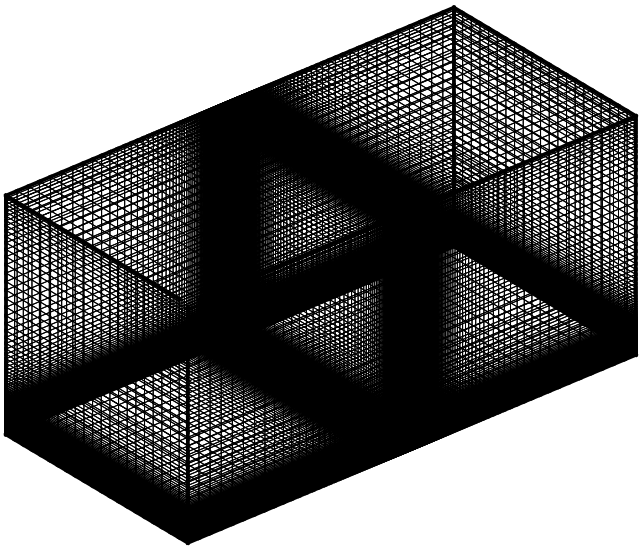

Fig. 4.4 Structured grid mesh of the computational domain.

4.2.2 Boundary Conditions

In the experiments, a heater mat was used on the channel floor and Balsa wood was used for convenience to represent the ribs in the channel. To match these experiments, no slip conditions are imposed at the wall. The rib surfaces and the upper wall are assumed to be adiabatic and a constant heat flux (q'') boundary condition is applied on the remaining channel floor. The fully developed flow is homogeneous in the spanwise directions and periodic in the streamwise direction. Periodic boundary conditions are imposed in these directions. The governing energy equation is non-dimensionalised by a characteristic temperature scale given by $q''D_h/k$. The assumed periodic domain in the streamwise direction requires that the mean gradients of pressure and temperature be isolated from the fluctuating periodic components as follows:

$$p(\vec{x},t) = p_{in} - \beta x + p'(\vec{x},t), \tag{4.1}$$

$$T(\vec{x},t) = T_{in} + \gamma x + \theta(\vec{x},t), \tag{4.2}$$

where β is the mean pressure gradient, p' is the fluctuating pressure, γ is the mean temperature gradient, and θ is the fluctuating temperature.

4.2.3 Development Time

The non-dimensional time step, which is defined as $\Delta t^* = \Delta x_{min}/U_{max}$, is set as 1×10^{-4} in the current study, giving a CFL of 0.7. The initial flow is assumed to have a uniform velocity in the channel at $U_O \approx 3.5$ m/s (the mean streamwise velocity). For all cases, the simulation is first allowed to develop for approximately five through-flow periods to achieve a fully developed turbulent flow. Then the time-averaged values, such as velocities and Nusselt numbers are obtained for another five periods giving a statistically stationary state.

4.3 Validation of IBM

IBM is used with *LES* for the more complex geometries. Three numerical benchmark cases were tested to to validate the accuracy of the *IBM*: (i) the flow in a plane channel skewed to the computational grid lines, (ii) wall-driven flow in an inclined box, (iii) the flow around a circular cylinder in a channel. The corresponding schematic of geometries is shown in Figure 4.5.

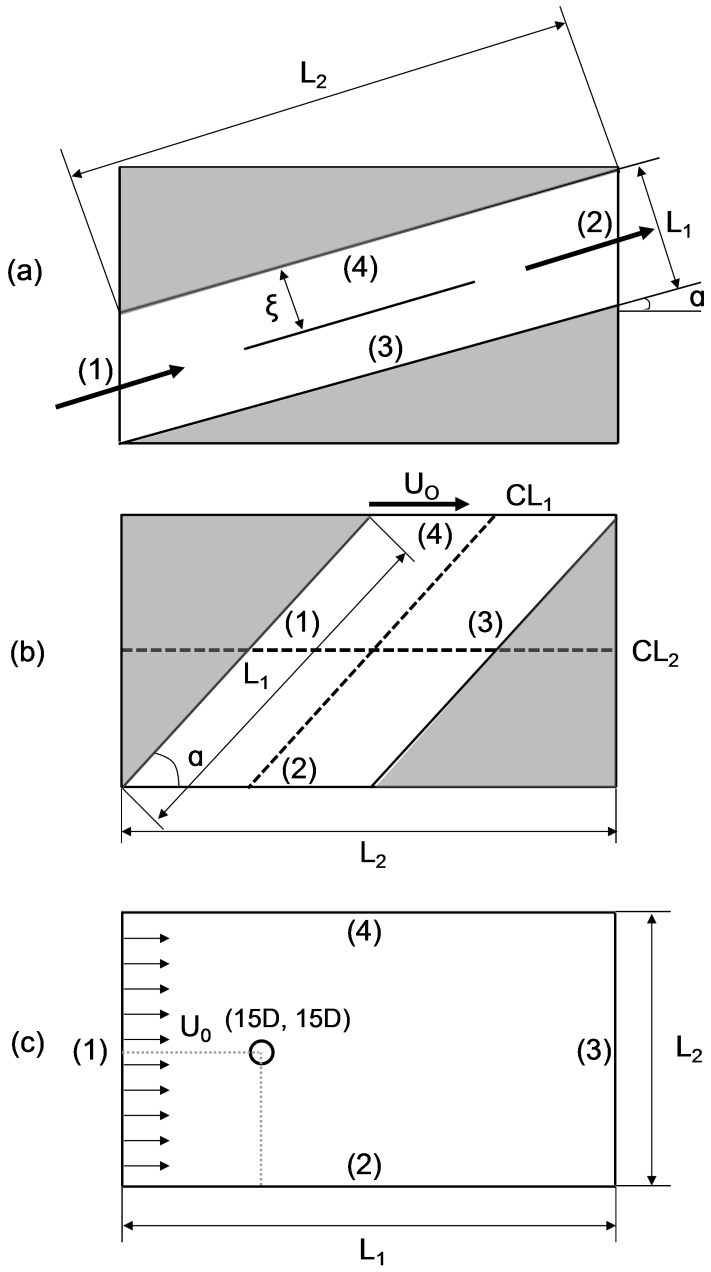

Fig. 4.5 Schematic of geometries considered: (a) flow in an inclined channel; (b) inclined driven cavity; (c) flow past a cylinder.

4.3.1 Case I – Flow in an Inclined Channel

For Case *I*, as illustrated in Figure 4.5(a), $L_1 = L_2/2$ and α is taken as 10°, 20° and 30°. For boundaries (3) and (4) no-slip and impermeability conditions are applied. At the inlet and outlet (boundaries (1) and (2)), a parabolic velocity profile is imposed. The grids consist of 81×101 nodes.

$$\frac{u}{U_0} = \frac{3}{2}(1 - 4\frac{\zeta^2}{L_1^2}) \tag{4.3}$$

where U_0 is the average fluid velocity and ζ is the distance from the channel centre line.

The average friction factor f is computed for each of the three channel angles. The friction factor is defined as $f = \tau_w/(\rho \mathrm{U}_0^2/2)$, where τ_w is the wall shear stress. As shown in Figure 4.6, agreement can be found when compared with the analytical value for laminar skin friction in a fully developed channel flow.

4.3.2 Case II – Lid-driven Inclined Cavity Flow

Lid-driven cavity flows are popular benchmark test cases. Demirdžić et al. [17] applied non-orthogonal grids to this benchmark case for a skewed cavity. Further, Tucker and Pan [107] solved the same problem using the Cartesian cut cell approach. The geometry is shown in Figure 4.5(b). The flow field is driven by a constant lid velocity U_0 at boundary (4). To be consistent with the data by Demirdžić et al. [17] and Tucker and Pan [107], *Re* is set as 100. L_2 is chosen as the characteristic length and set as $L_2 = L_1 = 1$, the inclination angle α being 45°. At boundaries (1)–(3), no-slip and impermeability conditions are applied. Grids of 80 × 33 are used in this case.

The velocity profiles u and v are predicted along the centerlines $CL1$ and $CL2$. Figure 4.7(a) shows the dimensionless axial velocity variation against the dimensionless vertical coordinate. Figure 4.7(b) gives the horizontal variation of the dimensionless vertical velocity. As can be seen from the comparisons, acceptable consistency is found with the benchmark data from Demirdžić et al. [17], demonstrating that the *IBM* code is correctly built. Figure 4.8 gives streamlines for the flow. Two vortices can be seen, the weaker one being in the left hand lower cavity corner. These are consistent with the predictions by Demirdžić et al. [17].

4.3.3 Case III – Flow Over a Circular Cylinder

The third case investigates flow past a circular cylinder in a rectangular domain with Cartesian meshes. The computational configuration is shown in Figure 4.5(c). To test this *IBM* on a steady laminar flow and an unsteady flow the simulations were performed at two Reynolds

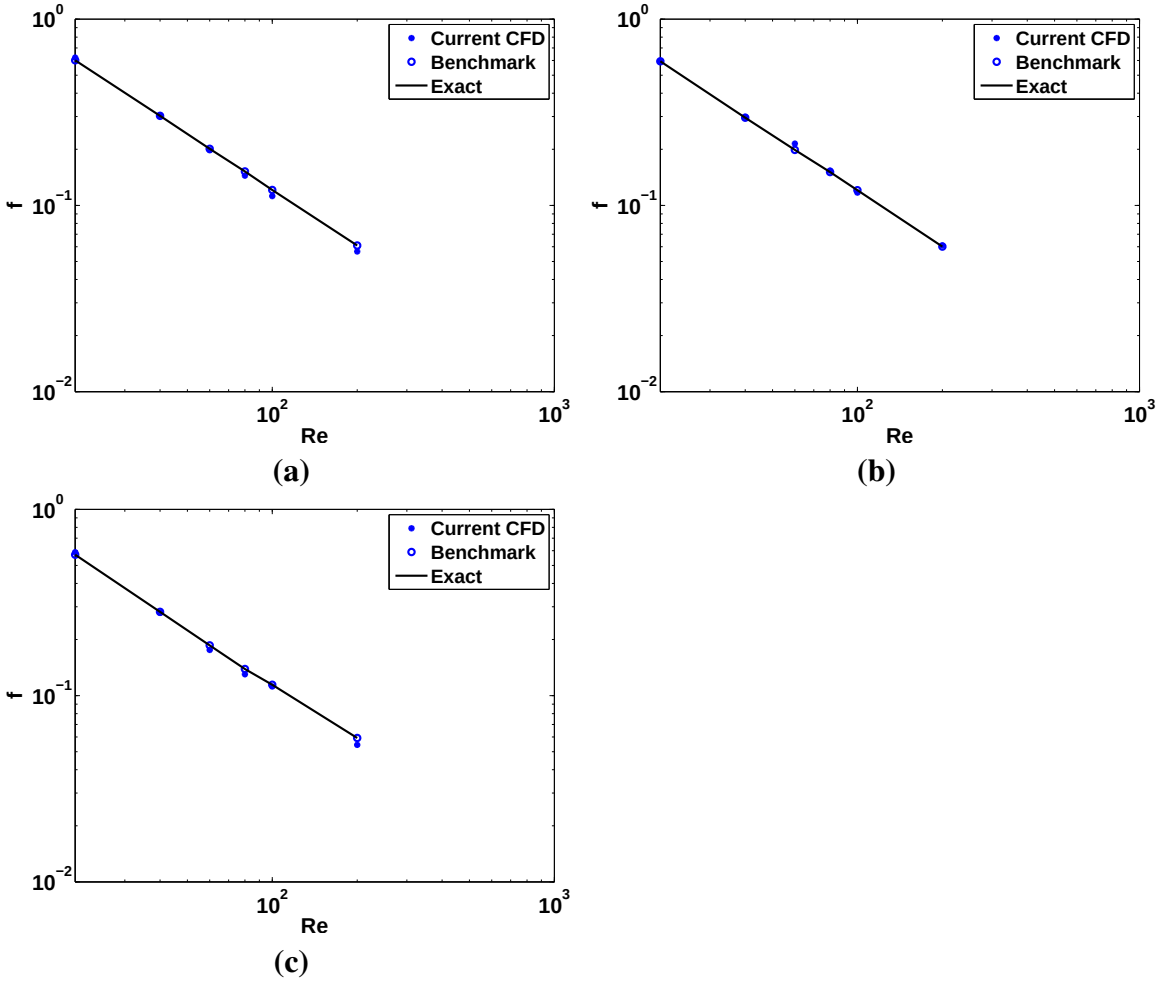

Fig. 4.6 Average friction factor in an inclined channel for different angles: (a) 10°; (b) 20°; (c) 30°.

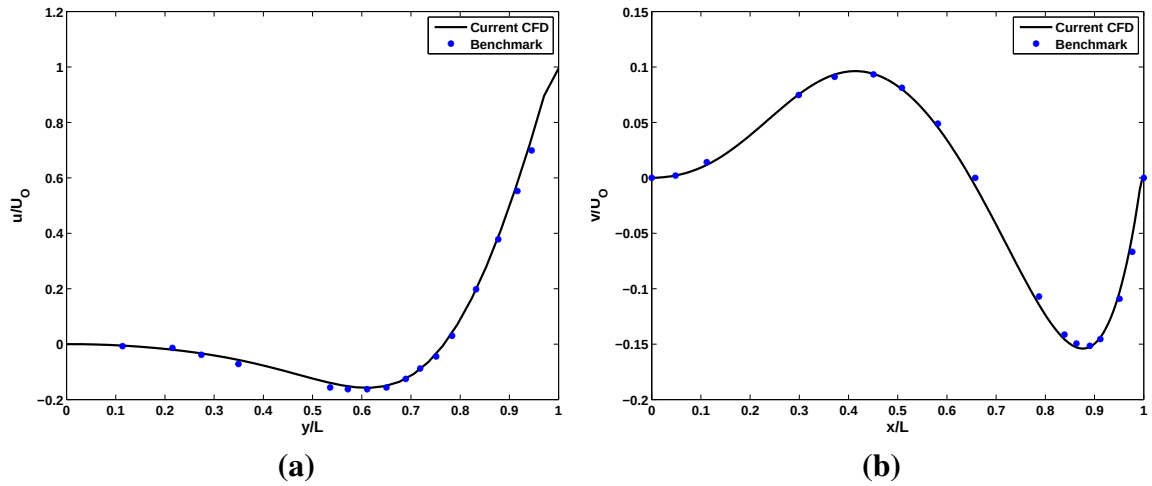

Fig. 4.7 Velocity profiles in an inclined cavity. (a) u velocity profile along vertical center line; (b) v velocity profile along horizontal center line.

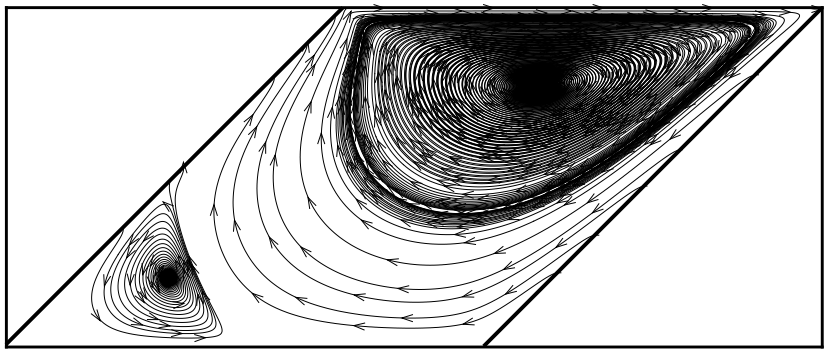

Fig. 4.8 Streamlines of flow in the inclined cavity.

numbers of 40 and 100. The characteristic length is the diameter of the cylinder (D) and the constant velocity U_0 at the inlet is set as 0.368 m/s for the Re=40 case and 0.92 m/s for the Re=100 case. No-slip and impermeability conditions are applied at boundaries (2) and (4). The cylinder is placed inside the flow domain at x=15 D, y=15 D. The cylinder diameter is 1.58 mm and the grid consisted of just 10 nodes across the diameter of the cylinder. The coarse grid is intended to really challenge the *IBM* treatment. The mesh consists of 151×76 nodal points in the streamwise (x) and transverse (y) directions. The corresponding Cartesian mesh is shown in Figure 4.9 with every 2^{nd} line plotted.

Streamtrace plots and vorticity contours are shown in Figure 4.10. Streamlines around the cylinder at Re=40 are shown in Figure 4.10(a), where two symmetrical vortices are stationarily attached behind the cylinder. The separation bubble behind the cylinder illustrates that the flow reaches a steady symmetrical state. The dimensionless wake length L_w/D = 2.3. This is consistent with the value 2.27 from Huang and Sung [32]. Note, the mesh used in this *IBM* is much less than the body-fitted grid used by Schäfer et al. [85]. When $Re \geq 47$, the cylinder wake becomes to be instable and vortex lengths appear to reduce. For Re=100, the vortices become unstable and start to shed alternately behind the cylinder. This phenomenon is shown in the sequence of streamlines plots in Figure 4.10(b), and it is clear that vortices of opposing polarity are shed alternately downstream.

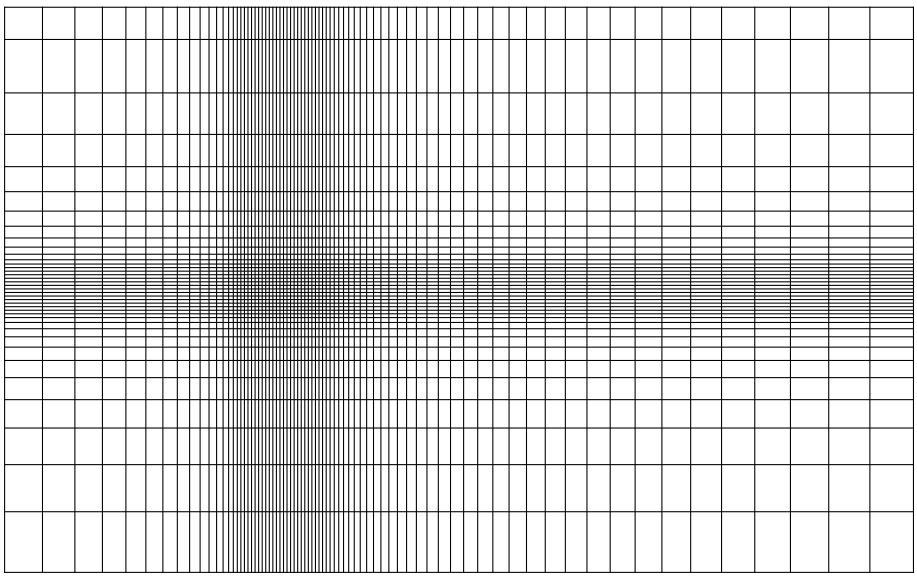

Fig. 4.9 Mesh of the cylinder case (with every 2^{nd} grid line plotted).

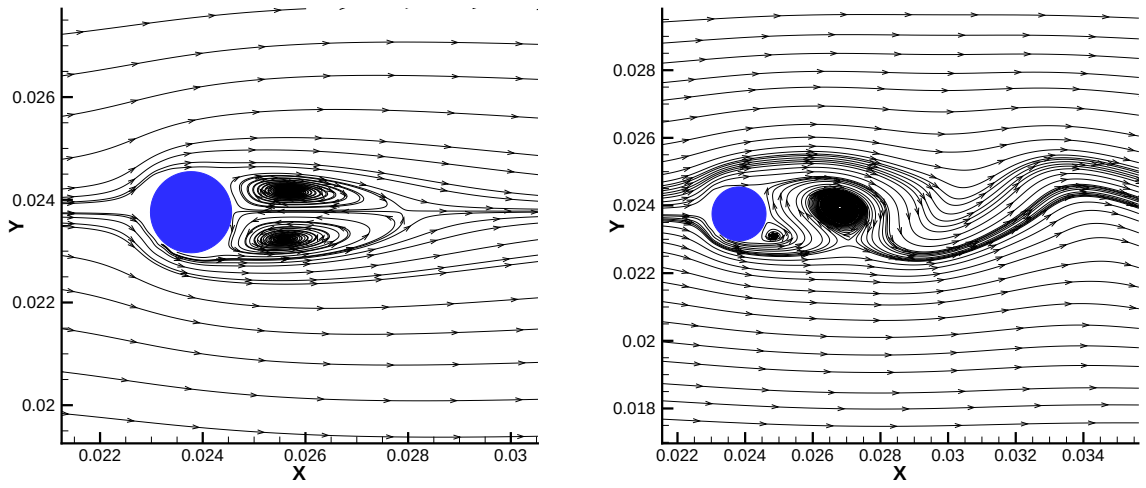

Fig. 4.10 Streamtrace plots over a cylinder: (a) *Re*=40 and (b) *Re*=100.

4.4 Baseline Square Case

4.4.1 Validation of LES

To validate the accuracy of the current *LES* model, as noted earlier the nonlinear *LANS-*α model, the baseline square rib case is first considered. The mean velocity is compared with the measurements made by Acharya et al. (1993). Figures 4.11(a)–4.11(d) present comparisons of the mean streamwise velocity, cross-stream velocity, streamwise velocity fluctuations and cross-stream velocity fluctuations, respectively. The plots are shown at seven different locations: x/e= 2.3, 10, 10.5, 11.1, 13.6, 16.2 and 17.6. Noted, x/e = 10 corresponds to the centre of the rib and x/e = 10.5 corresponds to the right edge of the rib. All profiles present the results downstream of the rib, except the location x/e = 2.3. These plots show that the velocity profiles agree well with the measurements, proving that *LES* is able to capture the turbulence with good accuracy, even with the current modest meshes.

As noted, Figure 4.11(a), gives the mean streamwise velocity profiles. Some negative values can be observed at the location of x/e = 11.1 and 13.6. This results from a large recirculation region generated after the rib, which will be shown later by streamlines. Further downstream of the rib, when the flow reattaches, the streamwise velocities then become positive again. By finding the point where the velocity changes from negative to positive, the reattachment point can be located. This will be shown later in the following section in Table 4.5.

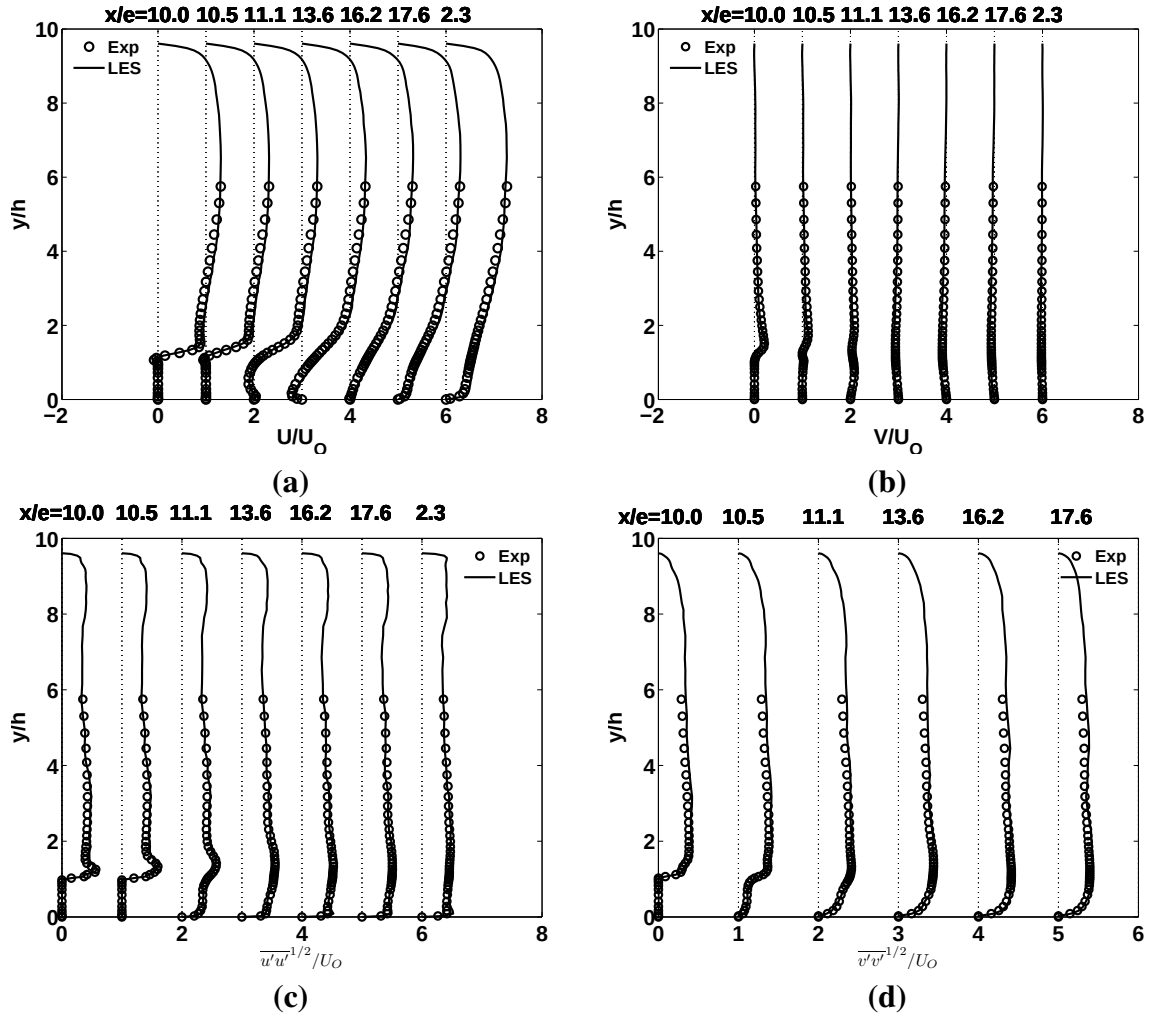

Fig. 4.11 Variation of velocity with y at seven different locations: (a) Streamwise velocity; (b) Cross-stream velocity; (c) Streamwise velocity fluctuation; (d) Cross-stream velocity fluctuation.

Figure 4.11(b) shows that the cross-stream velocity profiles are quite consistent with the experimental data. For the stream-wise velocity fluctuations, shown in Figure 4.11(c), two stress peaks appear at x/e = 10.0, 10.5 and 11.1. These can be observed in both the predictions and measurements. The peaks are a consequence of the shear layer turbulence at the top surface of the rib. The peaks then decrease with the mean flow moving downwards. Figure 4.11(d) shows that although the velocity profiles agree well in the whole computational domain, some deviation arises in predicting the cross-stream velocity fluctuation.

Figure 4.12 compares the predicted heat transfer with the measurements conducted by Acharya et al. [1]. The overall comparison of heat transfer is reasonably good (5% average deviation).

For constant heat flux, the local Nusselt number is calculated as:

$$Nu = \frac{q''}{T_s - T_b}\frac{D_h}{k} \tag{4.4}$$

Here, T_s is the wall temperatures, $T_b = \frac{\Sigma T dA}{\Sigma A}$ is the bulk temperature, and the thermal conductivity is $k = \mu c_p / P_r$.

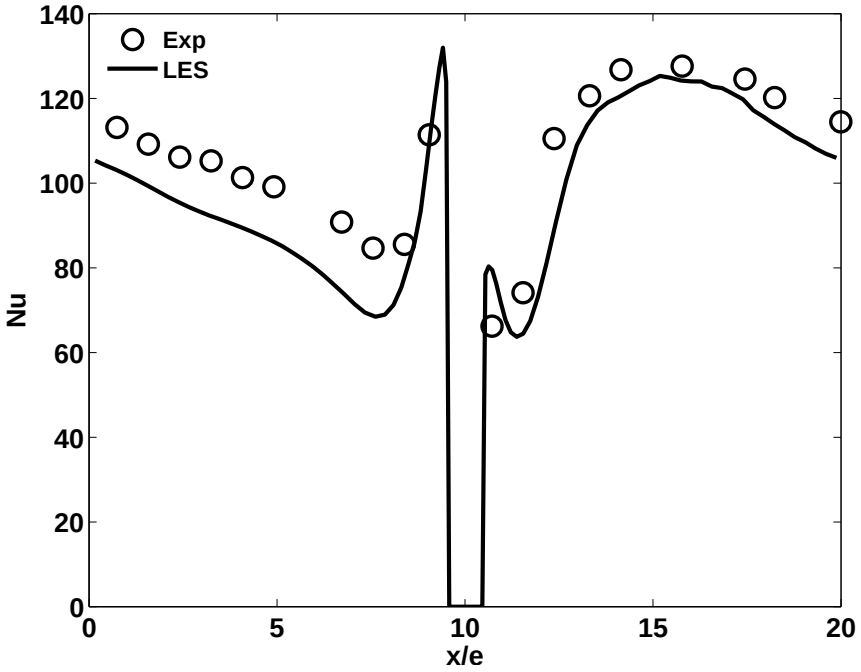

Fig. 4.12 Axial variation of Nusselt number for the baseline ribbed channel case.

The local Nusselt number is first observed to decrease upstream of the rib in the flow direction. It then comes to a maximum value at the front face of the rib. This is because at this position the instantaneous flow varies significantly in the spanwise direction. Moreover, many instantaneous backward motions are also found as shown in Figure 4.14, which indicates

active vortical motions near the wall. The presence of two peaks in both the prediction and measurements are observed in Figure 4.12, related to impingement (x/e = 9.5) and reattachment (x/e = 16), respectively. The maximum Nusselt number is found to occur in front of the rib.

4.4.2 Flow Structure

The flow structure of the square rib is first investigated to explain the mechanisms responsible for heat transfer behaviour.

Instantaneous Flow

Figure 4.13 presents the instantaneous velocity vectors with temperature contours. Upon close inspection of the velocity vectors, we can see that cold fluid is entrained toward the wall, driven by the vortices, which helps to enhance heat transfer. Here the clockwise vortices are prevalent, and the entrained cold fluid tends to move backward underneath the shear layer, indicating that there are active vortical motions near the bottom wall. This relocates the peak of the Nusselt number and can explain why the maximum value of the local heat transfer appears in front of the reattachment point.

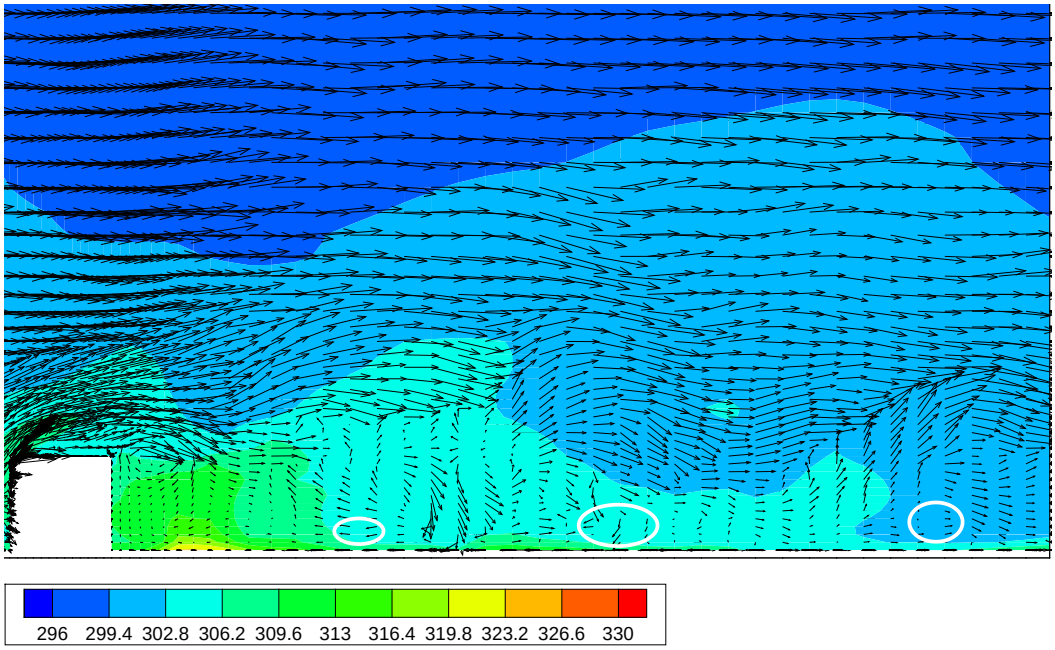

Fig. 4.13 Instantaneous velocity vectors and temperature contours in the mid x–y plane of the square rib.

Figure 4.14 shows the instantaneous streamlines. As can be seen from the instantaneous structure, the separated flow reattaches between the ribs. The zone near the rib contains the most turbulent activity. The length of the recirculation bubble changes as vortices are shed from the ribs and are convected downstream. Different eddy scales can be observed downstream of the rib.

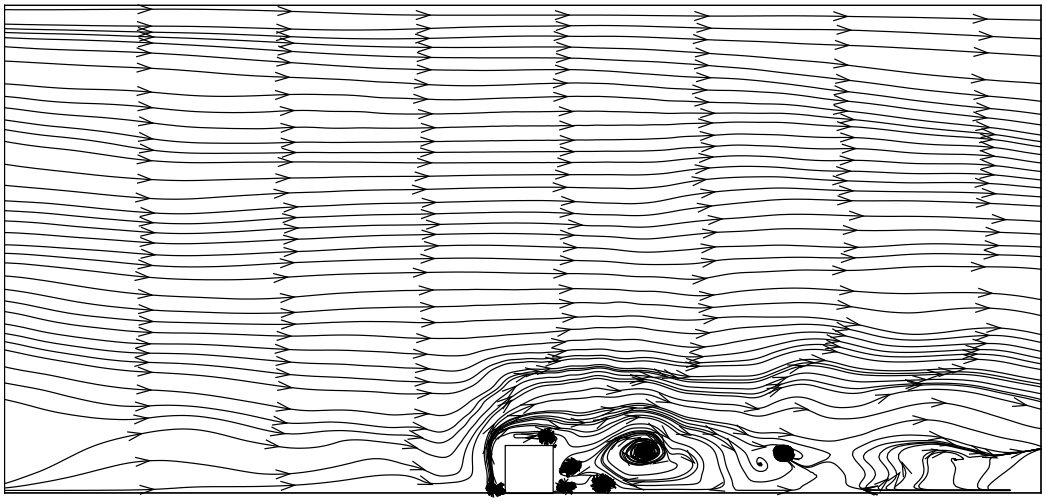

Fig. 4.14 Mid x–y plane instantaneous streamlines of the square rib.

Time-average Flow

The time-average flow field of the fully developed turbulence is further averaged spatially through the spanwise direction. The time-averaged streamlines are presented in Figure 4.15, which shows the time-averaged structures including the secondary motions, which are critical to represent flow features near the wall and to provide additional understanding of the role of these structures. Three characteristic flow features can be observed from this plot: a small recirculating region at the front face of the rib, a small primary recirculation bubble near the backward corner of the rib, and a further large recirculation region downstream of the rib. The movement of the reattachment point, L_R, destroys most classical boundary layer content and locally increases heat transfer (see later). For the square case, the reattachment length is observed to be around $5 \sim 6\ e$, which is consistent with the observation by Murata and Mochizuki [55], further indicating the accuracy of the *LES*.

Q-criterion Iso-surface

Hunt et al. [33] indicated that the rotation-dominated regions can be visualised by the iso-surface based on the Q-criterion ($Q = \frac{1}{2}(|\Omega|^2 - |S|^2)$, where Ω and S are the vorticity

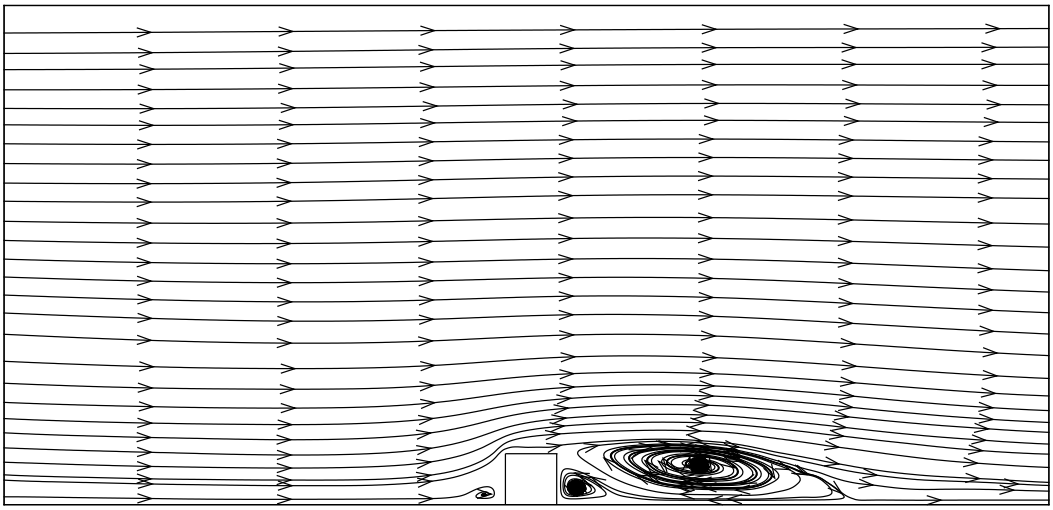

Fig. 4.15 Mid x–y plane time-averaged streamlines of the square rib.

magnitude and strain tensor, respectively). Q is a criterion used to identify the coherent structures embedded in the instantaneous field, as suggested by Dubief and Delcayre [23] and Lesieur et al. [44]. Figure 4.16 presents the iso-surface of the Q-criterion and is coloured according to local instantaneous crossstream velocity. The Q iso-surface highlights the attached recirculation structure on the top surface of the square rib as can be seen from Figure 4.14. The active recirculation tube drives the flow arriving at the rib into a swirling movement. This is caused by flow separation from the upstream face of the rib. These phenomena are consistent with previous observations in the *LES* study by Ramgadia and Saha [69]. The rib acts as a structure generator. The blockage effect of the rib, is also underlined by this Q iso-surface. Due to the separated shear layer, the presence of regions of high vorticity near the smooth wall further downstream of the rib are also shown clearly, which can be considered as instantaneous realisations of coherent structures. The recirculation structures on the top surface interact with the vortical structures further downstream and creates a high flow mixing.

4.5 Alternative Rib Geometries

In addition to the square rib, nine different geometries are also considered, as shown in Figure 4.1. To quantify the effects of rib shape on the local heat transfer features, the Nusselt number predictions are contrasted.

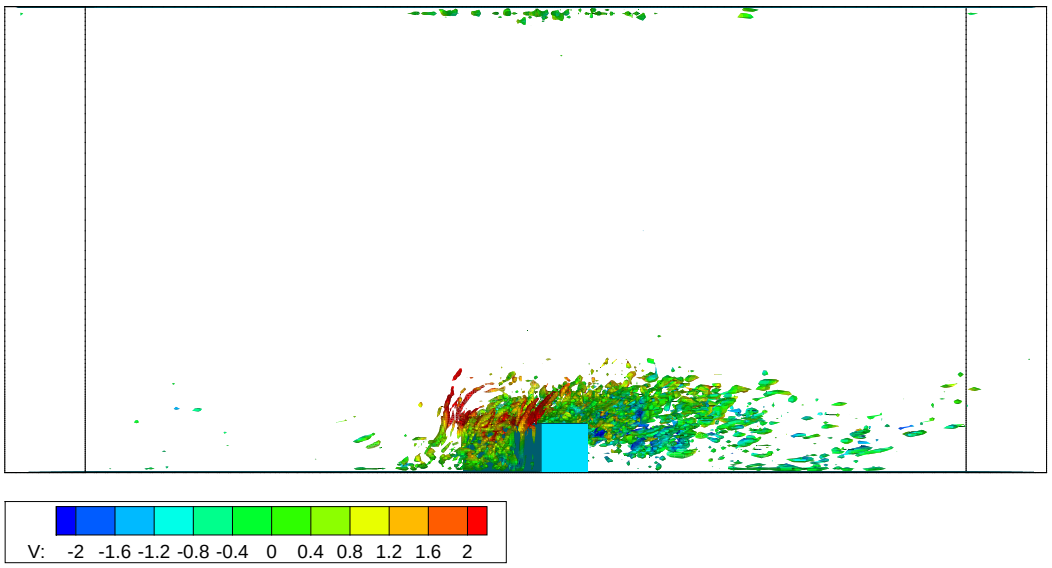

Fig. 4.16 Iso-surface of the Q-criterion coloured by v.

4.5.1 Heat Transfer

Heat Transfer Comparison

Figure 4.17 shows that all cases have similar trends. Two peaks are also visible in each profile, as examined in section 4.4.1. As in the case of the square rib, an impinging motion is also observed, for example, for the triangular case. However the location of the maximum Nusselt number differs depending on the geometry. Table 4.2 summarises the maximum value of the local heat transfer ($x/e > 10$) for each case. In Figure 4.17, upstream the rib, the triangular_up case seems to have the highest Nusselt number right at the front corner. The Nusselt number distribution is observed to be nearly identical upstream for the perforated rib and the square rib. Further downstream, in the recirculation region, the perforated rib achieves a higher heat transfer than the square rib. This maybe because the turbulence intensity of the perforated rib at that position is a little higher than the square one. The local maxima near the backward- and forward-facing corners for the semi-circle and arc rib are also not as sharp as those for the square rib. This illustrates that ribs with round shapes have a low heat transfer rate. This can be expected from the Q-criterion iso-surface.

Accordingly, comparisons of the coherent structures over the current square and semi-circular ribs are shown in Figure 4.18 to explore the influence of wall topology. The flow generated by the square rib is observed to be more complex than the semi-circular one. For the square rib, many flow structures are visible at the front corner of the rib. Downstream of the rib, at the recirculation zone, much more complex structures can also be identified.

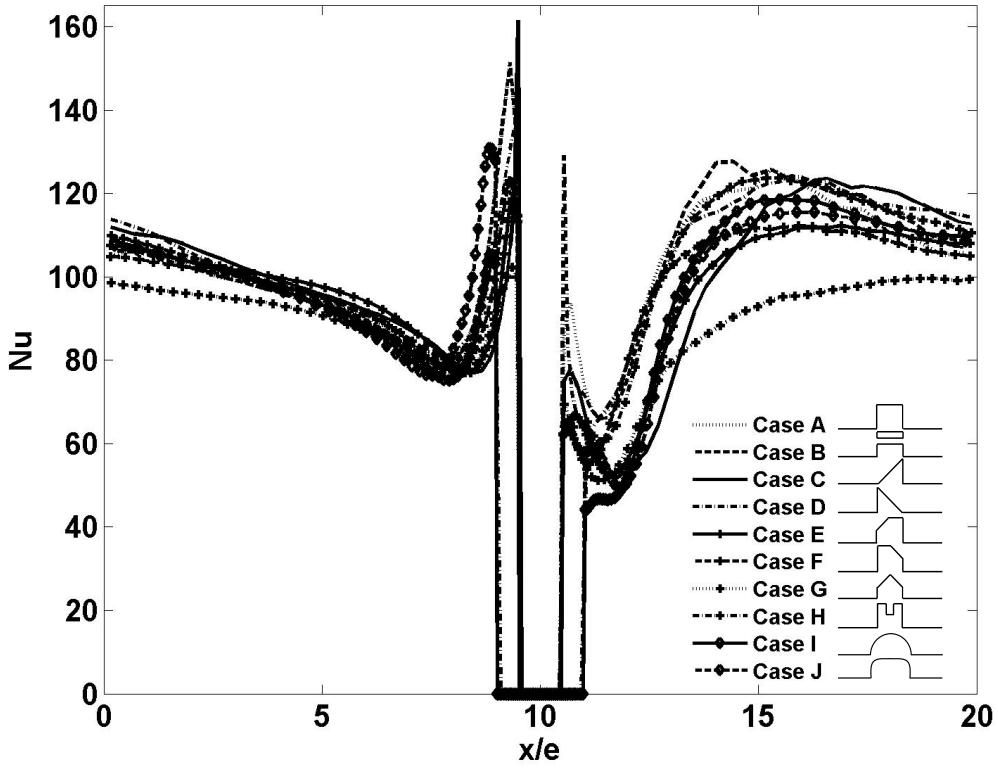

Fig. 4.17 Local Nusselt number distribution.

Table 4.2 Location of maximum N_u

Case	Nu_{max} locations
A	15.30
B	13.32
C	16.30
D	15.78
E	16.90
F	15.91
G	19.84
H	15.18
I	15.50
J	16.29

This is because both the rib faces are perpendicular to the flow direction and can produce primary and secondary recirculations near the front corner and further downstream of the rib (see Figure 4.15). However, the motion beyond the reattachment point of the semi-circular rib is found to be weak. The secondary flow can augment the heat transfer on the lower wall. Thus the Nusselt number values for the semi-circular rib are 10% lower than the square rib.

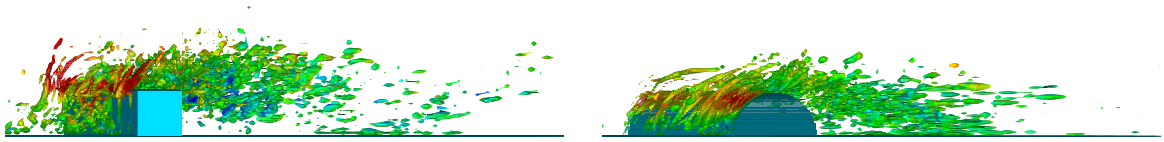

Fig. 4.18 Iso-surface contours of the square rib and semi-circular rib.

Heat Transfer Performance

The Nusselt number is normally used to measure the convective heat transfer effect. In order to better reflect heat transfer improvement of the ribbed passage, Webb et al. [123] and Han et al. [30] pointed out that the heat transfer performance can be used to evaluate the behavior of an 'enhanced' surface, which considers the heat transfer value as well as the friction factor.

The calculated Nusselt number was normalized by the Nusselt number for a smooth channel obtained from the Dittus-Boelter correlation (Nu_0):

$$Nu_0 = 0.023 Re^{0.8} Pr^{0.4} \tag{4.5}$$

The friction factor, f, is used to obtain a dimensionless representation of the pressure drop due to the ribs according to the Fanning definition:

$$f = (\frac{\triangle P}{L})(\frac{D_h}{2\rho {U_O}^2}) \tag{4.6}$$

where $\triangle P$ is the pressure drop across the length of the test section L, ρ is the density of air, U_O is mean velocity of the channel. The well-known Blasius equation is used for friction factors for a smooth duct:

$$f_0 = 0.0791 Re^{-0.25} \tag{4.7}$$

The heat transfer performance (η) of the ribbed channel can be computed with respect to both standard correlations (η_0) and smooth channel results (η_s) as provided by Gee and Webb [28]:

$$\eta_0 = \frac{Nu/Nu_0}{(f/f_0)^{1/3}} \tag{4.8}$$

$$\eta_s = \frac{Nu/Nu_s}{(f/f_s)^{1/3}} \tag{4.9}$$

where Nu_0 and f_0 stand for the correlation value of the Nusselt number and friction factor, Nu_s and f_s stand for the Nusselt number and friction factor for a smooth duct. Here, the derivation of this coefficient $1/3$ can be found in Gee and Webb [28] as the following:

Webb and Eckert [122] discuss basic heat transfer applications for internally rough surfaces. The relative heat conductance ($K/K_s \equiv hA/h_sA_s$) of the rough and smooth tube exchangers can be expressed using the ratio of Strouhal number, heat transfer surface area and mass velocity

$$\frac{K}{K_s} = \frac{St}{St_s} \cdot \frac{A}{A_s} \cdot \frac{G}{G_s} \tag{4.10}$$

The corresponding friction power ratio is

$$\frac{P}{P_s} = \frac{f}{f_s}\frac{A}{A_s}(\frac{G}{G_s})^3 \tag{4.11}$$

Eliminating G/G_s from equations (4.9) and (4.10) gives

$$\frac{K/K_s}{(P/P_s)^{1/3}(A/A_s)^{2/3}} = \frac{St/St_s}{(f/f_s)^{1/3}} \tag{4.12}$$

Thus,

$$\eta_s \equiv \frac{St/St_s}{(f/f_s)^{1/3}} \equiv \frac{Nu/Nu_s}{(f/f_s)^{1/3}} \tag{4.13}$$

The heat transfer performance, η_0, is used here to obtain the maximum heat transfer for low pressure loss. Nu_0 and f_0 are taken as the correlation value of the Nusselt number and friction factor. In Figure 4,17, although the increased performance of the triangular_up case is not obvious in the Nusselt number profiles, it becomes quite significant when the pressure drop is taken into consideration, as presented in Figure 4.19. Figure 4.19 plots the heat transfer performance. This helps explore how the investigated different rib shapes affect the local thermal performance versus pressure drop. Unlike the results in Figure 4.17, the triangular_up rib appears to have the highest overall η. Different rib shapes have been investigated in the literature using different methods (see Chapter 2). This finding is consistent with Ahn [3], who proposed that triangular-shaped rib geometry is more efficient for heat transfer than the square-shaped one.

The overall turbulence intensity ($T.I.$) for the triangular_up case is not the highest, nevertheless the value of $T.I.$ in the recirculation region is 5.05%, which is almost as high as the square case. Additionally, the turbulent fluctuating components, which are closely related to heat transfer mechanisms, reach a higher maximum value in the triangular_up case which has a sharp geometrical feature. The main parameters of the heat transfer results are compared in Table 4.3. These parameters are the Nusselt number and the heat transfer performance averaged in the streamwise and spanwise directions, maximum Nusselt number, and maximum heat transfer performance.

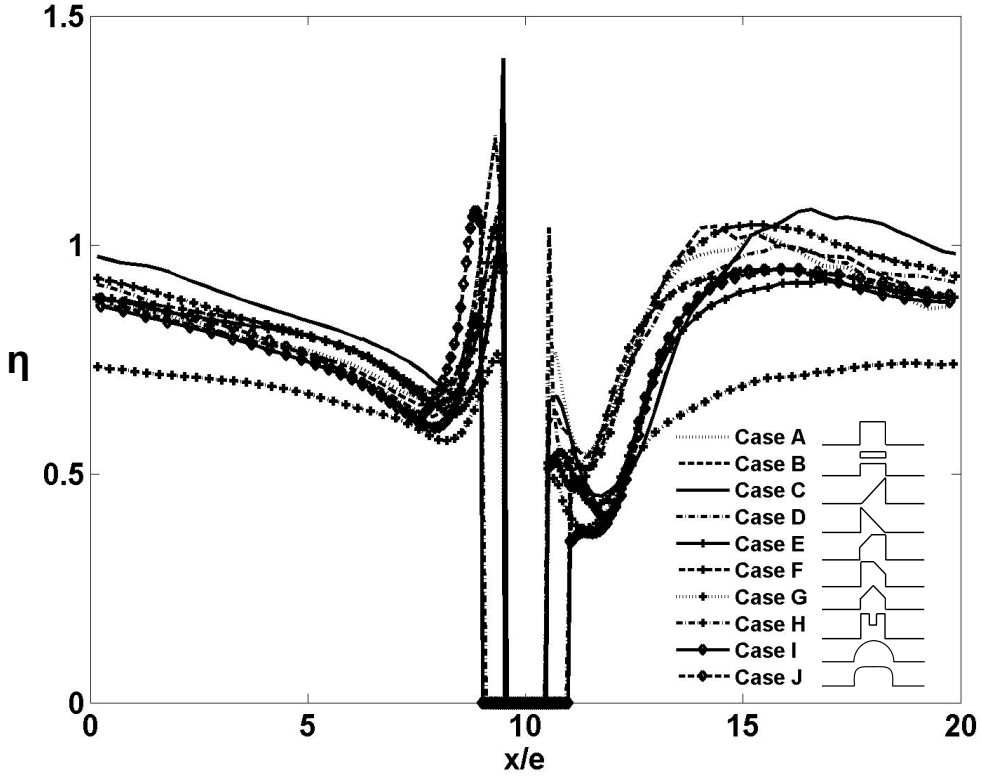

Fig. 4.19 Local heat transfer performance distributions.

Observation of Figure 4.19 shows that the heat transfer performance of the triangular_up case increases fairly rapidly near the front surface of the rib. It then comes to a local maximum value just before the front corner of the rib, and decreases subsequently along the rear face. Close inspection of the figure shows that the substantially low values of local performance behind the concave corner for the triangular_up rib are much more likely to occur than those behind the other rib geometries. As shown in Table 4.3, the triangular_up rib provides the best overall performance with a value of $\overline{\eta} = 0.85$, this being 5% higher than the basic square rib. The increase in performance would allow, for example, less fluid to be bled from the compressor in an aeroengine, increasing overall efficiency, or improving durability.

Table 4.3 Comparison of main heat transfer parameters

Case	$\overline{N_u}$	$N_{u_{max}}$	$\overline{\eta}$	η_{max}
A	91.41	139.99	0.81	1.33
B	91.75	139.87	0.81	1.33
C	94.50	149.23	0.85	1.41
D	94.54	125.38	0.81	1.16
E	84.92	106.55	0.78	1.01
F	88.70	113.69	0.81	1.08
G	65.58	77.90	0.60	0.75
H	87.80	114.28	0.80	1.09
I	82.47	103.53	0.75	0.99
J	84.88	117.49	0.77	1.12

4.5.2 Flow Structure

Figure 4.20 shows the instantaneous streamlines for the ten cases considered here. The eddy scales downstream of the rib change with the rib geometry.

To better appreciate the flow physics, the axial spatial correlation coefficients are calculated and shown in Figure 4.21. The two-point correlation coefficient is expressed as:

$$R_{11} = \frac{\overline{u_1'(x)u_1'(x+\triangle x)}}{\overline{u_1'^2}} \tag{4.14}$$

where the symbol $\overline{u_1'(x)u_1'(x+\triangle x)}$ indicates the corresponding mean value.

The correlation coefficients are obtained between $0 \sim 5e$ in the x-direction and at $y = 0.8e$, where large scale eddies are observed in Figure 4.20. The correlations are centered about a point at $x = 2e$. The correlations points are then moved axially with steps of $0.5e$ along the $x+$ and $x-$ directions.

The correlation coefficients correspond to the existence of streamwise vortical structures downstream of the ribs. The correlations in Figure 4.21 look quite different. The distance to $R = 0$ gives the eddy integral scale. The integral length scales of these different rib geometries are summarised in Table 4.4. It shows that the triangular_up case has the largest integral length scale. Also, it has the highest turbulence intensity at that area (6.05%), where the most active interaction takes place between the recirculating fluid flow over the ribs in the channel.

Figure 4.22 compares the time-averaged streamlines. Three characteristic flow features observed for the square rib can also be seen in these plots. For the square and perforated rib, a separation bubble appears at the top surface, with the opposite direction to the main

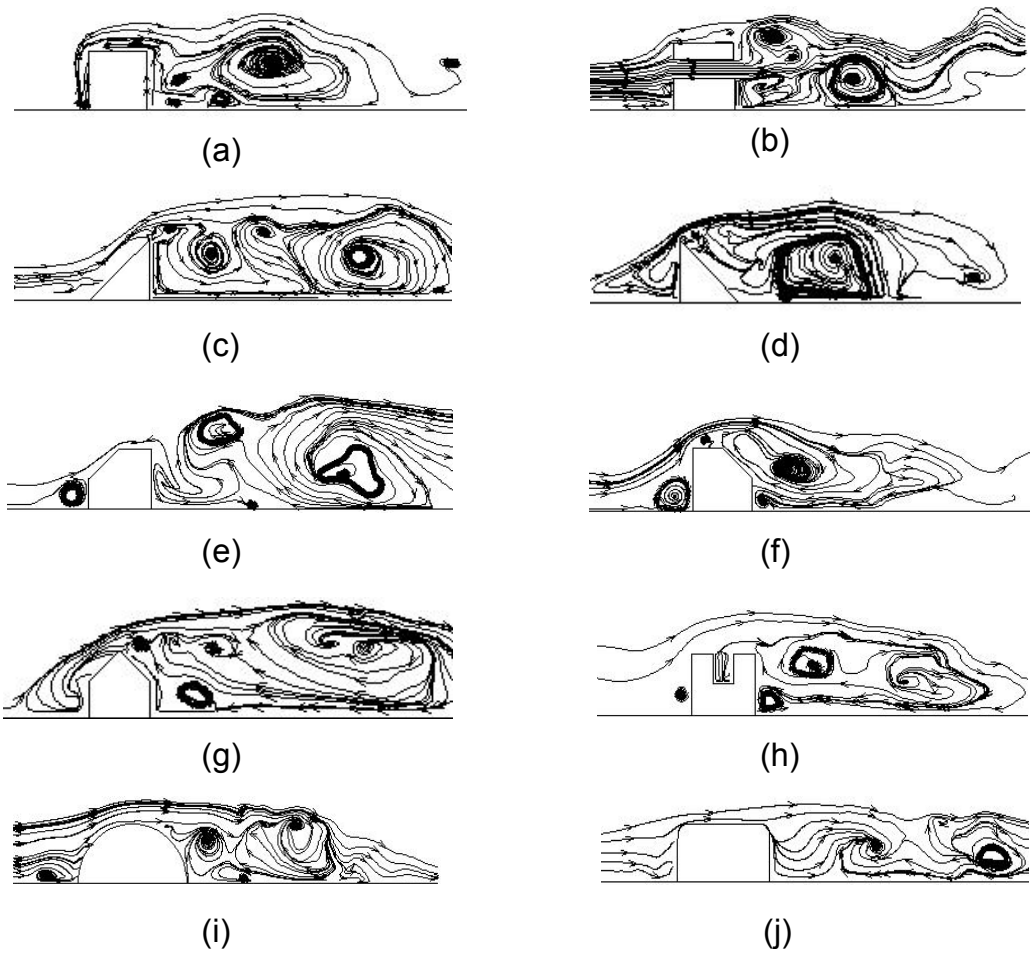

Fig. 4.20 Instantaneous streamlines: (a) Square rib; (b) Perforated rib; (c) Triangular_up rib; (d) Triangular_down rib; (e) Pentagonal_up rib; (f) Pentagonal_down rib; (g) House-shaped rib; (h) Groove-shaped rib; (i) Semi-circular rib; (j) Arc rib.

Table 4.4 Integral length scale

Case	l_I
A	2.85
B	1.83
C	4.34
D	3.44
E	3.39
F	3.64
G	2.94
H	3.88
I	2.59
J	2.42

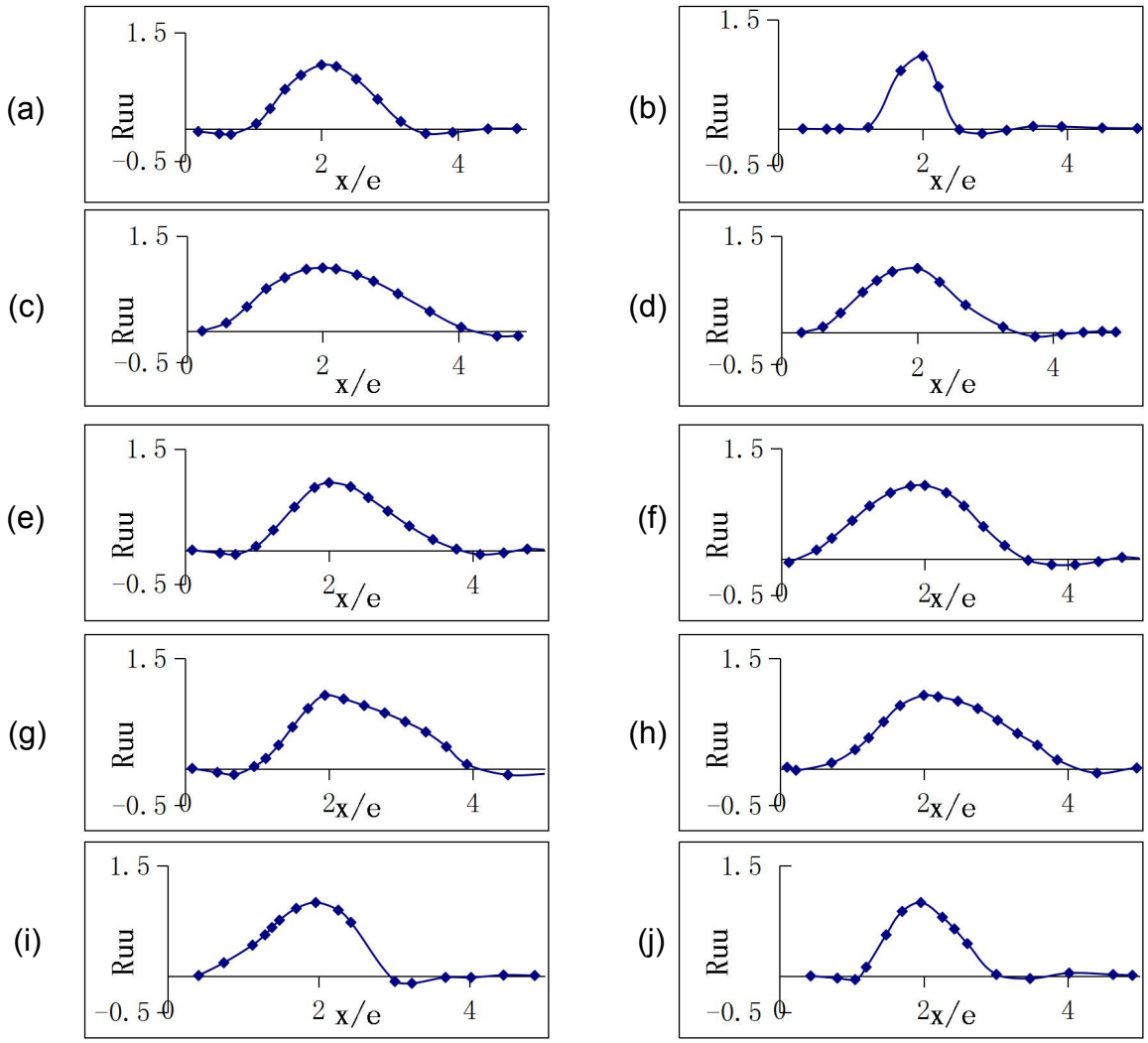

Fig. 4.21 Two-point correlation coefficients: (a) Square rib; (b) Perforated rib; (c) Triangular_up rib; (d) Triangular_down rib; (e) Pentagonal_up rib; (f) Pentagonal_down rib; (g) House-shaped rib; (h) Groove-shaped rib; (i) Semi-circular rib; (j) Arc rib.

recirculation zone, as shown in Figures 4.22(*a*) and 4.22(*b*). This is because the sharp front edge of the rib deflects the upstream flow.

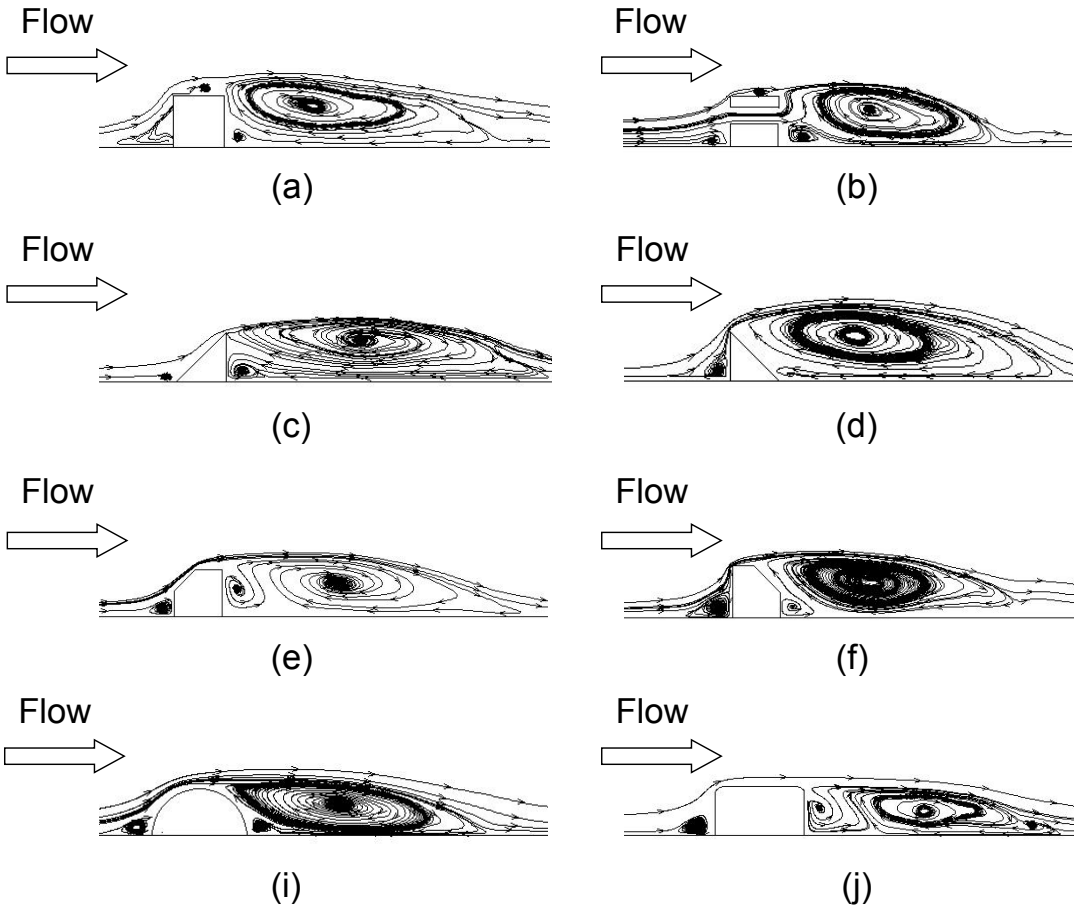

Fig. 4.22 Time-averaged streamlines: (a) Square rib; (b) Perforated rib; (c) Triangular_up rib; (d) Triangular_down rib; (e) Pentagonal_up rib; (f) Pentagonal_down rib; (i) Semi-circular rib; (j) Arc rib.

The non-dimensional reattachment length is summarised in Table 4.5. The Nusselt number distribution is observed to be nearly identical upstream for the perforated rib and the square rib. This fact is probably the reason why these two cases have similar flow characteristics. However, the Nusselt number near the back corner of the perforated rib is not as large as the square rib. This is because the recirculation bubbles are much smaller for the perforated rib (see Figures 4.22(*a*) and 4.22(*b*)). The reattachment length for the perforated rib is reduced by 15% compared to the solid square rib. This is because the flow passing through the slit of the rib adds streamwise momentum to the recirculation bubble region and generates vortical flow structures. The heat transfer behaviour of the semi-circular rib and

arc rib can also be expected from the much smaller and weaker recirculation bubbles of these two cases, as shown in Figures 4.22(i) and 4.22(j). The size of the recirculation zone for the triangular rib with increasing height in the flow direction is obviously larger than that of the other cases. This arose from the upward flow due to the front inclined surface of the triangular-shaped rib. Case E also showed large separation bubbles due to the inclined front walls.

Table 4.5 Non-dimension reattachment length

Case	L_R
A	5.78
B	4.95
C	7.29
D	5.86
E	6.31
F	4.92
I	5.51
J	5.15

4.6 Conclusions

Numerical studies of a fully developed channel with ribs have been performed using *LES*. *IBM* is implemented with *LES* to save the effort of grid generation and enhance speed of *CFD* solution allowing the rapid exploration of different rib geometries. Three benchmark cases using an *IBM* have been validated: (i) the flow in a plane channel skewed to the computational grid lines, (ii) wall-driven flow in an inclined box, (iii) the flow around a circular cylinder in a channel. Agreements are found when comparing the numerical results with the analytical and experimental data.

The thermal characteristics in terms of heat transfer and friction factor of ten different rib shapes have been investigated: square, perforated, triangular with increasing height in the flow direction, triangular with decreasing height in the flow direction, pentagonal with increasing height in the flow direction, pentagonal with decreasing height in the flow direction, house-shaped, groove-shaped, semi-circular and an arc profile. The square case was first carried out to validate the accuracy of the *LES* model. Through the velocity field and heat transfer results, *LES* was found to be able to predict the velocity distribution with good accuracy and obtain the correct Nusselt number trend. It shows that the structural solver can not only generate the mesh efficiently, but can also help to model the turbulence accurately.

The formation of a large recirculation bubble has been observed for all cases downstream of the rib. Moreover, to better appreciate the flow physics, the two-point correlation coefficients were also calculated. The triangular rib with increasing height in the flow direction, with the largest recirculation bubble, was found to provide the best heat transfer performance, at 5% more than the basic square rib. The results also showed that rounded-corners deteriorated the heat transfer performance.

Chapter 5

Optimisation of Labyrinth Seal

5.1 Introduction

As mentioned in Chapter 1, labyrinth seals are vital components in turbomachinery. They are used to mitigate the leakage flows around blades and therefore to increase the turbine efficiency. They have been explored extensively experimentally, and different sizes and types of labyrinth seal, such as straight-through seals, inclined seals, and honeycomb seals have been investigated in the literature (see Chapter 2). Despite this, however, they remain a difficult geometry to design effectively, as experimental methods can be prohibitively expensive under real engine conditions, particularly when large numbers of different designs need to be tried.

Computational modelling of the fluid physics has been shown to be tremendously powerful in these situations, however the traditional workhorse computational methods – solution of the Reynolds Averaged Navier-Stokes equations – tend to perform inadequately on such separated and unsteady flows. Fortunately, these flow characteristics lend themselves well to solution using Large Eddy Simulation.

5.2 Introduction to Optimisation

Some kind of "optimisation" is almost universal in design processes. Traditionally, this has taken the form of the engineer producing an initial design, and then manually varying it slightly to improve the performance. This approach has two key drawbacks – it requires substantial user involvement, and it may miss large portions of the design space. The other extreme of optimisation involves exhaustively searching the entire design space. Although

this is, conceptually, a straightforward process to automate, and no part of the design space is missed, for more than trivial problems it is likely to be impossibly expensive.

Between these two extremes lie a range of self-guiding optimisation heuristics, which aim to sensibly and automatically explore the design space while avoiding the extreme cost of an exhaustive search. Coupled with computational physics approaches, these can be very effective tools for largely automated design optimisation. With the increase in computational power that is available, these self guiding optimisation heuristics have been used widely, and automated optimisation is realisable.

5.2.1 Optimisation Algorithm Heuristics

To help understand the optimisation process, a multidimensional design space is first introduced. Every value from the objective function is found in this design space, indicating how effectively each input parameter may help to improve the target design. Thus the purpose of the entire optimisation process is to find the deepest trough or highest peak within the corresponding design space, leading to the optimal design. A variety of guiding heuristics are available to be used for this purpose. It is essential to select the appropriate optimisation algorithm as it will directly affect the optimisation performance. Some of the most commonly used intelligent optimisation algorithms are:

Hill Climbing

The hill climbing algorithm is probably the simplest of the optimisation heuristics. Hill climbing is an iterative algorithm in which a starting point is randomly chosen within the design space. It then attempts to find a better solution by comparing the current objective function value with the surrounding nodes, and moves the design in the direction which produces an improvement. By repeatedly doing this until no more improvement is possible, an optimised design is found. The solution this "climbs the hill" towards the optimum, as seen in Figure 5.1.

Hill climbing is an efficient way of finding a solution, however, in more complicated design spaces with many peaks and troughs, it is easy for it to get trapped in a local optimum, with the solution dependent on where the starting design was located. In fact, in the case shown in Figure 5.1, the solution has become trapped in a local optimum, missing the much larger peak behind.

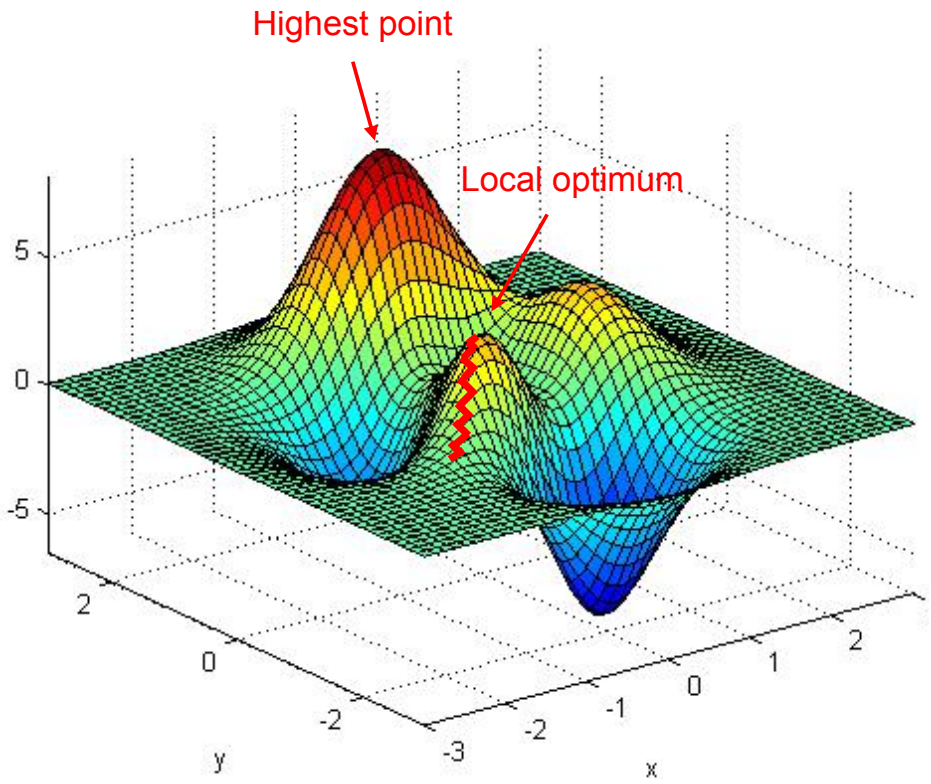

Fig. 5.1 Hill climbing algorithm in a three-dimensional design space.

Simulated Annealing

The simulated annealing (*SA*) algorithm was developed by analogy with the thermodynamics of metalwork, which is a technique involving heating and controlled cooling of a material to increase the size of its crystals and reduce their defects. In simulated annealing, a temperature-like variable is used to simulate this heating and cooling process. When the cooling is sufficiently slow, the global minimum will be reached. In *SA* algorithm, protections are provided against becoming trapped in a local rather than globally optimal design.

Genetic Algorithms

Genetic algorithms are inspired by Darwin's evolutionary theory, and were first proposed by Professor Holland from Michigan University in 1975, and were further developed by Back et al. [6]. Through the biological process of evolution, it enables gradual convergence towards the best possible solution for an optimisation problem by employing natural selection. GAs can search with robustness, have a global optimisation ability, and are not limited by derivatives and the associated problem. With a proper setting of constraints, they are able to rapidly explore a large design space whilst also rapidly rejecting suboptimal parameters

sets. As each solution can be evaluated separately, it lends itself to parallel architectures. The large data sets generated can also be used to inform design practices, lower order modelling and provide a deeper understanding of factors impacting complex flow physics. Based on the above advantages the genetic algorithm is used here.

5.3 Optimising with a Genetic Algorithms

For the cases laid out here, a custom procedure was developed to link the main *CFD* code (including the *IBM*) with the genetic algorithm. Figure 5.2 shows a flow chart of this process to give an overview of the coupling between the codes. This can be considered as consisting of four basic stages.

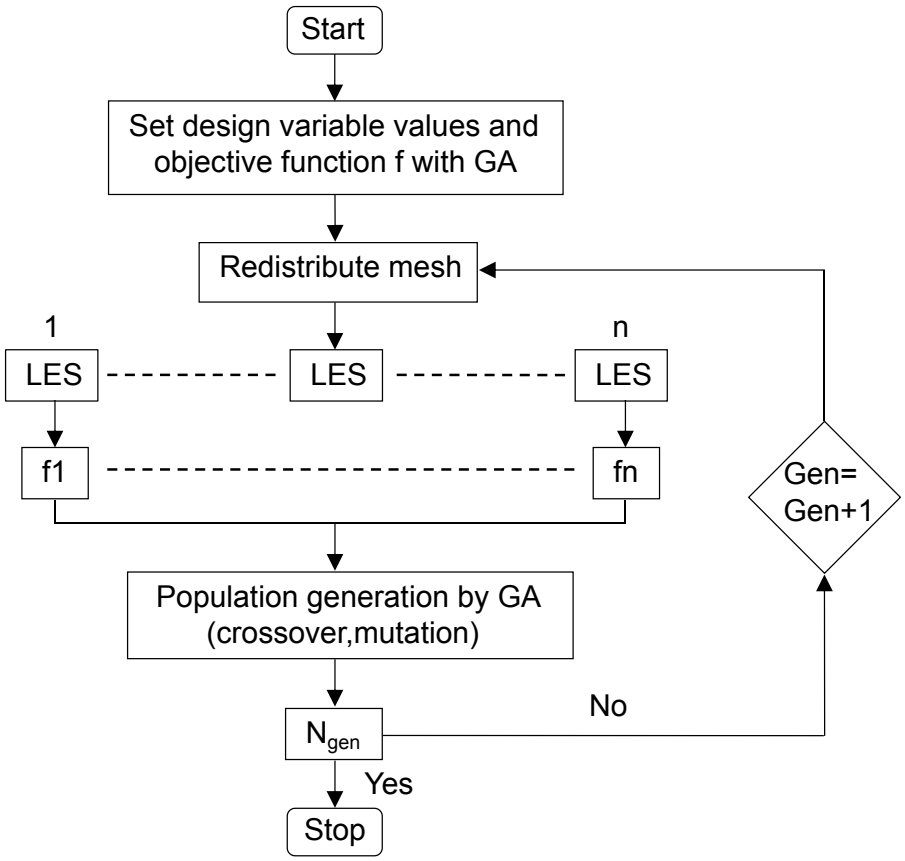

Fig. 5.2 A flowchart of the mechanism of *GA*.

1. Prior Set Up.

Before the optimisation begins, the design space is encoded as a stream of data, referred to in the literature as a genome. To determine the extent of the design space, a systematic

study of the key dependent variables was conducted. Each member of the initial set of designs is stochastically generated by giving a random value to each gene within its genome. One of the key advantages of the *GA* is that it is able to handle large populations, so in this case the initial generation consisted of 100 members. Typical members of this initial population are shown in Figure 5.3. Subsequent generations consisted of 30 members.

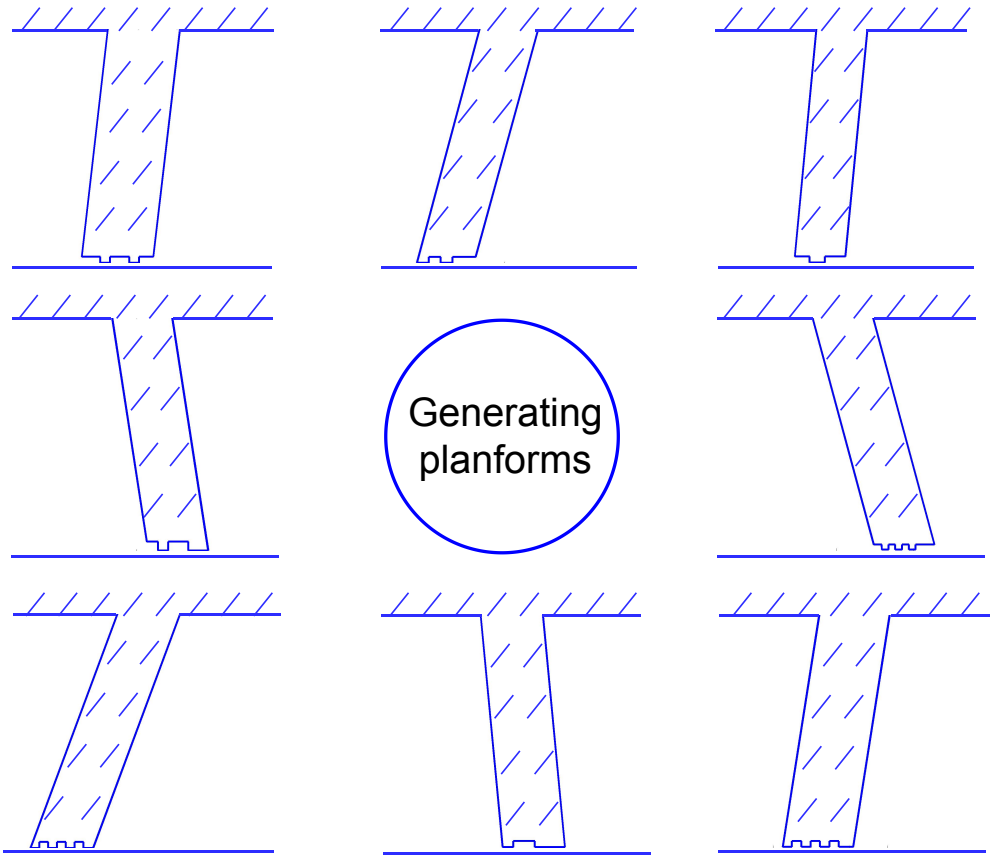

Fig. 5.3 Typical forms of initial layouts for the population.

2. Determination of the Fitness Parameters.

The fitness parameter describes how well a design performs. Designs which have better fitness parameters are more likely to pass on their genes to the next generation of designs. In this case, the fitness parameters were determined by performing a Large Eddy Simulation on each design. Each design was then ranked by its fitness. In terms of the design space, the individuals with the best performance tend to belong to the regions where the objective function is more likely to achieve high values.

3. Selection, Crossover, and Mutation.

In genetic algorithms, genomes are sets of parameters which are specific to the problem to be solved. In the current implementation these genomes are generated by breaking down the design variables into integer strings. The set of all genomes is known as the population. The key part of the genetic algorithm is the manner in which the genomes of the next generation are determined from those of the previous. The first stage in this process is selection. The best performing members of the population are chosen to be parents based on their objective functions. Several methods, such as that of Mitchell [53], exist to choose these parents allowing the best performing designs to produce more children. Once the parents have been selected and paired, their genes are recombined in a process known as crossover to produce offspring. For each parent's gene, the genotype had a 50% chance to pass on to the child's genome, as shown in Figure 5.4.

To allow further exploration of the design space, mutations of the child's genome could also happen. A complete mutation, where a gene was completely lost and replaced at random happened in 0.1% of cases. A swap, in which the genotypes of two neighbouring genes were swapped in the genome happened in 0.5% of cases.

Fig. 5.4 Portfolio optimisation.

4. Termination Condition and Output.

After each generation, the simulation is tested for whether it meets the termination conditions, either a sufficient improvement level in the objective function, or a certain amount of elapsed time, or a fixed number of generations. In this case, the number of generations was fixed at eight. Once this criterion has been met, the optimal design is output.

Unlike in either the hill climbing algorithm or simulated annealing, each of the individuals generated by the *GA* can be evaluated completely separately from each other. In this situation the whole process can be conducted in a perfectly parallel fashion. Figure 5.5 shows how this could be run on various different computational architectures without a loss of speed. The evaluation of each generation of thirty individuals took, in total, about 120,000 core hours. However, in this work only 24 cores were used for each individual seal simulation. By making use of the inherent parallelism of the heuristic, the real time for each generation was reduced to less than ten days.

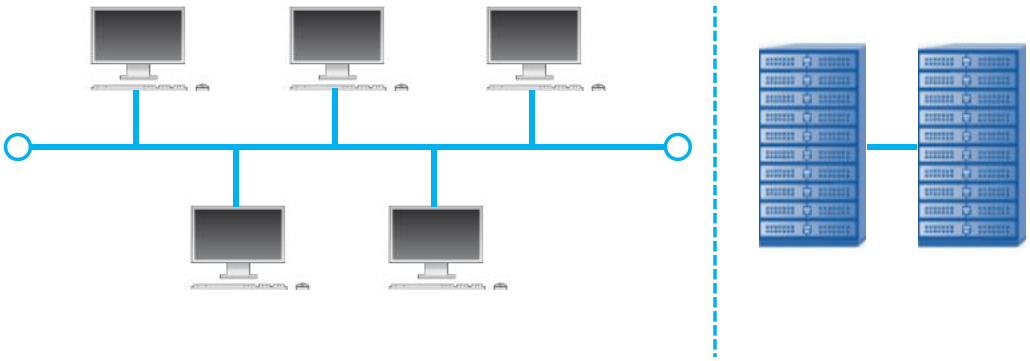

Fig. 5.5 Distributed sources of computing power compared to supercomputer sources of computing power.

5.4 Computational Setup

This optimisation study starts with a simple geometry, frame (a) as shown in Figure 5.6, studied by Gamal and Vance [27]. The baseline seal has previously been studied using a variety of *LES* models in Tyacke et al. [111]. For the *LES* models tested, the mass flow coefficient, f, is calculated, as given in Gamal and Vance [27], as

$$f = \frac{\dot{m}\sqrt{RT_{in}}}{A_i P_{in}} \tag{5.1}$$

where $\dot{m}$ is the mass flow rate through the seal, P_{in} is the inlet pressure, and A_i is the clearance area.

The results for the baseline seal matches the measurements at a pressure ratio of 2.04 within approximately 1%. Hence, *LES* has been shown to be a reliable method to study these types of flows.

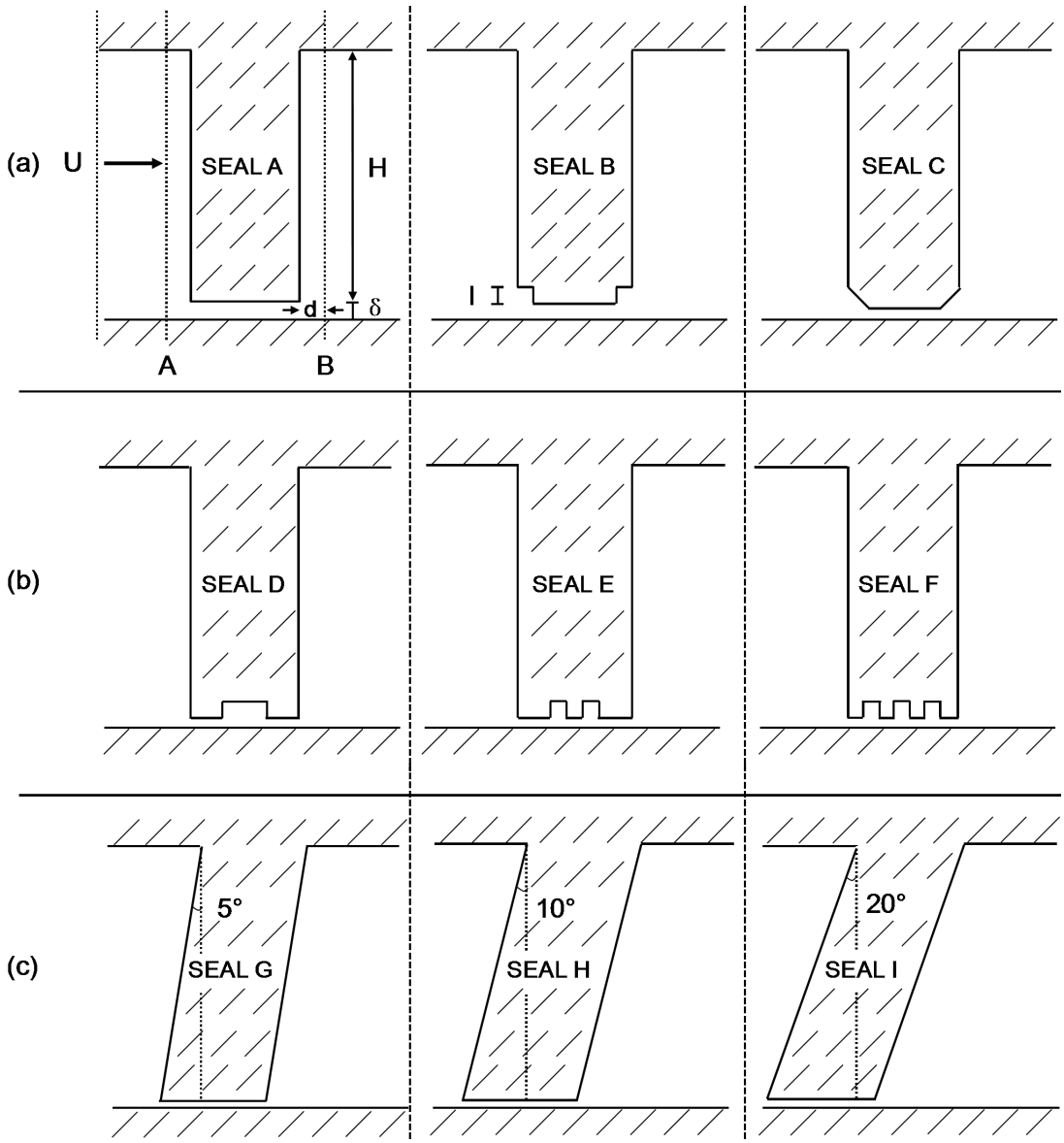

Fig. 5.6 Schematic diagrams of some different seal configurations.

5.4.1 Geometry of the Labyrinth Seal

Some key cases, that are shown in Figure 5.6, have been run to investigate the effect of various geometrical parameters. These geometries contain different inclination angles (θ), numbers of grooves (n), groove widths (l), groove geometries and corresponding positions.

The width of the groove was determined based on the tooth width (L) and number of grooves (n). For the baseline seal, the clearance size δ is set as $\delta/H \approx 0.008$. Here, the distance between profile B and the tooth boundary is $d/L = 0.35$, as shown in Figure 5.6. This location will be used to extract velocity and Reynolds stress profiles in the results section. The width of the groove, l, was determined based on the tooth width and number of grooves. For Seal B, the grooves were located at the start and end of the tooth and the groove width was set as $1/12L$. For Seal E the grooves were located at two positions along the tooth, the corresponding l was set as $1/6L$; for Seal F the teeth were located fully along the groove with e set as $1/10L$.

5.4.2 Mesh, Resolution and Runtime

The baseline mesh is $359 \times 399 \times 42$ nodes in the x, y and z directions. These correspond to an average grid spacing of $\Delta x^+ = 12$, $\Delta y^+ \approx 1$, $\Delta z^+ = 25$ in the seal tooth region. In the cavity zone, where the shear is less intense, the average grid spacing is $\Delta x^+ = 5$, $\Delta y^+ = 15$, $\Delta z^+ = 12$. At walls, $\Delta^+_{normal} \approx 1$. These spacings are within *LES*–Quasi–*DNS* resolution requirements, and the total mesh size is around 6 million. Figure 5.7 shows the structured mesh of the computational domain in this study with every 8th line plotted. In the x- and y- directions, more cells are applied around the seal blade and in the near wall region to capture the turbulent shear layer and small scales near the wall. The CFL, which is defined as $u\Delta t/\Delta x$, is set to $CFL \approx 1$. For the seals with an inclination angle, the mesh has been refined in the x direction and contains $512 \times 399 \times 42$ nodes in the x, y and z directions, and the total mesh size is around 8.6 million. Periodic boundary conditions were employed in both the streamwise and spanwise directions, and the no-slip condition is applied at walls.

The optimisation simulations are made at a constant pressure ratio. A key time scale is the time taken for the development of the correct mass flow rate from the initial conditions. This can be inferred from Figure 5.8. Here $t^* = L_{gap}/U_{max}$ represents one through flow time for the gap. The flow is developed by $15t*$, and then statistics are averaged for at least another $15t^*$. Around 220 hours using 24 CPU cores are required for each $15t^*$. The runtime could be reduced on more modern clusters, for example using Intel Xeon 2.2 GHz a $CPUs$ factor of 4x reduction was achieved.

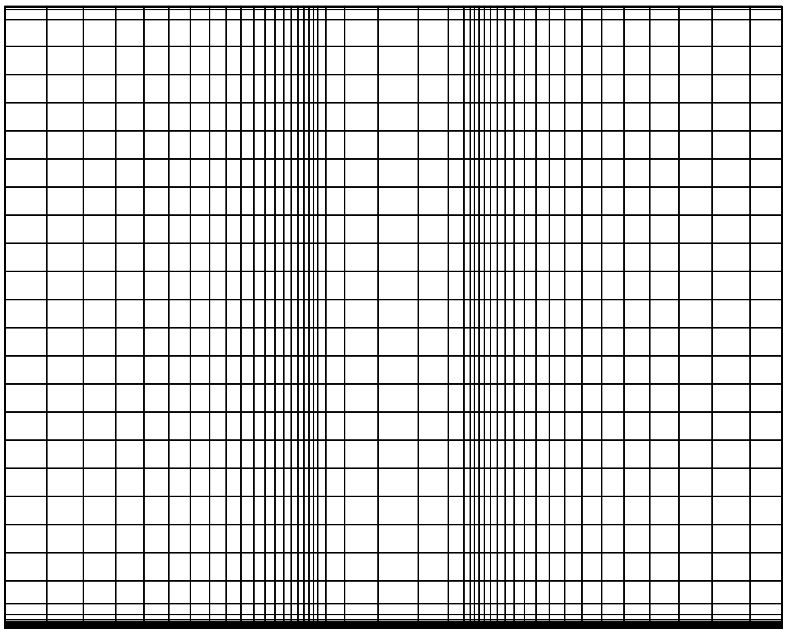

Fig. 5.7 Mesh for the baseline Seal *A* (only every 8^{th} grid line plotted).

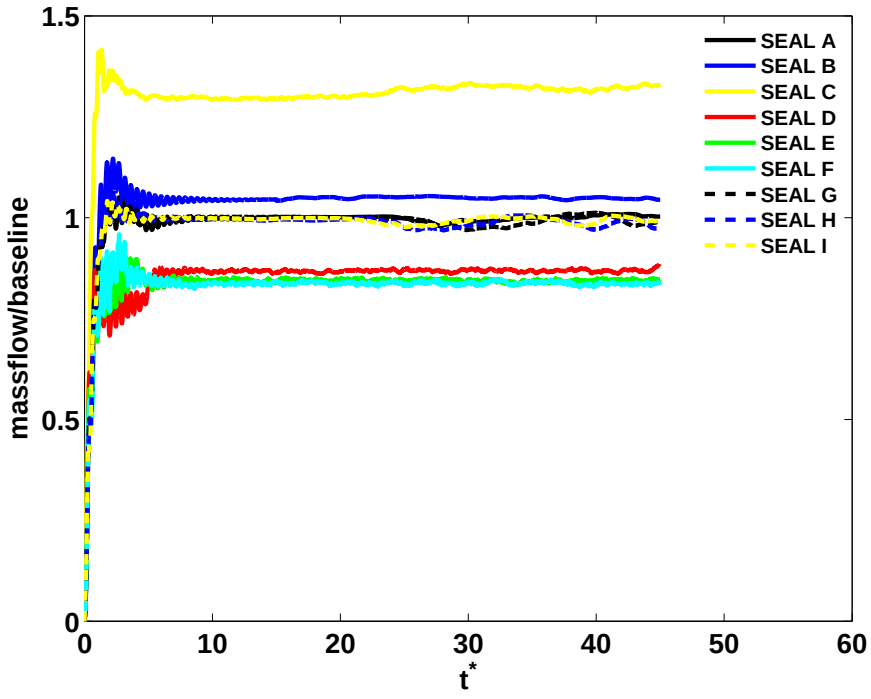

Fig. 5.8 Typical time scale of multiple configurations vs. mass flow coefficient.

5.5 Parametrisation and Objective Function

5.5.1 Mass Flow Results

Initially, the mass flow results for nine example seals were analysed, to investigate the effect of various parameters on the seal performance. The mass flow coefficient, f, was selected as the objective function. Figure 5.9 compares the pressure ratio against the mass flow coefficient for these nine example seals, at pressure ratios of 1.5, 1.75, and 2.04. For all cases, the mass flow increases almost linearly as the pressure ratio increases. The calculated results also show a strong dependence of the objective function on the seal configuration.

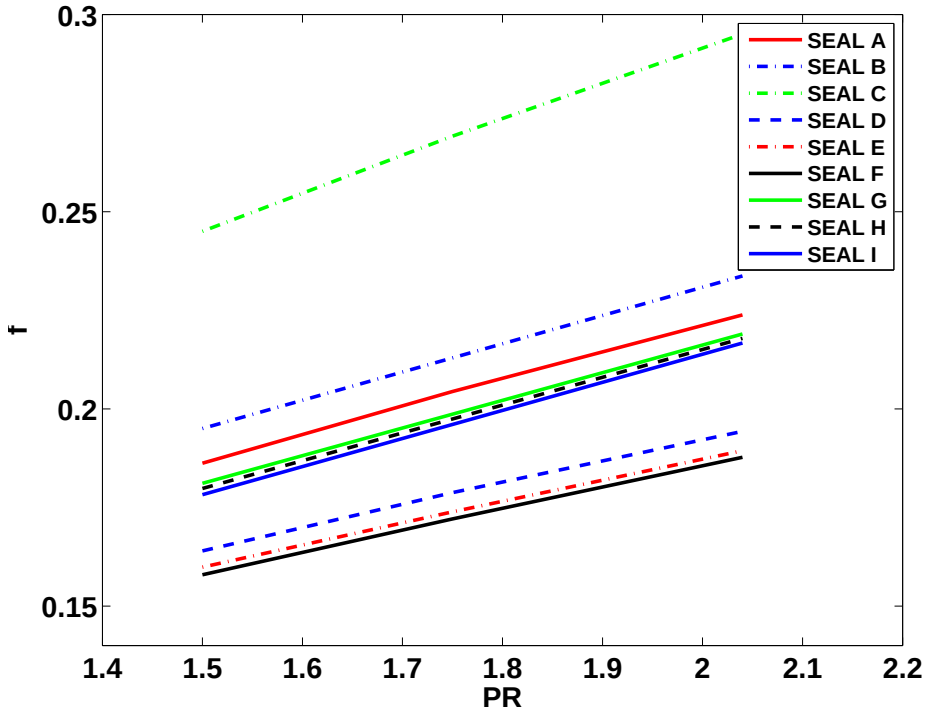

Fig. 5.9 Effect of labyrinth seal configuration on the mass flow coefficient vs. pressure ratio.

As can be seen from Figure 5.9, the mass flow coefficient of the seals with grooves is much smaller than that of the baseline, Seal *A*, suggesting that the leakage performance of the grooved seals are better. It is also noted that the more grooves, the better the leakage performance that can be achieved. The leakage mass flow coefficient of Seal *F* reduced by 16% compared to that of the baseline Seal *A* for a given pressure ratio. While seals *D* to *F* have better leakage performance, seals *B* and *C* fail to show a positive effect, with Seal *C* performing particularly poorly.

In order to highlight the difference in vortex patterns that different seal layouts can produce, Figure 5.10 presents the instantaneous vorticity magnitude contours for each of

the example seals. The flow fields shown in Figure 5.10 for seals with grooves (D to F) are similar. For these geometries, the flow through the gap enters the grooves, which causes higher loss and a large flow blockage area. This complicated flow structure caused by the grooves results in a larger pressure drop. For a given pressure ratio, then, there is less leakage for the seals with grooves. For Seal F, with grooves, the main flow separates into three recirculating regions. In Seal E, two vortices rather than three were formed. As a result, the vorticity for Seal F is more intense. Consequently, it shows the best performance in reducing the leakage.

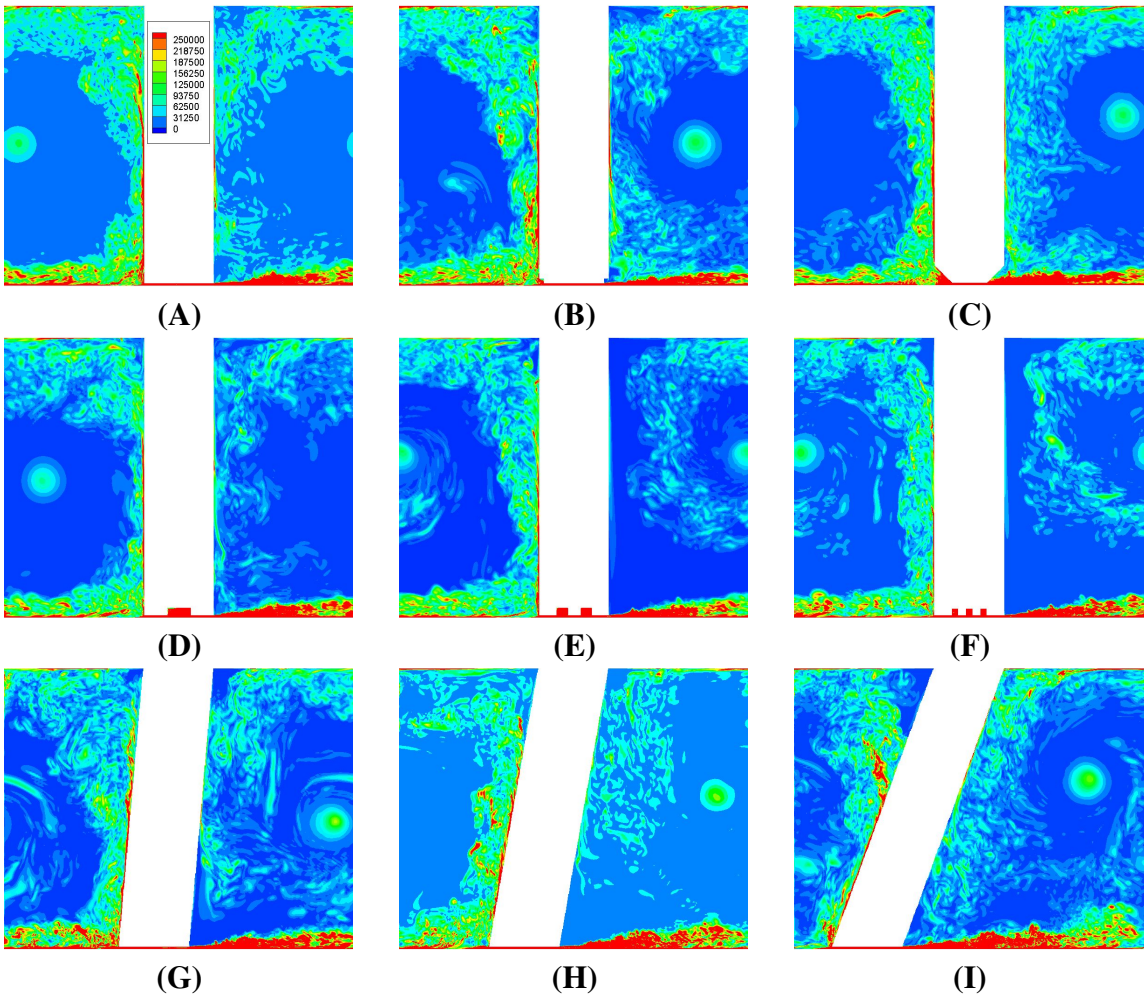

Fig. 5.10 Instantaneous vorticity magnitude contours of seal configurations.

Fasheh [24] stated that an inclination angle would lead to lower leakage rates than a straight tooth profile. This finding is supported by the results of this study, as the straight seal is again found to have greater leakage than the upstream inclined seals. The leakage

performance between the three inclined seals is quite similar, though as the inclination angle increases, there is slightly improved performance. Seal *I* (with the greatest inclination angle in the upstream direction) reduced the leakage by 3.2% relative to the baseline straight seal (Seal *A*) at a pressure ratio of $PR = 2.04$. As shown in Figure 5.10, Seal *I* produced a more distinct deflection of the leakage flow. After the fluid has flowed through the first tooth, deviation of fluid from the mean axial flow direction is greater. This leads to increased recirculation strength and kinetic energy dissipation in the main cavity.

5.5.2 Effects of Rotational Speed

Waschka et al. [119] found that at low speeds the impact of rotation on sealing performance could be considered negligible. This is further explored here, invoking the assumption that the rotor radius $\gg 20\delta$, so that the Cartesian coordinate system is maintained. Figure 5.11 compares the mass flow results based on different rotational Reynolds number. Here, the rotational Reynolds number is defined as $Re_r = \rho v_r R_r / \mu$, where v_r represents the rotational speed, and R_r represents the rotor radius.

The rotor surface is set to be the rotating wall boundary. Simulations were conducted with the rotational speeds in the range of 0–4000 rpm with a constant sealing clearance, where the typical rotational speed for jet engine is around 11,000 rpm. From the results, as shown in Figure 5.11, the leakage flow rate remains approximately constant. Thus to keep the number of simulations – and mesh requirements – manageable, the effect of rotational speed is not considered in this optimisation exercise. However, Lu et al. [51] shows that the rotational speed and its physical impact is aligned with that of clearance. Hence, variations in clearance are, in a sense, a surrogate for rotational speed.

5.5.3 Effect of the Inclination Angle Direction

The inclination angle of the tooth profile is allowed to be either positive or negative. Two example cases (Seal *G*, Seal *J*) were selected to investigate the effect of the inclination angle direction. They were generated from the baseline seal, Seal *A*, with Seal *G* and *J* being given a $+5^\circ$ inclination angle and a -5° inclination angle, respectively.

A comparison of the mass flow coefficient of these two geometries at different pressure ratios is shown as Figure 5.12. For reference, the baseline Seal A is also included. It is clear that seals with positive inclination angles have better sealing performance than the baseline seal. Moreover, for Seal G, which is angled into the flow, the increase over the baseline effect was approximately doubled that for Seal J, inclined with the flow. Figure 5.13 and Figure 5.14 present the vorticity magnitude contours of the two examples seals.

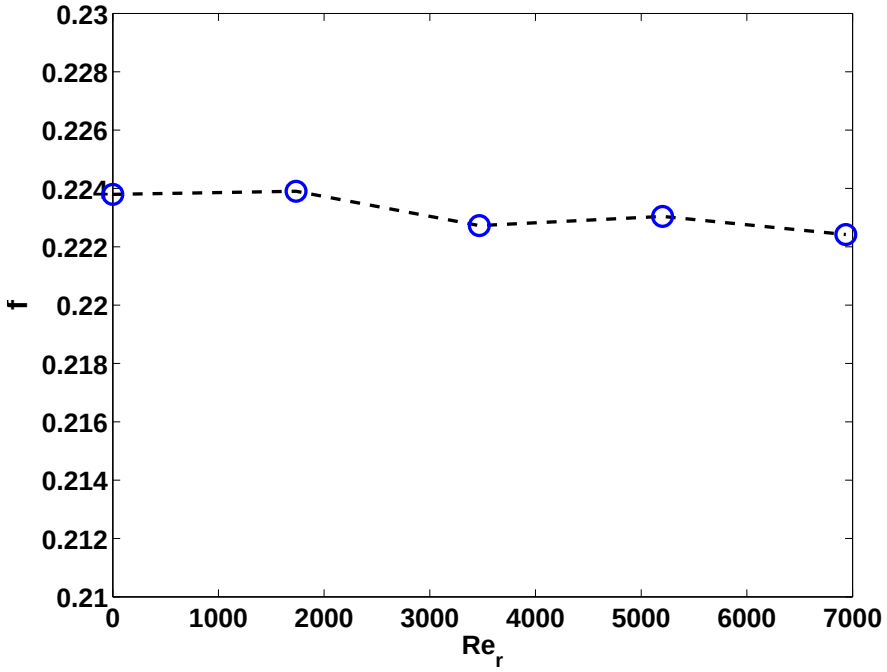

Fig. 5.11 Leakage flow coefficient at different rotational speeds.

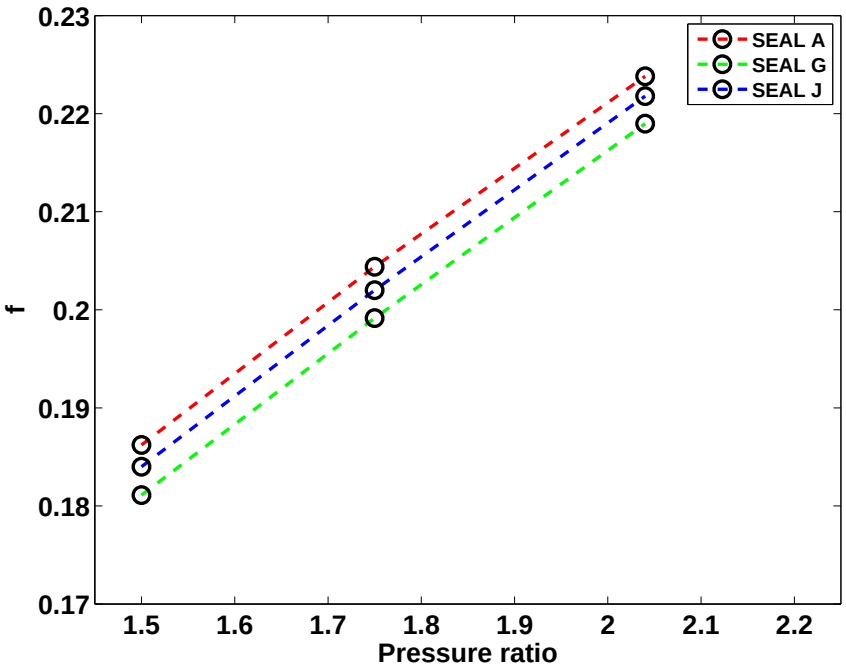

Fig. 5.12 Mass flow coefficient between seals *A*, *G* and *J*.

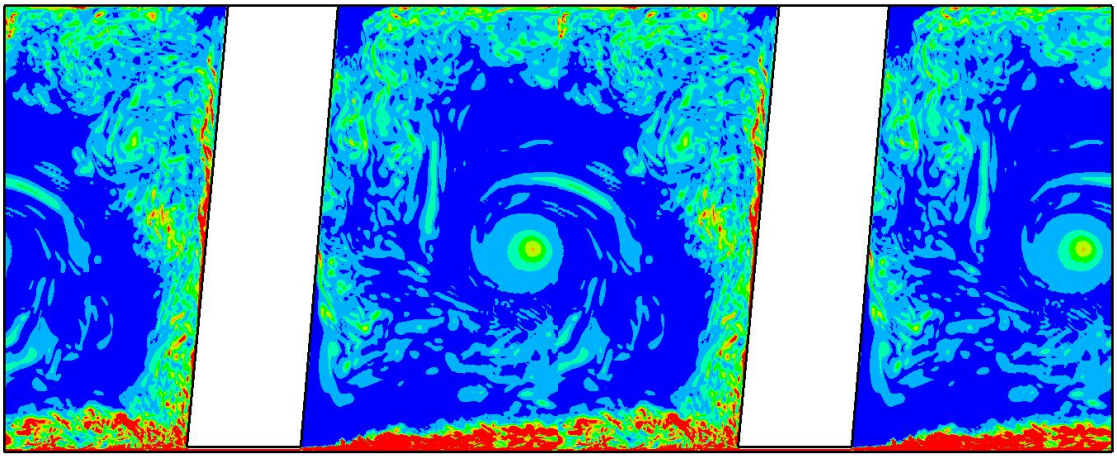

Fig. 5.13 Instantaneous vorticity magnitude contours for Seal *G*.

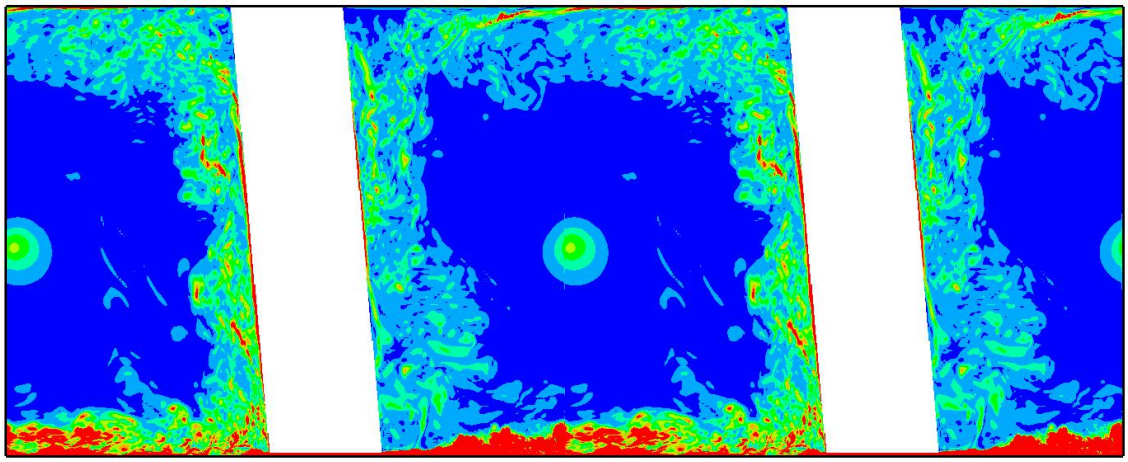

Fig. 5.14 Instantaneous vorticity magnitude contours for Seal *J*.

From the above test results and previous studies in the literature (see Chapter 2), five geometrical parameters were determined. They are: the inclination angle (θ); clearance size (δ); tooth width (L); number of grooves (n); and groove width (l). The parameters and their allowable ranges are given in Table 5.1. A schematic indicating the corresponding model and geometrical parameters is given in Figure 5.15. These geometrical parameters of the seal geometry are then used to generate hundreds of individuals as the input design variables over the course of the *GA*.

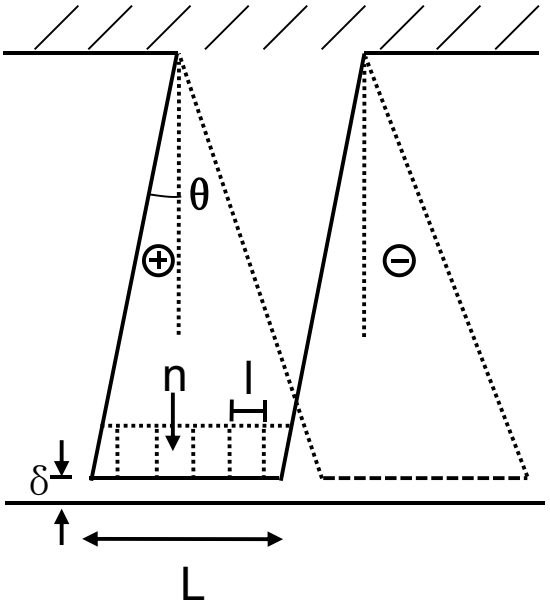

Fig. 5.15 Schematic model for the *GA* parameters.

Table 5.1 Variables and the corresponding constraints.

Variables	Constraints
Inclination angle (θ)	[-20°,20°]
Clearance size (δ)	[0.08, 0.12] (*mm*)
Tooth width (L)	[2.54, 3.81] (*mm*)
Groove width (l)	[0.3175, 1.27] (*mm*)
Number of grooves (n)	[1, 9]

5.6 Optimisation Results

After the determination of the optimisation algorithm, and the corresponding parameters, a wide range of optimisation design is carried out. Through the genetic optimisation process, an optimised design is obtained. By analysing the evolutionary process, it is possible to see how the optimisation advanced and the optimal values found within each generation.

5.6.1 The Progress of the Evolution

The average performance of each generation is presented in Figure 5.16. As the populations in the first generation were randomly generated, the corresponding performance is not so good. Thus there is considerable scope for improvement over the next generations. After the first generation, an average reduction of 8.5% of the mass flow rate was achieved when compared with the initial geometry configuration. The rate of the improvement begins to slow by about the fourth generation, as further improvements have a stronger dependence on the random mutations, so higher peaks are increasingly rare. For the second generation the average reduction was up to 4.0%.

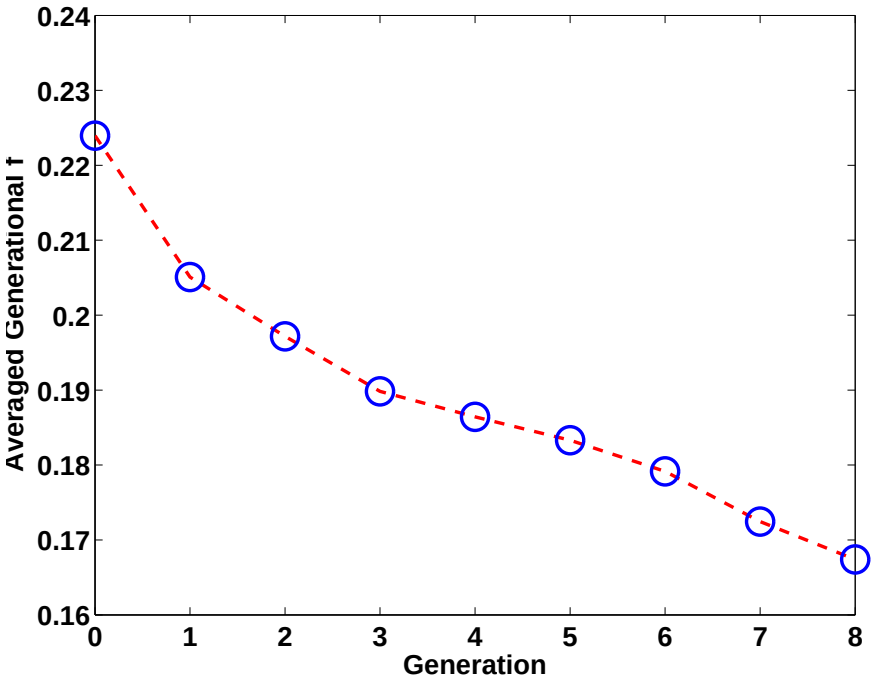

Fig. 5.16 Improvement in averaged generational performance.

Figure 5.17 shows the development of the relationships between the mass flow coefficient and the blockage ratio (δ/L), where the symbol "+" represents the first generation, "$\circ$" shows

the third generation and "♢" the fifth. The performance gains over these three generations can be seen from this figure, as well as the tendency the optimiser had to reduce the blockage ratio. These effects are especially clear between the first and the third generations.

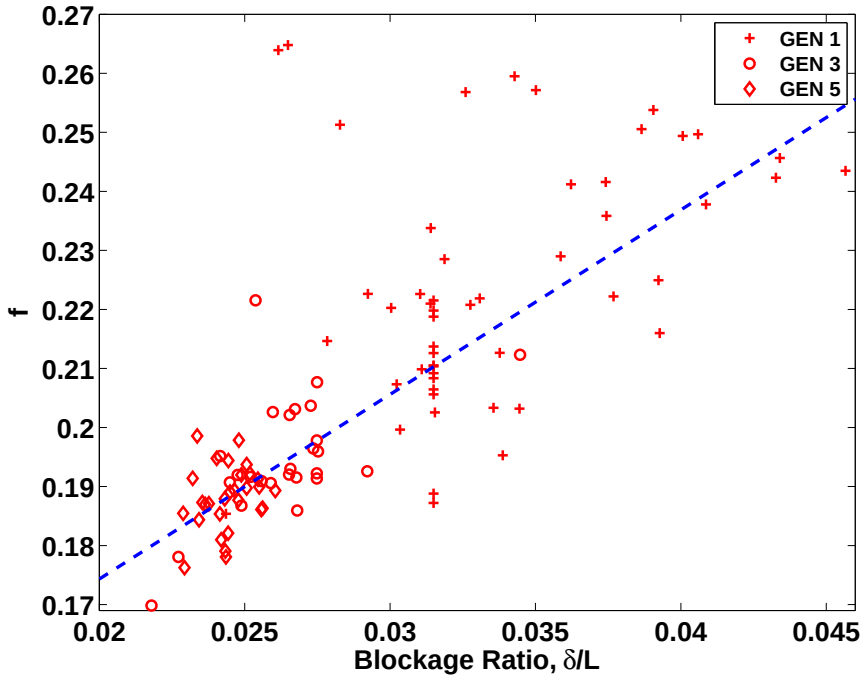

Fig. 5.17 Generational development of mass flow coefficient vs. blockage ratio at $PR = 2.04$.

5.6.2 Empirical Relations

As well as producing the optimal design, the calculations carried out on the way can also give useful information. Here the relationships between the sealing performance and various design parameters are presented using the populations from the final three generations. By this time, the gene pool has become largely saturated with "good" genes. The correlation lines on each scatter plot are determined using a Theil-Sen median slope estimator. This estimator can be computed efficiently, and is insensitive to statistical outliers. As defined by Theil [103], in each correlation line the slope is chosen as the median slope among all lines through pairs of points. Once the slope m has been determined, the y- intercept b is given by the median y–intercept of each of these gradients.

As expected the correlations between the overall performance and each geometrical parameter are fairly weak (as shown by the correlation coefficient). This is because, when conducting the optimisation process using *GA*, there is no requirement to alter only one parameter at one time. Figures 5.18 – 5.21 plot the mass flow coefficient against clearance

size, inclination angle, tooth width and groove width, respectively. The Theil-Sen median slope, m, and correlation coefficient, R_f, for these parameters are shown in Table 5.2.

For all the figures of merit explored, the clearance size was found to be a critical parameter with the strongest correlations (R_f = 0.64), as shown in Figure 5.18. It means that the clearance size has the most influence on the sealing performance. This is not unexpected, as with larger clearance more fluid can be expected to flow over the tooth without being influenced (or less strongly influenced) by the tooth. As a result, a larger portion of the kinetic energy is carried over to the next cavity without being dissipated in the vortex. Thus, the percentage of the kinetic energy carried over to the next cavity increases and accordingly the mass flow coefficient increases. The second most important parameter was the tooth width with R_f = 0.30, as shown in Figure 5.20.

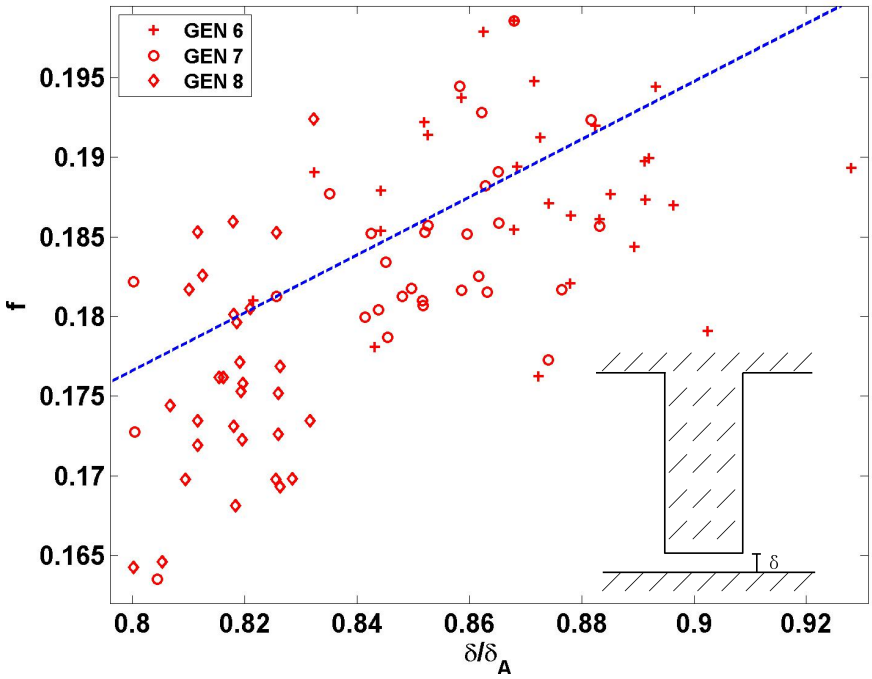

Fig. 5.18 Scatter plot of mass flow coefficient against clearance size.

5.6.3 Optimised Design

Geometry

The most successful seal tooth configuration from the final generation is shown in Figure 5.22. Table 5.3 gives the geometrical parameters for the optimised configuration. Also shown are the geometrical parameters of the initial baseline configuration.

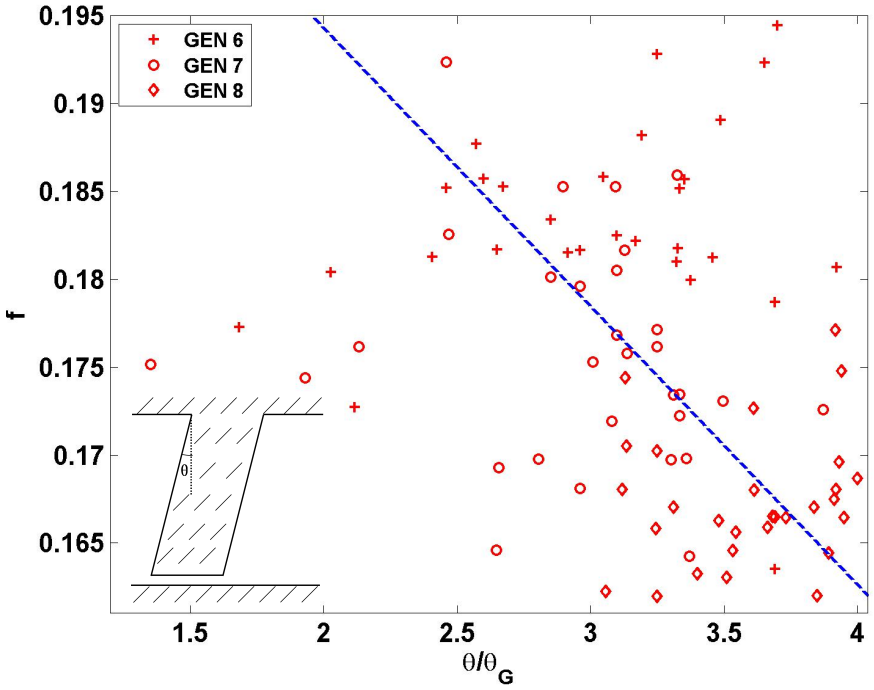

Fig. 5.19 Scatter plot of mass flow coefficient against inclination angle.

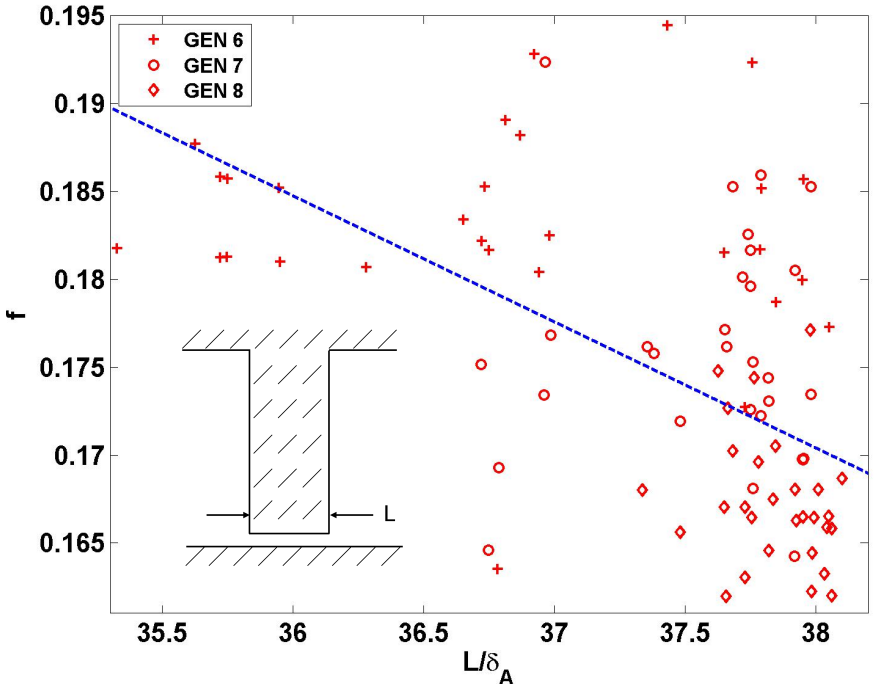

Fig. 5.20 Scatter plot of mass flow coefficient against tooth width.

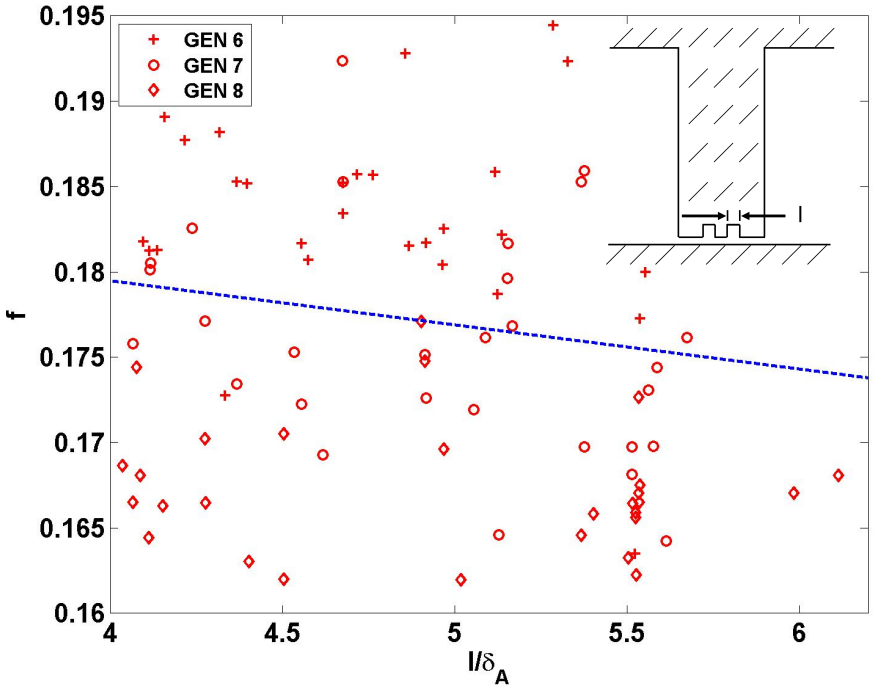

Fig. 5.21 Scatter plot of mass flow coefficient against groove width.

Table 5.2 Quantities of interest over optimisation.

Parameter	m	R_f
Blockage ratio	3.127	0.74
δ	1.815	0.64
L	-0.072	0.30
l	-0.026	0.28
θ	-0.002	0.12

Table 5.3 Comparison of design parametres between the baseline seal and optimised seal.

	δ (mm)	L (mm)	θ $(^\circ)$	l (mm)	n
Seal A	0.1	3.175	0	0	0
Optimised seal	0.08	3.7656	16.25	0.5478	3

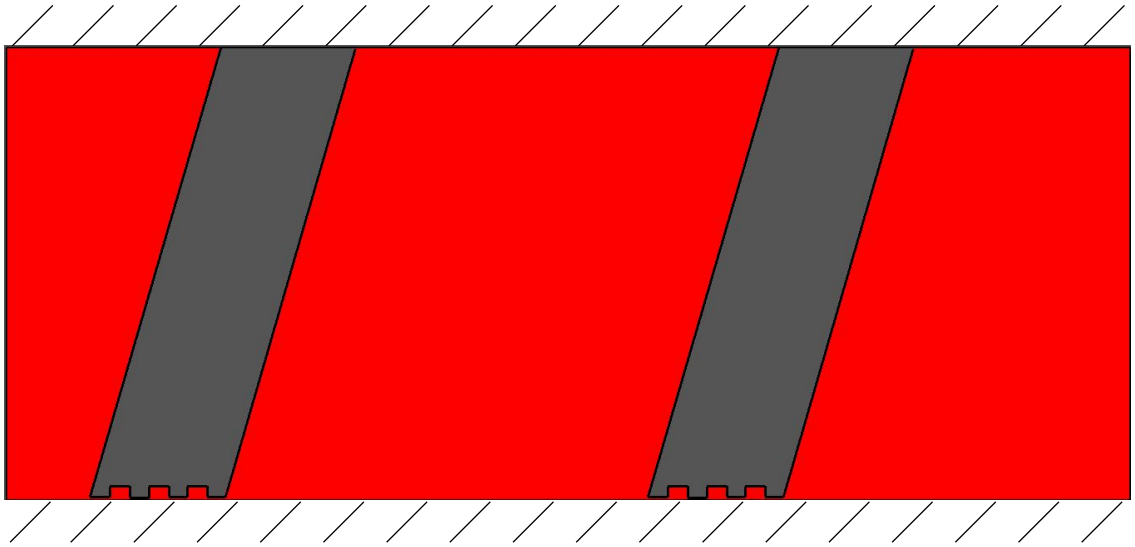

Fig. 5.22 Optimised labyrinth seal layout.

The mass flow coefficient of this optimised labyrinth seal was found to be significantly better than that of the baseline seal. A significant reduction of 27.6% in the mass flow coefficient through the seal was observed. By simply qualitatively comparing the configuration of the best performing labyrinth seal and that of the baseline seal, it is clear why the latter has a significantly higher mass flow coefficient. The best performing geometry consists of three grooves which are quite evenly spaced in the streamwise direction. These generate substantially 50% higher turbulence relative to the baseline seal. This significantly increases loss and hence the effort required to force the fluid between the seals. The high speed wall jet from the baseline Seal *A* is more likely to impinge directly onto the tooth of the next downstream cavity.

Flow Fields

In order to better understand the capability of the optimised design to control the flow leakage, the flow field is briefly analysed. The instantaneous vorticity magnitude is compared for the optimised seal and the baseline seal in Figure 5.23. As can be seen, at the exit of the seal a wall jet is generated. Fluid from the cavity is highly accelerated into the seal gap. On exit, it decelerated rapidly, forming a turbulent shear layer next to the lower wall. Also, it can be seen that the flow penetration into the cavity is moderate and the flow decelerates in the corner regions of the cavities. The shear layer for the optimised seal is thicker than that for Seal *A*. This is also shown in the averaged vorticity magnitude contours in Figure 5.24. This increased thickening is due to more mixing and hence loss. This gives the improved sealing.

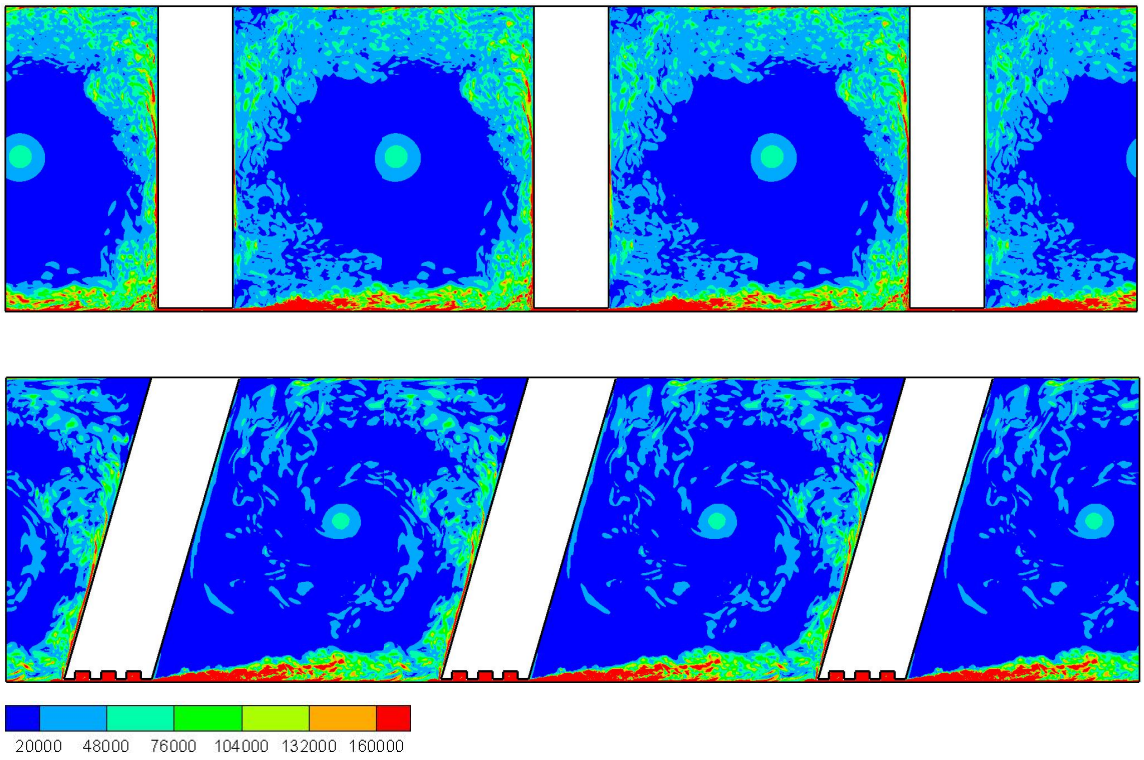

Fig. 5.23 Comparison of instantaneous vorticity magnitude between the baseline Seal *A* and optimised design.

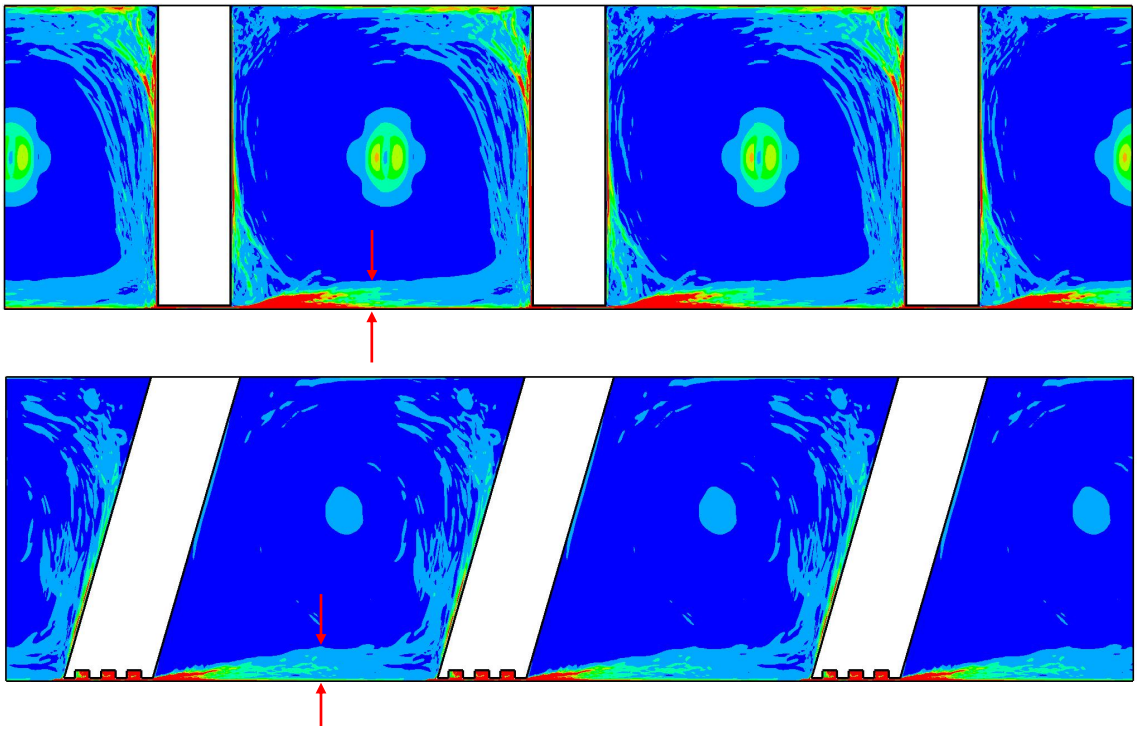

Fig. 5.24 Comparison of time-averaged vorticity magnitude between the baseline Seal *A* and optimised design.

To identify the fluid structures more clearly, contours of the Q-criterion are plotted in Figure 5.25. The flow appears to spread after passing through the seal gap. After passing through the clearance, the main flow path comes to the next cavity. The flow then begins to accelerate again, with vortices becoming stretched near the upper part of the seal clearance, and large recirculations are generated with larger coherent structures. Small vortices are also generated in the boundary layer. Hence a mixed flow is formed together with the larger vortical structures, which further improves the sealing performance.

5.7 Conclusions

The present study investigated the effect of geometry on the leakage mass flow coefficient for around three hundred different labyrinth seals. The clearance size, inclination angle, number of grooves, tooth width, and groove width were specified as design variables. *RANS* calculations have previously been shown to be inadequate, whereas the flow structures can be reliably produced using *LES*.

Multiple geometries were generated using the genetic algorithm, controlled by the selected geometrical parameters and manufacturing constraints. Geometries are generated in

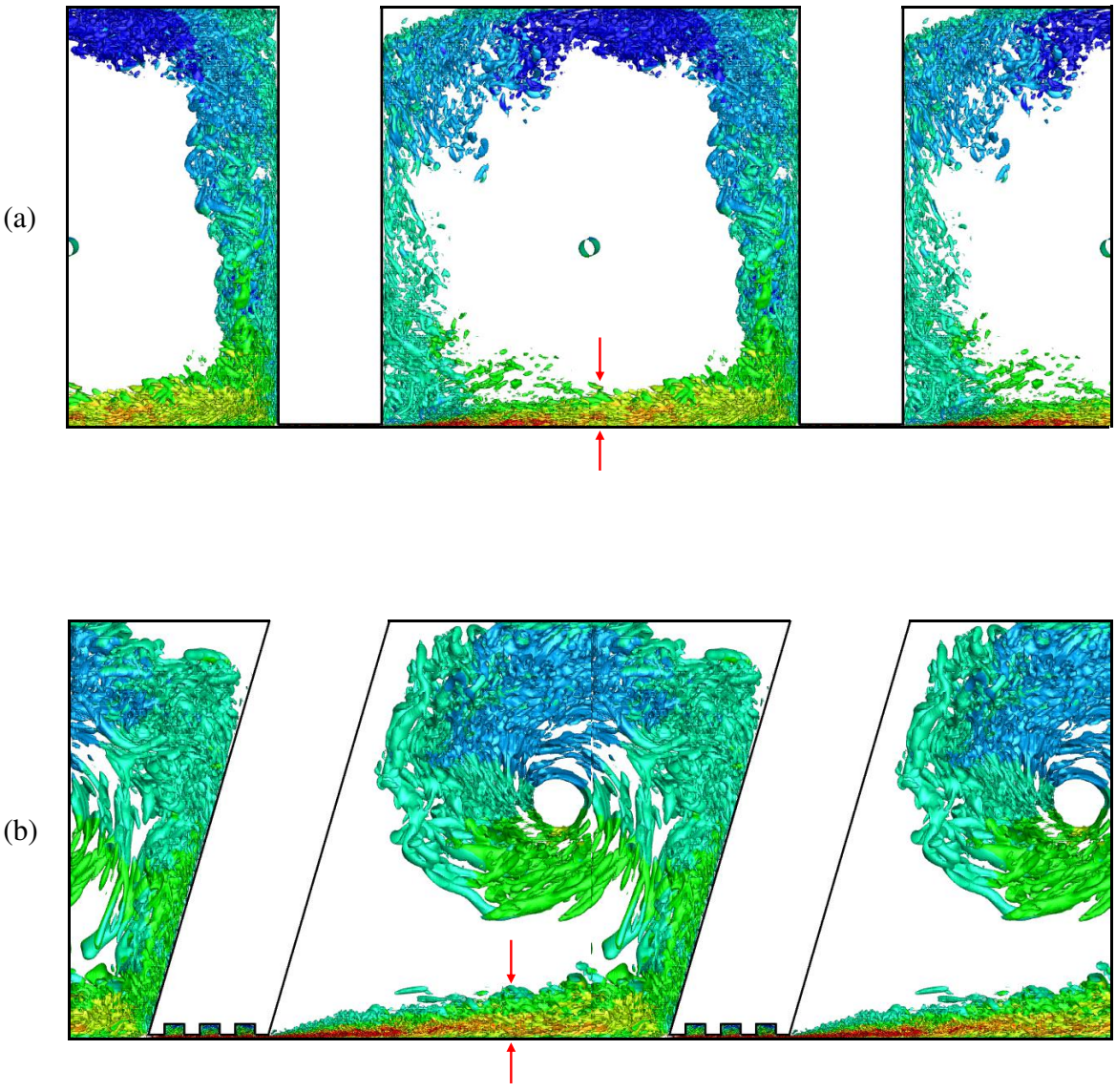

Fig. 5.25 Comparison of Q-criterion iso-surface between the baseline Seal A and optimised design.

sets, representing a population for each evolutionary generation. The range of geometries is represented using an *IBM* on a background Cartesian grid. This avoids the need to laboriously mesh by hand, or to trust in automatic meshing software and inevitable failures. As a further benefit, the computational cost of each of the individual simulations could be reduced by the use of an efficient structured solver. *IBM* gives a much easier way to resolve the wide range of complex geometries with a simple mesh.

The best performing seal is that with the lowest mass flow coefficient, f, for the applied pressure gradient. In comparison to the baseline geometry, the design optimised by the *GA* showed a leakage reduction of about 27.6%. The optimal design consisted of a seal inclined towards the flow directio with grooves at its tip. Along with this, among the five variable design parameters, the effect of the clearance size, δ, had the greatest effect ($R_f = 0.64$) on the mass flow coefficient. The second most important parameter was the tooth width, L, with $R_f = 0.30$.

The use of Large Eddy Simulation for large scale design exercises has only recently come within the reach of modern computational systems. With careful problem selection, such as the labyrinth seals shown here, the use of a genetic algorithm based optimising heuristic can achieve significant design improvements in relatively short real time scales even on a modest local cluster.

Chapter 6

Sealing Mechanisms

6.1 Introduction

The purpose of labyrinth seals is to reduce fluid leakage by increasing resistance to fluid flow. This can be realised by dissipating as much of the kinetic energy of the fluid as possible. Due to their simplicity straight-through labyrinth seals are mainly used in turbine engines. This design, however, has a larger mass flow coefficient than the honeycomb seal (as discussed in the literature review) or optimised design in this study (see Chapter 5). Using *LES*, a more in depth study of turbulence generated in the flow can be achieved. This section illustrates the flow physics through various labyrinth seals in order to understand the sealing mechanisms and to further improve the sealing performance. The baseline Seal *A* and honeycomb seal are chosen as typical seals (found in practical applications) and are analysed in detail. The effects of the optimisation parameters explored in Chapter 5 on the mass flow are also investigated. Finally, the optimised design from Chapter 5 is combined with the honeycomb seal, and a reduction of 30.6% on leakage is obtained compared to the baseline case.

6.2 Seals with Honeycomb

As discussed in the literature review (see Chapter 2), honeycomb seals have shown the potential to reduce leakage. Thus the effect of honeycomb seals on the leakage performance is taken into consideration.

6.2.1 Computational Setup

The configuration of the labyrinth honeycomb seal is shown in Figure 6.1, in which honeycomb cells are located beneath the tooth. The sealing clearance for the honeycomb case is

set as the same as the baseline Seal *A*. Three times the sealing clearance is used as the depth of the honeycomb cells. The honeycomb cell diameter $L_h = 2.3$ mm. Figure 6.2 shows the structured computational grid used in the honeycomb seal. The mesh size for the honeycomb seal simulation is approximately 13.8 million. Typically $y+$ is less than 1 at walls, with at least 150 nodes inside the turbulent boundary layer. Also, $\Delta x^+ = 10$, $\Delta z^+ = 20$, as for other cases are consistent with quasi-*DNS*. The boundary conditions are kept consistent with the baseline seal model in section 5.2.1.

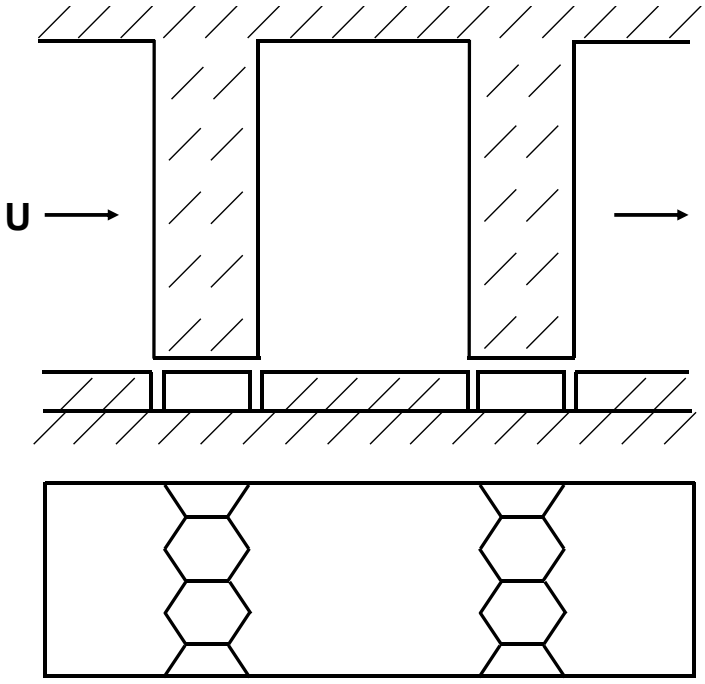

Fig. 6.1 Configuration of the honeycomb seal.

6.2.2 Mass Flow Results

Figure 6.3 compares the leakage flow rate between the smooth seal and honeycomb seal under different pressure ratios. Like the smooth seal, the increase in leakage rate is also almost linearly proportional to the pressure ratio for the honeycomb seal. The numerical calculation shows that the labyrinth seal with the honeycomb structure has a better sealing effect. The honeycomb configuration reduced the leakage flow rate by 4% relative to that of the smooth configuration at *PR* of 2.04.

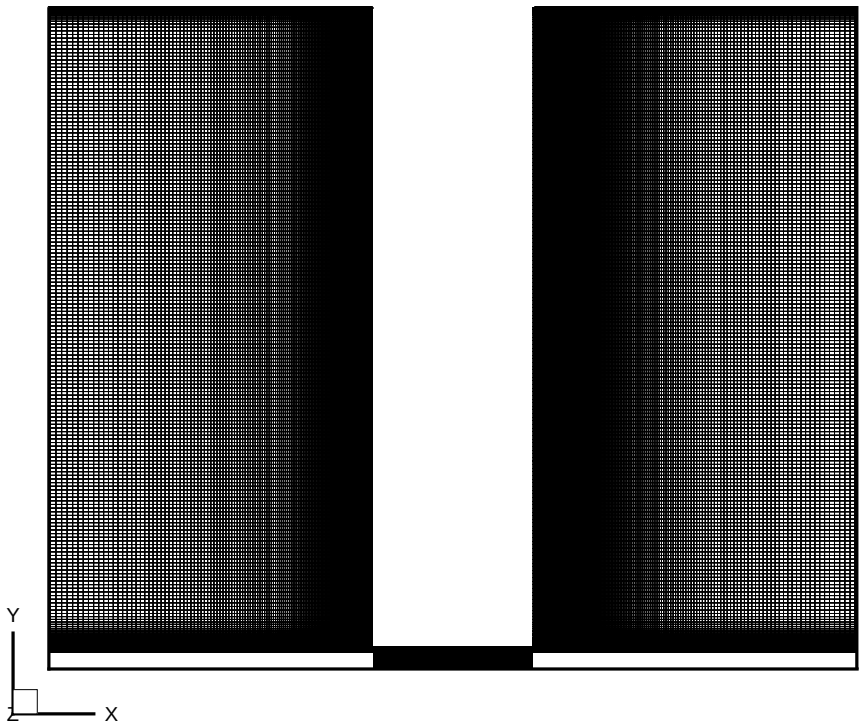

Fig. 6.2 Structural mesh of the honeycomb seal.

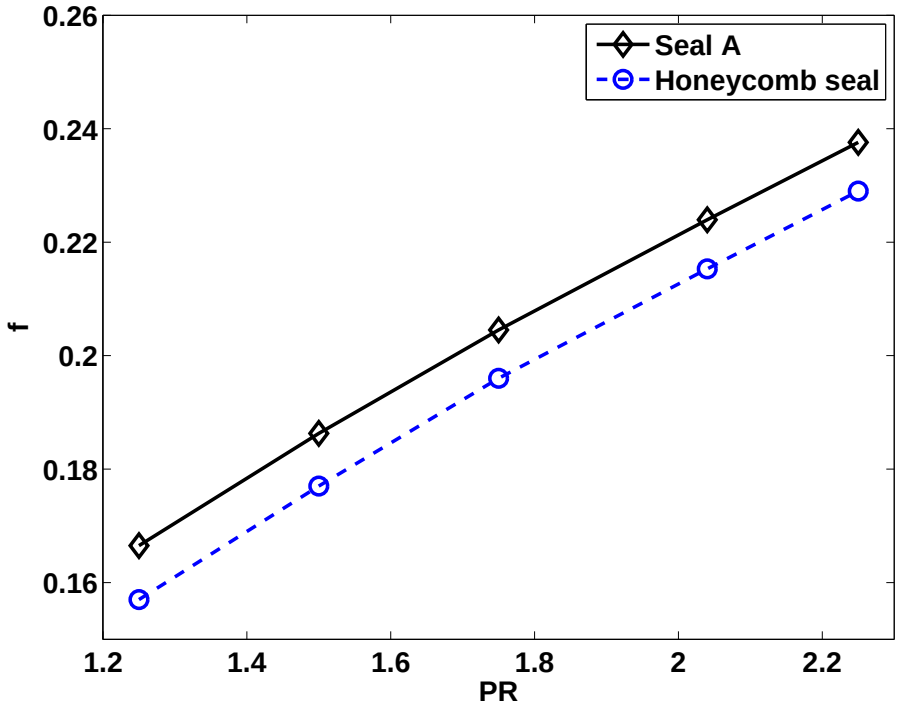

Fig. 6.3 Comparison of mass flow coefficient vs. pressure ratio between Seal *A* and the honeycomb seal.

6.3 Comparison between Baseline Seal and Honeycomb Seal

6.3.1 Flow Fields

Flow Fields for The Baseline Seal

The sealing tooth plays an important role in controlling leakage. Figure 6.4 shows static pressure contours for Seal *A*. There is an extreme pressure gradient at the seal clearance entrance. This is because when the fluid flows through the clearance, a large part of the pressure is converted into kinetic energy. The generated jet subsequently enters the cavity and expands further to form a large vortex as the velocity decreases. This vortex dissipates the kinetic energy of the fluid through small scale turbulence. Kinetic energy is hence turned into thermal energy. The whole process is governed by the leakage jet generated by the clearance gap, and the interaction between the leakage jet and the main flow. This interaction will be explored next in terms of energy transfers.

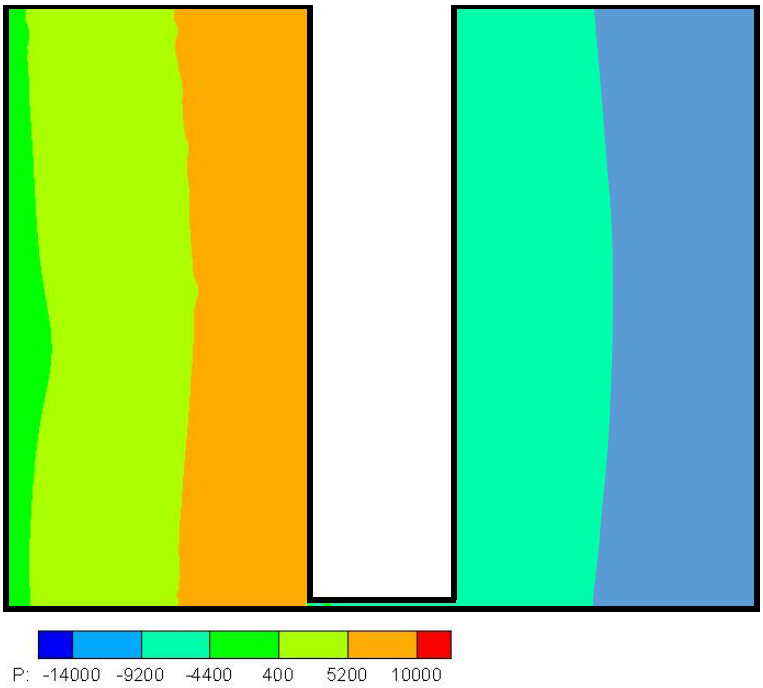

Fig. 6.4 Pressure contours of Seal *A*.

Figure 6.5 presents the typical flow pattern within Seal *A* (the basic, straight-through seal). The labyrinth seal case in this study is investigated assuming bi-periodic flow as outlined in Chapter 5. Here, periodic sections in the streamwise direction are repeated to make the flow structure easier to follow. Large recirculations are generated within the cavity. From the streamlines it is also observed that, a part of the wall bounded jet continues under the next

tooth without recirculation. This is indicated in terms of the angle β. Inside the cavity, two small recirculations also exist at the front and back corners of the seal. These are marked $R1$ and $R2$. Another small reciculation is formed at the entrance of the seal clearance. This is enlarged in the lower part of Figure 6.5. It has an extent of around 7% of the tip gap length, and masks the more critical flow near the tip clearance. There is also a large change of flow direction at the entrance of the clearance. With the presence of high axial velocity near the lower wall as shown in this lower figure, the fluid is accelerated through the narrow tip gap. These accelerations cause a highly inflectional free shear layer and hence large pressure losses after passing the tooth.

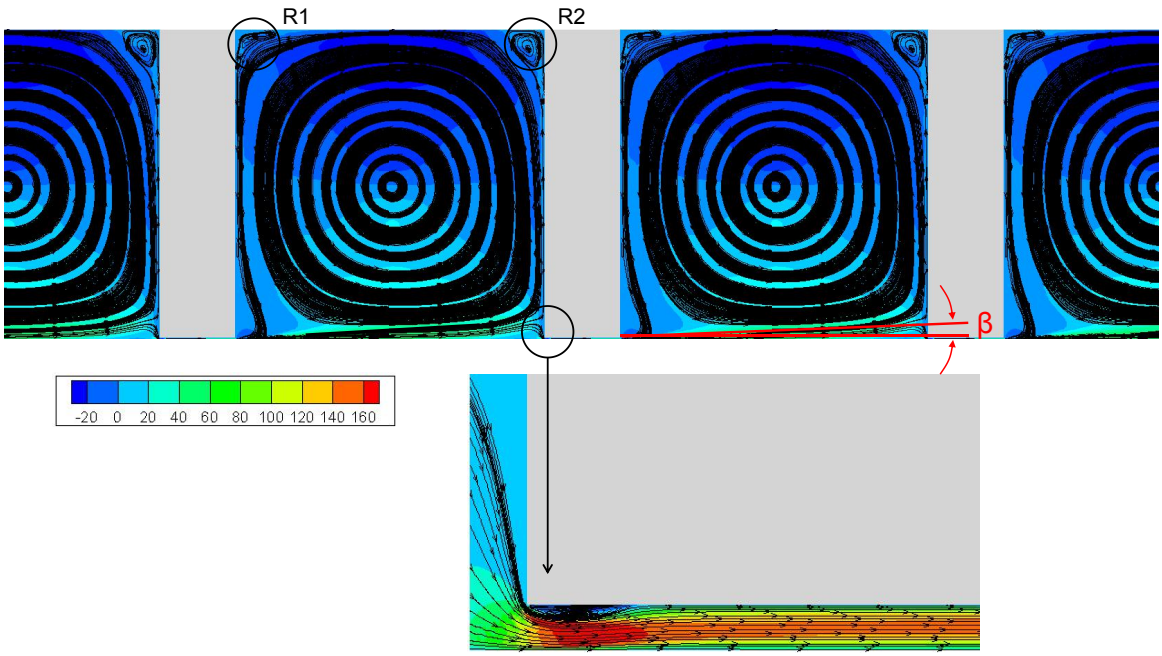

Fig. 6.5 Periodic streamlines, seal tip recirculation and axial velocity contours of Seal A.

The instantaneous and time-averaged vorticity contours for Seal A are presented in Figures 6.6 and 6.7. Figure 6.6 shows that the flow is rich in turbulent structures. Regions of high vorticity can be seen at the lower wall. A strong wall bounded jet is formed at the exit of the tip clearance. The flow separates after passing through the clearance, with vortices shedding from the tooth tip. As shown in Figure 6.7, the jet forms a recirculation as it spreads into the cavity zone before part of the jet is re-accelerated into the next seal gap. Vorticity, generated by the jet impinging on the downstream seal tooth surface can also be found near the upper seal surfaces. Energy is lost in the jet shear layer, driving the recirculation.

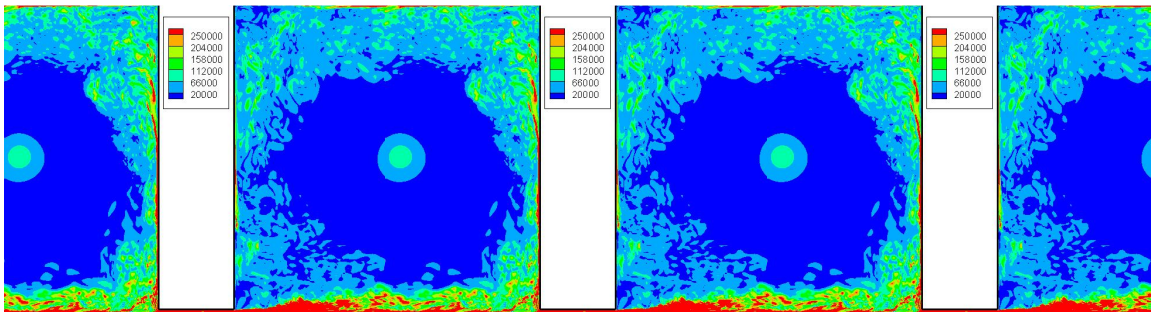

Fig. 6.6 Instantaneous vorticity magnitude contours of Seal *A*.

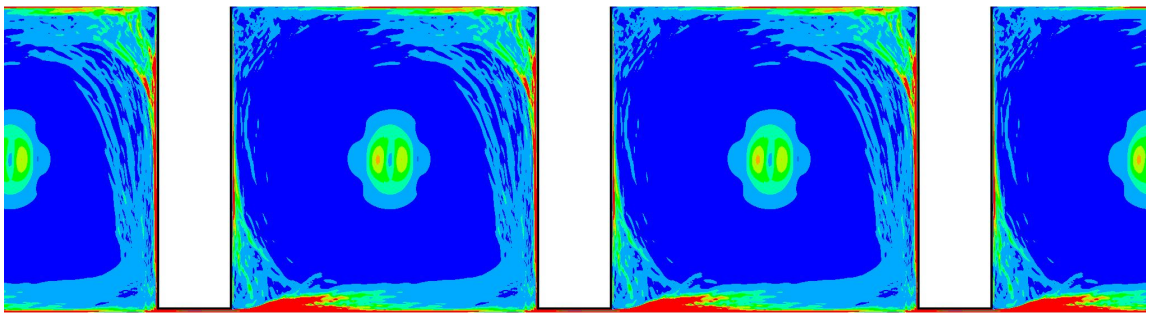

Fig. 6.7 Time-averaged vorticity magnitude contours of Seal *A*.

Flow Fields for The Honeycomb Seal

The streamlines and axial velocity contours on the mid x–y plane of the honeycomb seal are presented in Figure 6.8. The general flow structure inside the cavity remains similar to that of the baseline seal presented in Figure 6.5, where a large vortex is also formed in the centre of the cavity. At the same time, compared with the smooth seal, an area with lower velocity at the bottom is found (see Figure 6.8). Moreover, with the honeycomb structure applied at the lower wall, more small scale turbulence is also generated.

Figure 6.9 shows the streamlines inside the honeycomb cell. Fluid flows into the honeycomb cell, and a relatively strong vortex is formed at the centre of the honeycomb cell, driven by the viscous shear layer above (*A*). This recirculation zone is observed within each honeycomb cell, and a transfer of the kinetic energy into thermal energy also occurs here. At the side position of the honeycomb cell, much smaller vortices (*B*) are observed caused by colliding fluid spilling out of the cell.

Instantaneous and time-averaged vorticity magnitude contours for the honeycomb seals are presented in Figures 6.10 and 6.11. Like the smooth seal, high vorticity near walls and in regions of separation can be found. The subsequent separated flows will hence be influenced

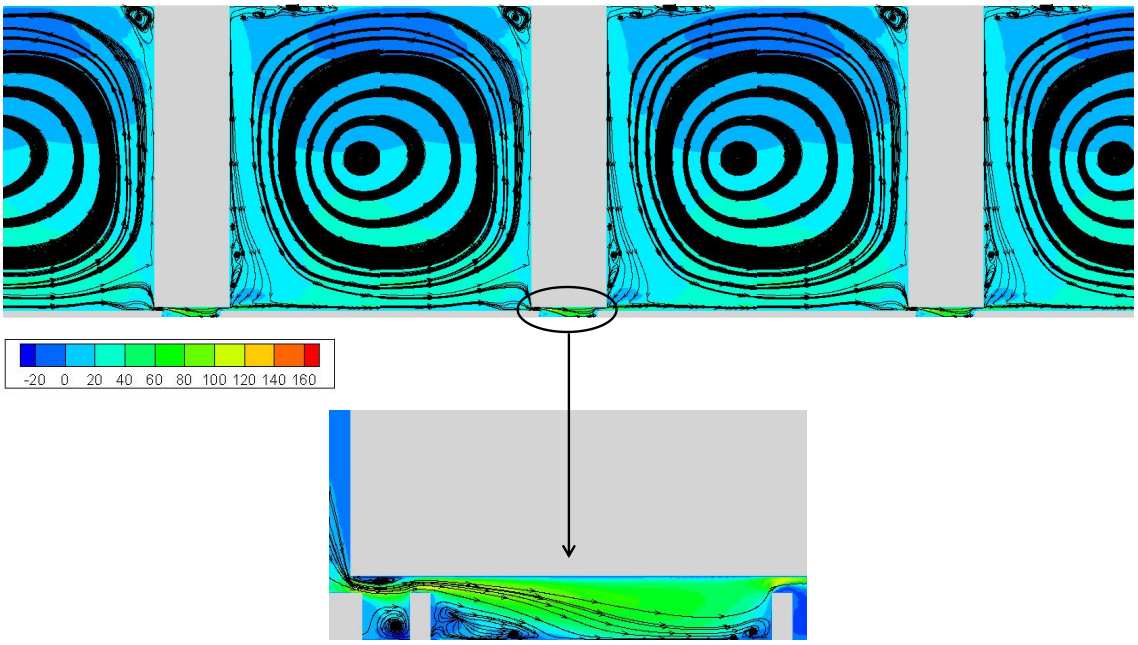

Fig. 6.8 Streamlines and axial velocity contours of the honeycomb seal.

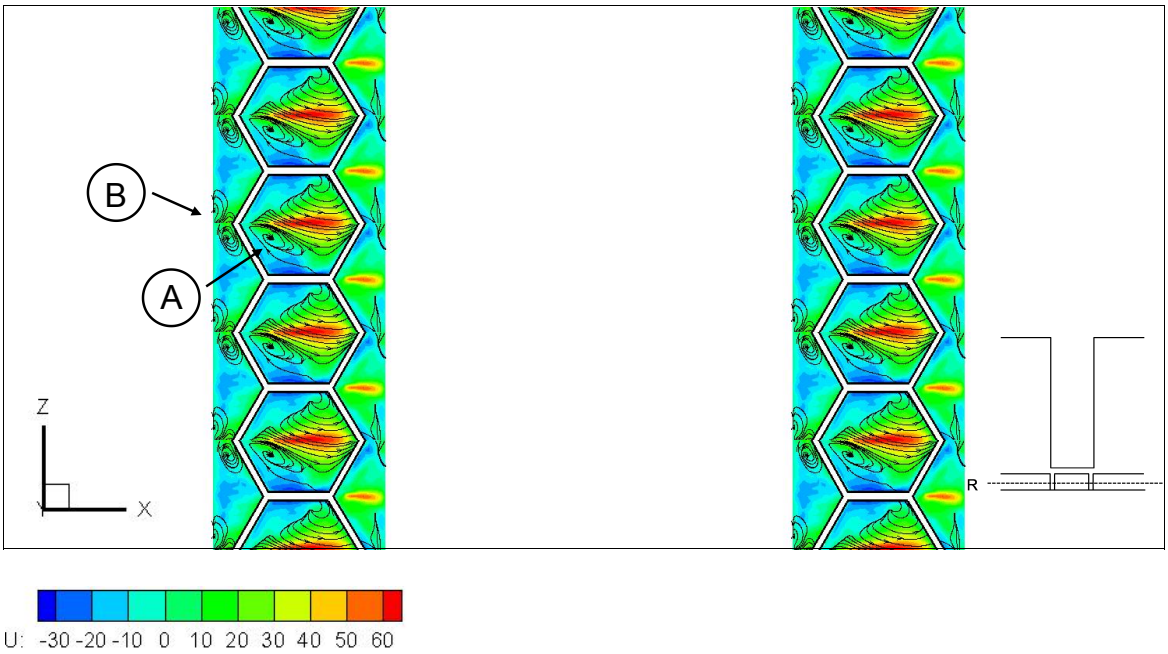

Fig. 6.9 Streamlines and axial velocity contours inside the honeycomb cell at *R*.

by the turbulence formed by the honeycomb cell. Compared with the vorticity magnitude contours in Figure 6.6, the secondary flow field for the honeycomb seal is much thicker than that of the smooth seal, due to enhanced turbulence mixing. Figure 6.12 compares the turbulence intensity between the baseline Seal *A* and honeycomb seal. The turbulence intensity is the averaged value taken from the clearance area, as shown in Figure 6.12. It can be seen that the turbulence intensity of the honeycomb seal is increased by around 25% with respective to the value of the baseline seal. Higher turbulence intensity increases the turbulence effect in the shear layer.

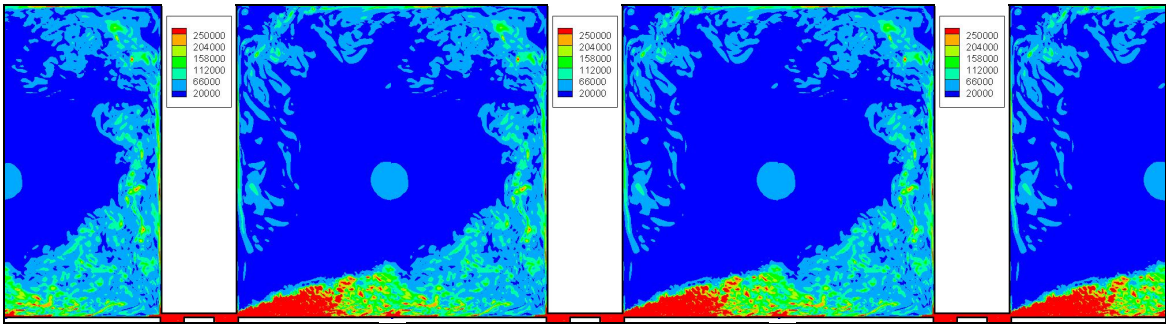

Fig. 6.10 Instantaneous vorticity magnitude contours of the honeycomb seal.

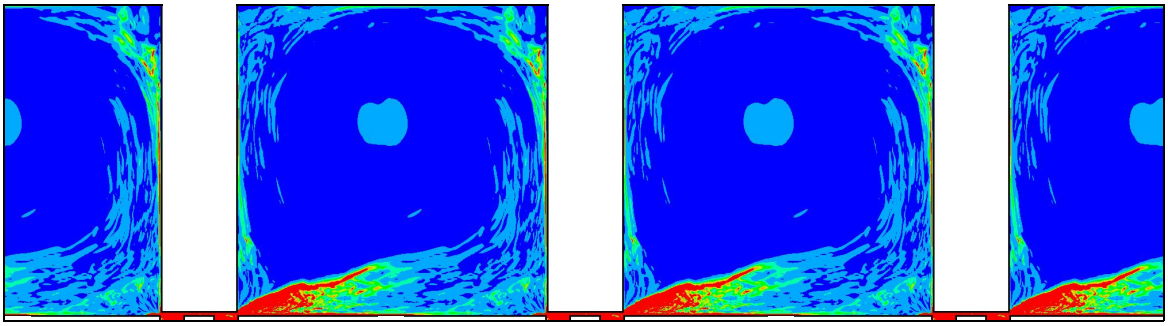

Fig. 6.11 Time-averaged vorticity magnitude contours of the honeycomb seal.

6.3.2 Velocity Profiles

Figures 6.14 compares the axial velocity distributions between the baseline Seal *A* and the honeycomb seal. Nondimensionalisation is kept consistent with that of Denecke et al. [20]. Here, $U_{max} = 140$ m/s. Profiles are extracted along locations *A* and *B*, the seal tip centre and the cavity centre (see Figure 6.13). As discussed in the previous results, for the axial velocity along profiles *A* and *B*, the maximum values appear in the near wall region at the seal gap exit. The acceleration causes the structure of the near wall turbulence to change significantly.

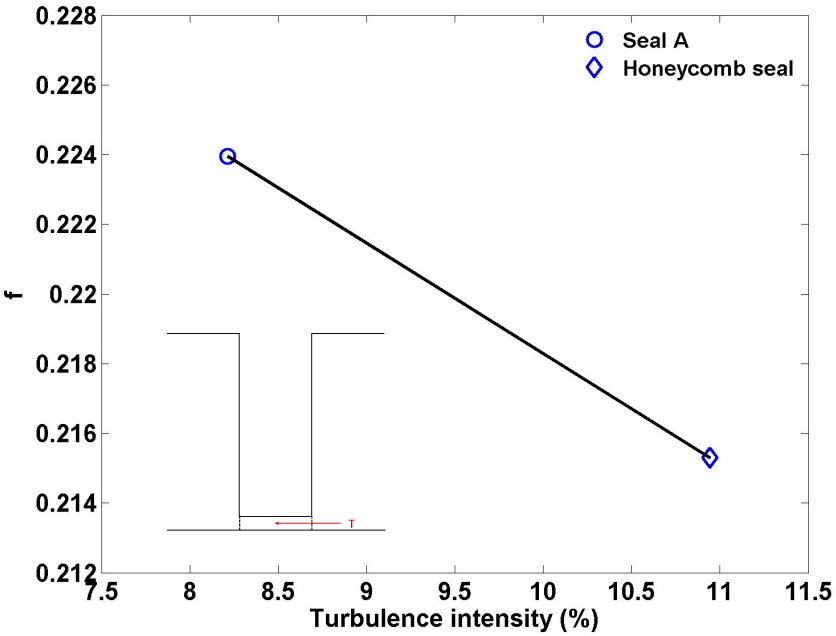

Fig. 6.12 Comparison of turbulence intensity of Seal *A* and the honeycomb seal.

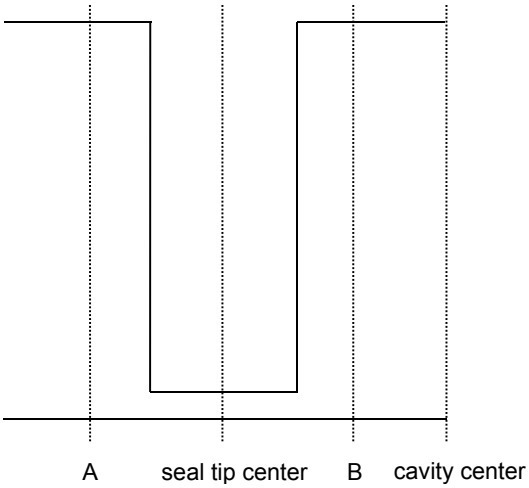

Fig. 6.13 Schematic to show the position to extract the velocity profiles and TKE budget.

The leakage jet then spreads, and re-enters the main cavity with a reduced axial velocity caused by the increase of surface roughness, as can be seen through the velocity distribution along the cavity centre in Figure 6.14(*d*). For the results along profiles *A* and *B*, although there is little variation between these seals in the cavity zone, in the near wall region the axial velocities for the honeycomb seal are much smaller. This is also obviously shown in the comparison results in the seal tip centre in Figure 6.14(*b*). This is because a decay of small scale turbulence is generated by the honeycomb cells (Figure 6.8). The lower velocities in the honeycomb seal indicate the increased level of blockage and associated reduction in mass flow achieved in comparison to the smooth seal.

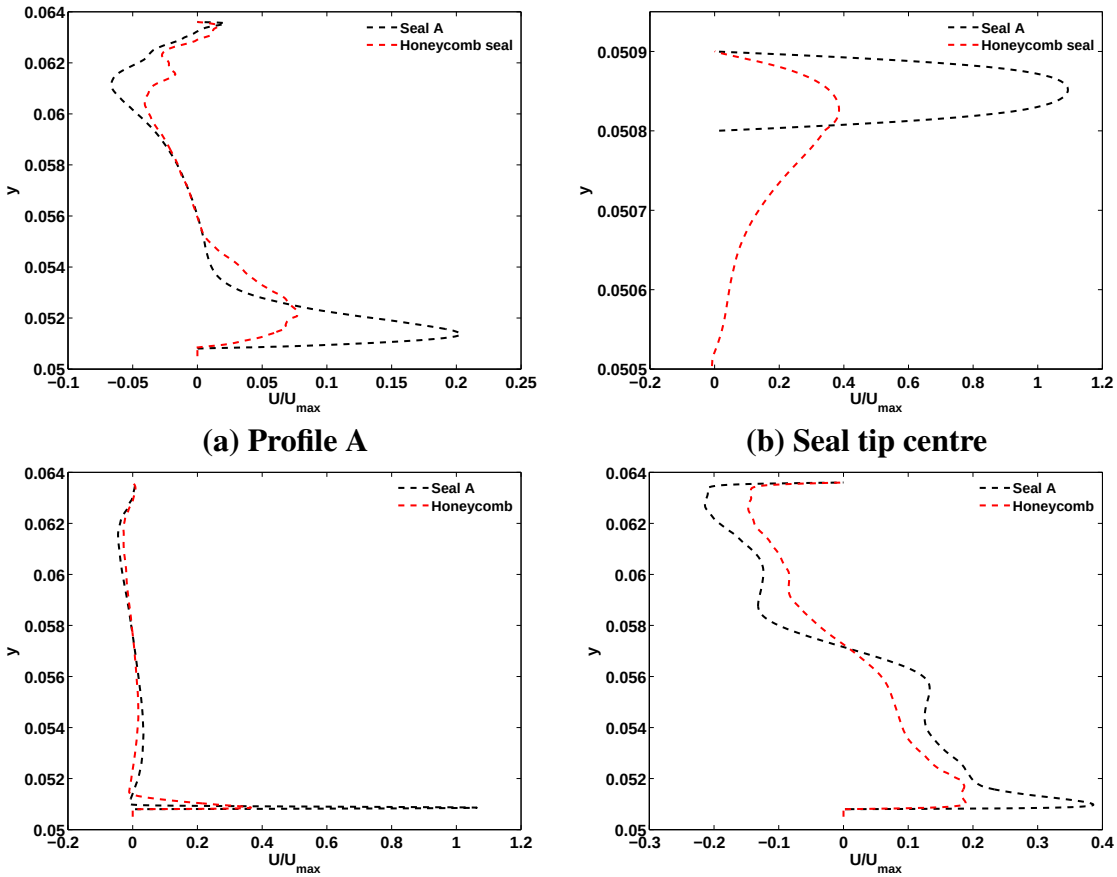

Fig. 6.14 Axial velocity profiles between Seal *A* and the honeycomb seal.

Figures 6.15 and 6.16 show a comparison of turbulent Reynolds stresses. Using *LES*, a more in depth study of turbulence generated in the flow can be achieved. The impact of different types of seal on the turbulent quantities is more obvious. For the Reynolds stress profiles $\overline{u'u'}$ and $\overline{v'v'}$, along profile *A*, the values of Seal *A* are much larger than the

honeycomb seal, especially for the near wall gradients. The complex flow near the tip clearance largely determines the flow in the cavity. Along profile B, after passing through the clearance, maximum $\overline{u'u'}$ and $\overline{v'v'}$ values are also found in the shear layer region, as can be seen in Figures 6.15(c) and 6.16(c). Due to the extreme acceleration at the entrance to the seal clearance, the velocity fluctuations tend towards a frozen state. These frozen disturbances then promote rapid re-transition to turbulence in the exit region of the clearance gap. Further downstream, these two seals tend to have a much lower turbulence level in the cavity centre (see Figures 6.15(d) and 6.16(d)). The $\overline{v'v'}$ values reach nearly the same values in the cavity centre profile.

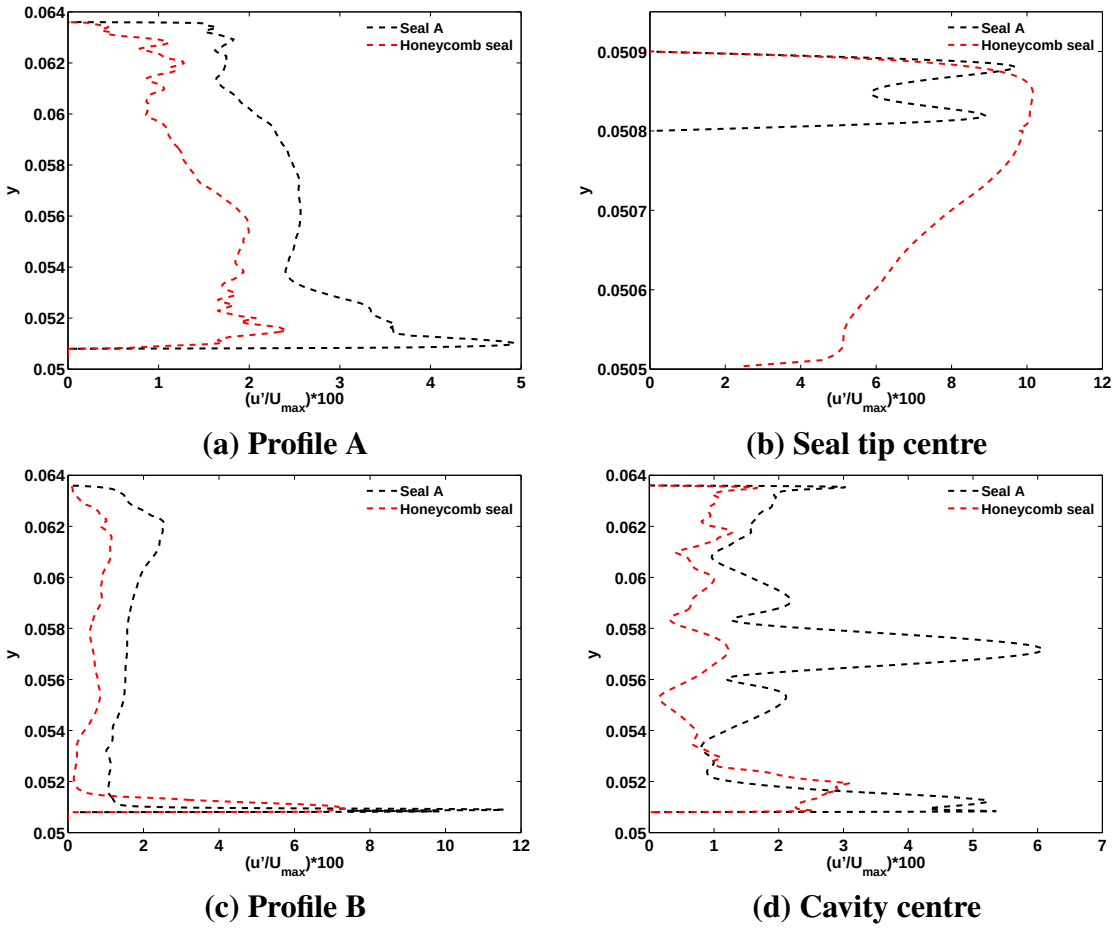

Fig. 6.15 Axial turbulence intensity profiles between Seal A and the honeycomb seal.

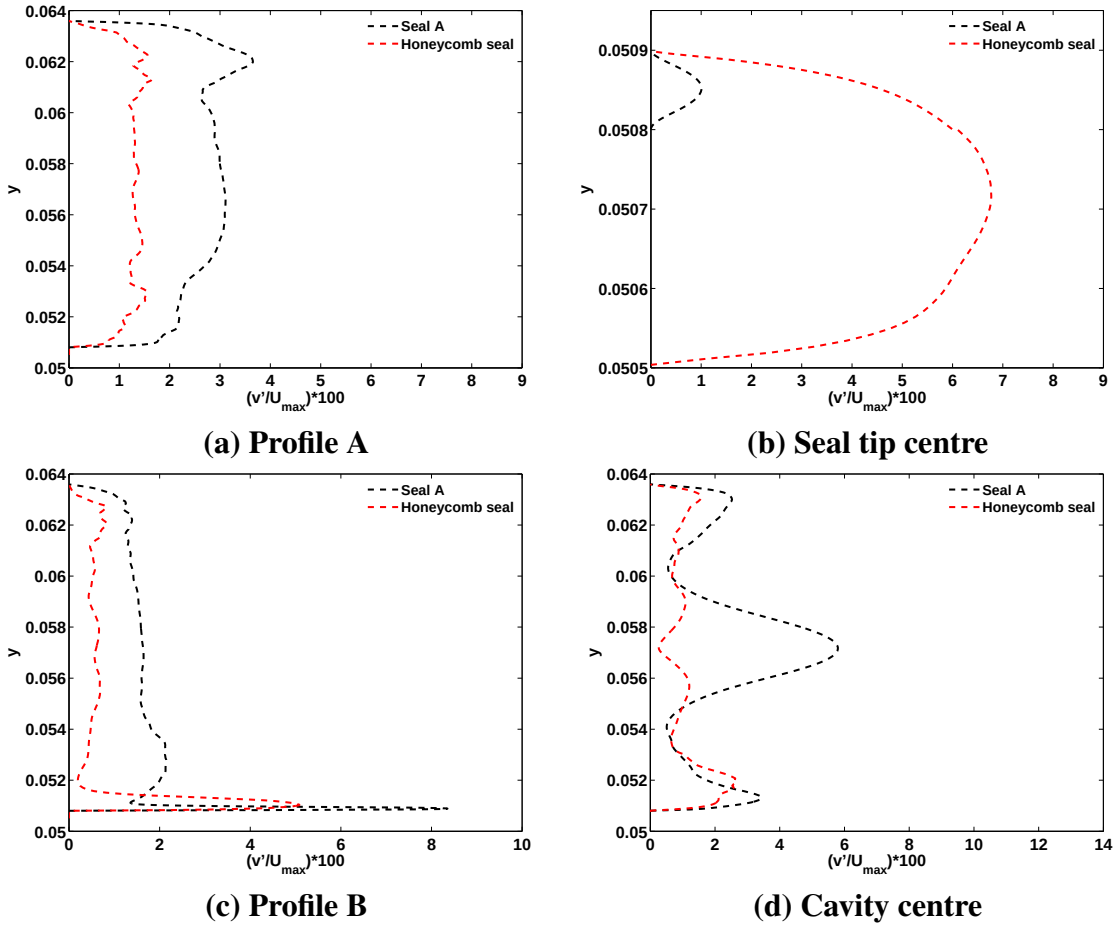

Fig. 6.16 Radial turbulence intensity profiles between Seal *A* and the honeycomb seal.

6.3.3 Size of Shear Layer

As the high velocity fluid exits the seal clearance, a shear layer is formed between the fluid that is carried over to the next constriction and the slower recirculating fluid in the main cavity. Most of the seal performance can be attributed to the action of this shear layer, however, momentum is also transferred to the large recirculations which ultimately are under the viscous effect of the seal walls, providing additional resistance to the flow. Comparison of the size of the shear layer between Seal *A* and the honeycomb seal is presented in Figure 6.17. Here, the shear layer thickness δ_s is expressed as a half width, and is nondimensionalised by the size of the clearance gap. As can be easily seen from Figure 6.17, the size of the shear layer for the honeycomb seal is much thicker than that for Seal *A*. This is consistent with the results shown in Figures 6.6 and 6.10. The axial velocity at the exit is significantly reduced by the effects of the wall shear layers (see Figure 6.14(*b*)).

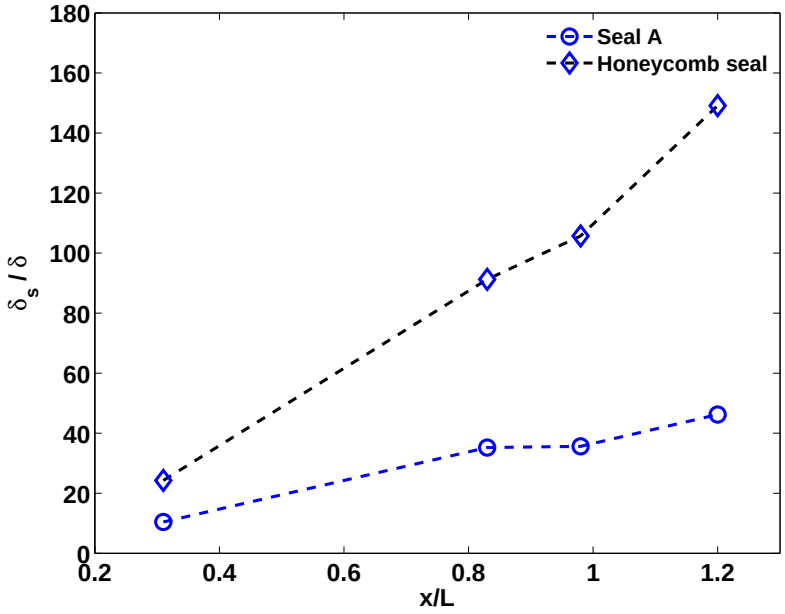

Fig. 6.17 Comparison of shear layer sizes between Seal *A* and the honeycomb seal.

6.3.4 Calculation of Mean Flow Kinetic Energy Carry Over Coefficient

As discussed in the flow field section, a part of the mean flow kinetic energy carries over to the next tooth without recirculation in the cavity. Hodkinson [31] proposed that kinetic energy that is not dissipated in the cavity can be measured by this part of the flow using the carry over coefficient. The carry over coefficient accounts for the turbulent dissipation of

kinetic energy occurring inside each individual cavity. The relationship between the carry over coefficient, γ, and the fraction of kinetic energy carried over into the next cavity, χ, is given by

$$\gamma^2 = \frac{1}{1-\chi} \tag{6.1}$$

when $\gamma = 1$, $\chi = 0$, indicating that all kinetic energy is dissipated in the cavity. Higher carry over coefficient means that a larger portion of the kinetic energy is carried to the next cavity instead of being dissipated. Hence, a higher value of γ indicates that the cavity is less effective in dissipating kinetic energy.

The derivation of Equ (6.1) can be found in Hodkinson [31] as the following:

It is well known that the discharge coefficient increases with clearance. Using Egli's method, the increase expressed by the ratio γ, could also be expressed approximately as $(n_{co}/n_{id})^{1/2}$ which is the ratio of the number of throttlings in the actual labyrinth to the smaller number of throttlings in an ideal labyrinth. Egli plots γ against (δ/s), i.e. the ratio of the clearance δ to the tooth pitch s, and gives the following equation

$$\gamma = \sqrt{\frac{1}{1-\frac{n-1}{n}\times\frac{\delta/s}{\delta/s+0.02}}} \tag{6.2}$$

Hodkinson [31] also pointed out that with uniform design through all stages the pressure drops equal with the exception of the first stage (δ_p/n), which decreased in the proportion $(1-\chi)$. Accordingly the drop through the first stage is increased in the proportion of $l/[l-\chi(n-1)/n]$. As the drop also applies to the square of the velocity, thus $\gamma = 1/[1-\chi(n-1)/n]^{1/2}$ is here adopted. It remains to connect x with the clearance-pitch ratio (δ/s), and a rough attempt was made by Hodkinson [31] as shown in Figure 6.18.

Assuming the stream spreads uniformly at an angle β to a total width $(s+stan\beta)$, and with a part flows straight through with a width s where the energy kinetic is retained, then the energy carry-over fraction χ is $s/(s+stan\beta)$.

This fraction can also be expressed in another way. The kinetic energy at N (say, $K.E.N$) is that due to pressure drop (say, $K.E.\delta_p$) plus the carry-over. The carry-over is the fraction χ multiplied by the kinetic energy at M (say, $K.E.M$). That is,

$$K.E.N = K.E.\delta_p + \chi K.E.M \tag{6.3}$$

If discharges are proportional to square roots of energies, then

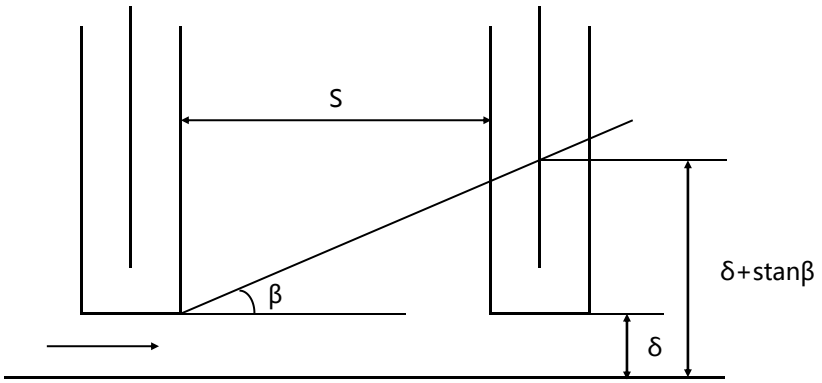

Fig. 6.18 Energy carryover fraction.

$$\gamma^2 = \frac{K.E.M}{K.E.\delta_p} = \frac{1}{\frac{K.E.N}{K.E.M} - \chi} = \frac{1}{1-\chi} \tag{6.4}$$

This with the previous relation gives

$$\gamma^2 - 1 = \frac{\delta}{stan\beta} \tag{6.5}$$

The divergence angle, β, can be measured using the diagram in Figure 6.19. Here, $tan\beta = l1/l2$.

As shown in Figure 6.19, $l1$ is determined by examining the position on the downstream tooth where the radial velocity is zero. Also, $l2$ is the line that connects the lip of the upstream tooth to the point of impingement of the jet onto the downstream tooth, and it is parallel to the lower wall. The kinetic energy carry over coefficient, γ, for Seal A is 1.0537. This means that 90% of mean flow kinetic energy is dissipated in the cavity and 10% is carried over into the next cavity.

The carry over coefficient for the honeycomb seal is calculated as 1.0328. Comparison with the value of the smooth seal, 1.0537, shows that more energy is dissipated in the labyrinth honeycomb seal. As shown in Figures 6.10 and 6.11, like the smooth seal, recirculation also fills the cavity of the honeycomb labyrinth seal and acts as a blockage for the leakage jet. Near the tip, the influence of the honeycomb becomes predominant. For Seal A, a large part of the flow is directly carried over to the next cavity with little dissipation, which reduces the effectiveness of the seal. For the honeycomb seal, fluid flows into the honeycombs. With high turbulence intensity, many vortices are formed that are driven by the viscous shear layer resulting from the honeycomb. This increases perturbations near the tip and hence overall

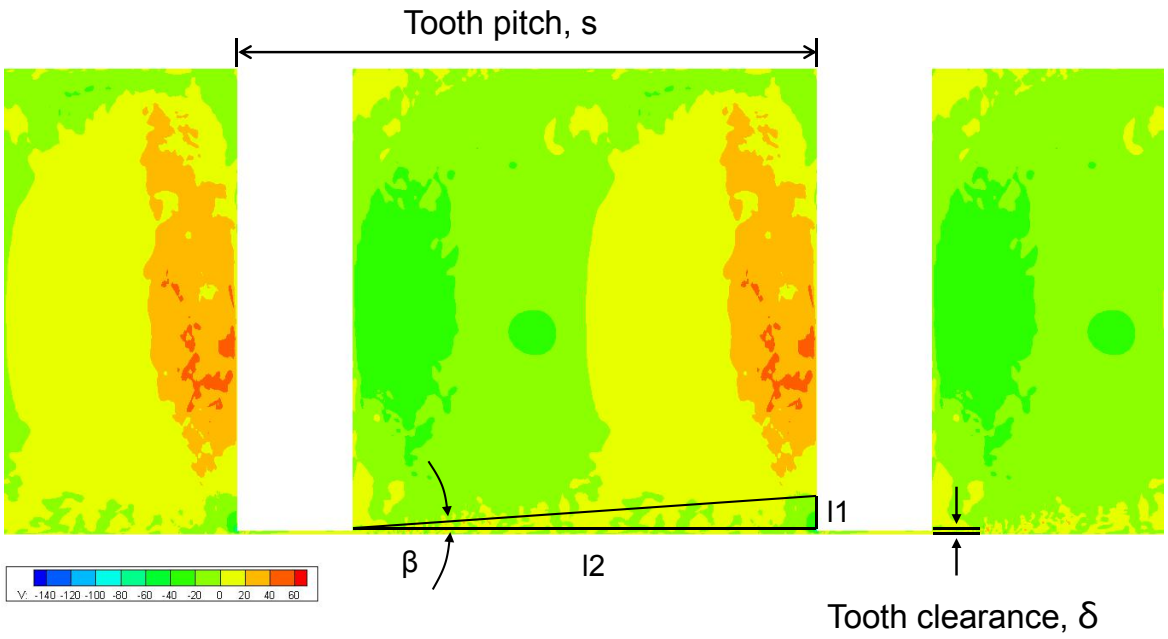

Fig. 6.19 Contour plots of radial velocity and measurement of β.

less energy is carried over in the honeycomb seal. Table 6.1 summarises the main flowfiled parameters between the baseline seal and the honeycomb seal.

Table 6.1 Comparison of the main flowfiled parameters between the baseline seal and the honeycomb seal.

	χ	β (°)	$T.I.$ (%)
Baseline Seal A	1.0537	4.1	8.21
Honeycomb seal	1.0328	6.7	10.94

6.3.5 Calculation of Turbulent Kinetic Energy Budget

From the results obtained from the kinetic energy carry over coefficient, the dissipation value appears to dominate the mean flow mixing process. To help explore the mechanisms in the turbulent mixing process, the turbulent kinetic energy (TKE) budget is also calculated in this study. The TKE budget examines the contribution of different mechanisms such as pressure, diffusion, production and dissipation in the TKE transport equation, providing insight into the flow physics within the labyrinth seals. The TKE budget can be written as:

$$\underbrace{\frac{\partial k}{\partial t}}_{I} + \underbrace{\overline{u_j}\frac{\partial k}{\partial x_j}}_{II} = \underbrace{-\frac{1}{\rho}\frac{\partial \overline{u'_j p'}}{\partial x_i}}_{III} \underbrace{-\frac{1}{2}\frac{\partial \overline{u'_j u'_i u'_i}}{\partial x_i}}_{IV} + \underbrace{\upsilon\frac{\partial k^2}{\partial x_j^2}}_{V} \underbrace{-\overline{u'_i u'_j}\frac{\partial \overline{u'_i}}{\partial x_j}}_{VI} \underbrace{-\upsilon\overline{(\frac{\partial u'_i}{\partial x_j})^2}}_{VII} + \underbrace{\overline{g'_i u'_i}}_{VIII} \tag{6.6}$$

Pressure (III): The first term on the *r.h.s*. represents pressure gradient work by the pressure fluctuations. This term does not produce or dissipates energy, it just re-distributes turbulent kinetic energy in the fluid. Hence it is zero when integrated over a control volume.

Turbulent diffusion (IV): The second term represents transport of turbulent kinetic energy by the turbulent velocity fluctuations.

Molecular diffusion (V): The third term represents viscous diffusion of k, and is negligible at high Reynolds numbers.

Production (VI): The fourth term is positive because the Reynolds stress is usually of opposite sign to the velocity gradient, and hence it represents the production of turbulent kinetic energy by the mean flow gradients. It indicates that the Reynolds stresses act on the mean velocity gradient, extract energy from the mean flow, and feed it to the turbulent velocity fluctuations. Critically in current context this term gives removal of kinetic energy from mean flow.

Dissipation (VII): The fifth term is the dissipation ε, of k, defined as $\varepsilon \equiv 2\upsilon\overline{s'_{ij}s'_{ij}}$. This is also equal to $\upsilon\overline{(\partial u'_i/\partial x'_j)^2}$. This in turn is proportional to the enstrophy, which is dominated by the dissipation scales in turbulent flows.

Body force (VIII): There is no body force added in this study. Thus, this term can be taken as zero.

Overall Balance

In most cases, all terms in Eq. (6.3) have similar orders of magnitude. The turbulent kinetic energy is extracted from the mean flow, and is transported throughout the flow by the mean flow, turbulent transport and pressure fluctuations. The turbulent kinetic energy is diffused by molecular motions with a minor effect and dissipated at small scales by ε.

The TKE budget results for Seal A are presented. To capture the turbulent jet development process, the location at profile B (see Figure 6.13) is selected to extract the TKE budget. As shown in Figure 6.20 (a), production and dissipation are the dominant mechanisms during the turbulent mixing process. At the shear layer region, the turbulent diffusion magnitude is comparable to the production term, but their peaks have the opposite sign. The high value of the turbulent diffusion term results from the higher turbulence generation along the free

shear layers after passing through the seal clearance. The turbulent diffusion term is negative within the shear layers and positive at the cavity zone (y>0.0509). This suggests that the fluctuating kinetic energy is carried from the shear layer by the turbulent diffusion term towards the upper wall region, increasing the viscous dissipation rates at the wall, and hence explaining the more rapid decay of the vortices. The dissipation term at the wall is much larger than the production of fluctuating kinetic energy. The kinetic energy obtained from the flow pressure is also dissipated by the effects of shear stresses along the free shear layers. The dissipation is balanced by the molecular diffusion, which is positive near the lower walls and positive at the cavity zone (y>0.0509). The large amount of energy removed at the walls is mainly due to the effects of the molecular diffusion term, carrying more energy to the walls to be dissipated by ε. The dominant terms are now the viscous dissipation and the molucular diffusion.

The corresponding TKE budget results for the honeycomb seal are shown in Figure 6.20 (*b*). For the baseline seal, the production, diffusion, and convection terms are comparable. For the honeycomb seal, the diffusion terms are larger than the production term. Also, the peak of the convection term is below the centerline axis (y<0.051) and this is consistent with the results of vortex trajectory that indicate the path of the vortices moves downwards as they travel downstream. The dominant term for the honeycomb seal is now the dissipation term, especially near the walls where the viscous dissipation balances the molecular diffusion. The production values appear to be comparatively small compared with the dissipation at this location. This is because turbulence mixing around the tooth-edge is much intense.

6.4 Effects of Optimisation Parameters

As discussed in the optimisation results in Chapter 5, the mass flow coefficient is found to be strongly dependent on geometrical parameters. The effects of individual parameters are masked by the complex interactions of the range of parameters studied. The changes in flow patterns that can be produced by simply altering a single parameter are quite large. The effect of the selected geometrical parameters: groove numbers, sealing clearance, inclination angle, and tooth width on the leakage flow characteristics in the labyrinth seal are investigated in this following section in detail.

6.4.1 Effects of Groove Number and Geometry

From the mass flow coefficient trend shown in Figure 5.9 in Chapter 5, we know that for seals *D* to *F* with grooves, the leakage is much smaller than that of Seal *A*. The results show

(a)

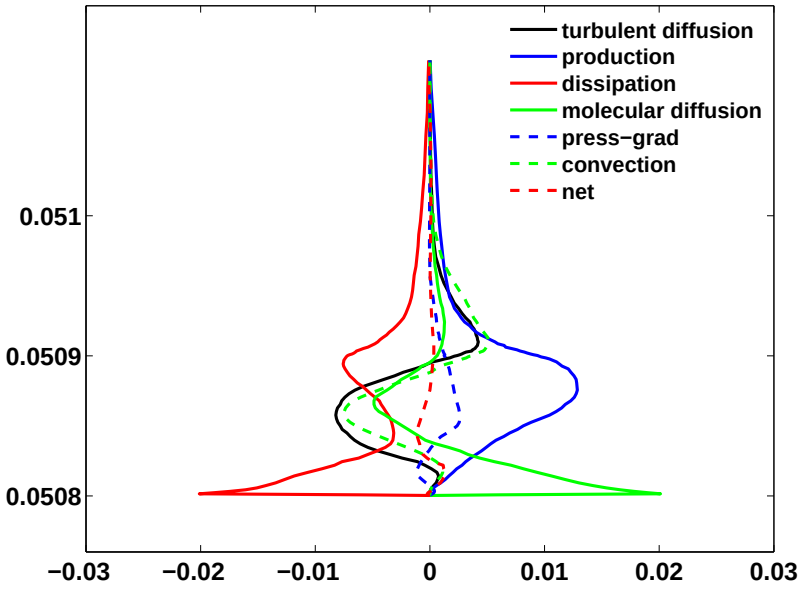

(b)

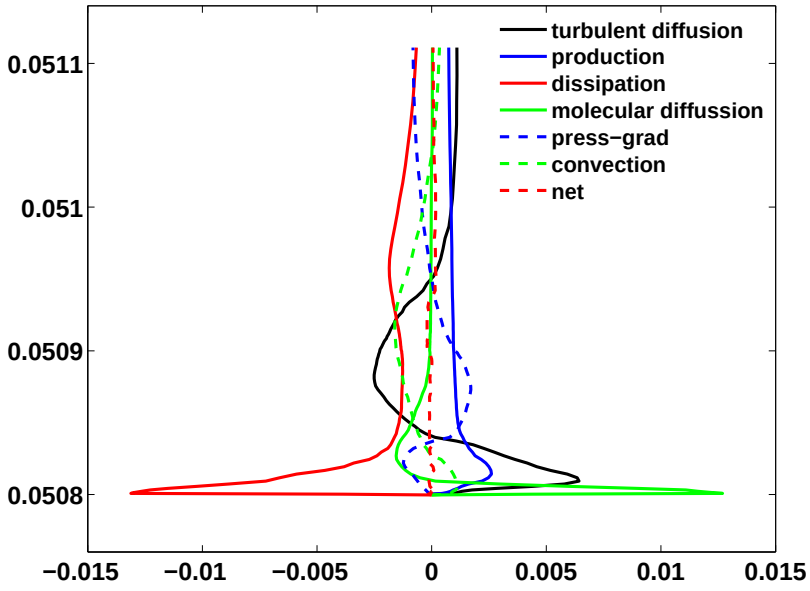

Fig. 6.20 Budget of turbulent kinetic energy along profile *B*.

that the more grooves, the better the leakage performance that can be achieved. Although the large recirculation in the seal cavity for the baseline Seal *A* and seals with grooves look similar, the secondary flow in the labyrinth chamber for seals with grooves is stronger than the baseline Seal *A*.

Figure 6.21 shows the time-averaged vorticity magnitude contours at the seal exit. In Seal *B*, small scale eddies generated near the lower front corner can be seen (indicated by the inset figure), which reduces the flow blockage and length of the seal constriction, and degrading the sealing performance. Similar effects also degrade the performance of Seal *C* further, and are indicated by the inset figures. Figure 6.22 presents the iso-surface based on the *Q*-criteria, coloured by local instantaneous streamwise velocity for the best and worst performing seals *F* and *C*, respectively. The vortices in the recirculations can be seen clearly in the figures. The global recirculation for Seal *F* is more intense than that of Seal *C*.

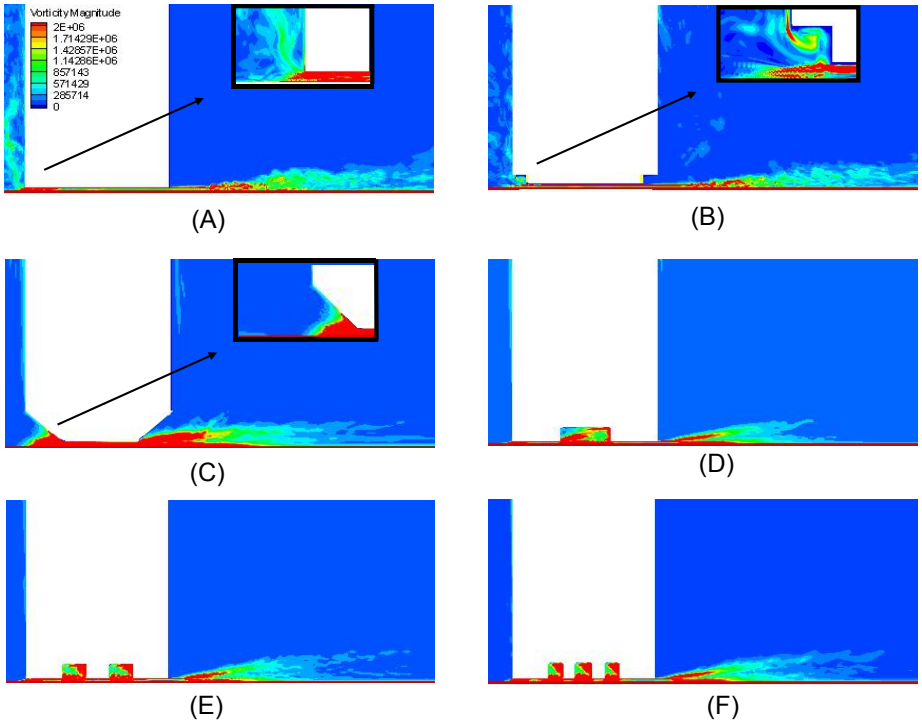

Fig. 6.21 Time-averaged vorticity contours at seal exits.

The velocity profiles are analysed quantitatively along profiles *A* and *B* as presented in Figure 6.23. From the variation of the axial velocity, again the maximum values of the axial velocity are found to be in the shear layer region at the seal gap exit, in the bottom portion of the cavity. The leakage flow decelerates rapidly as the wall jet spreads into the cavity. In the spanwise profile of the streamwise component of velocity, some evidence of a type of

(a)

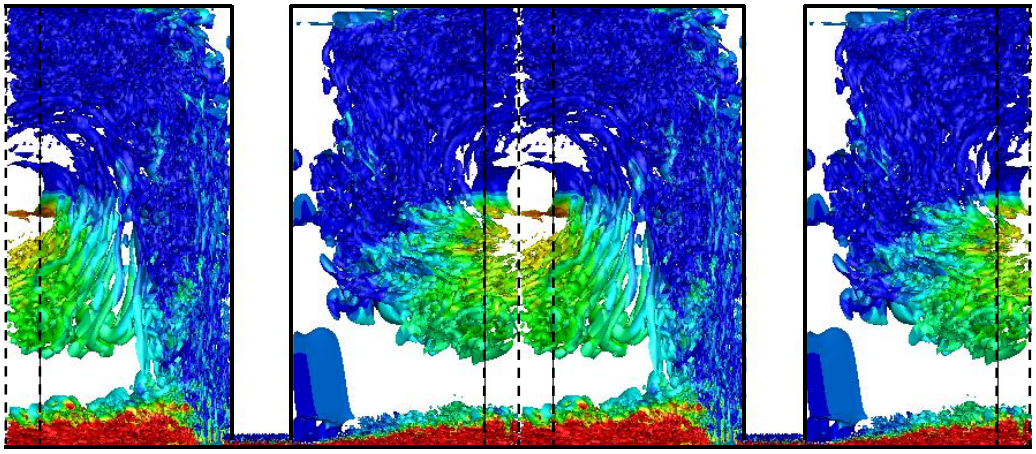

(b)

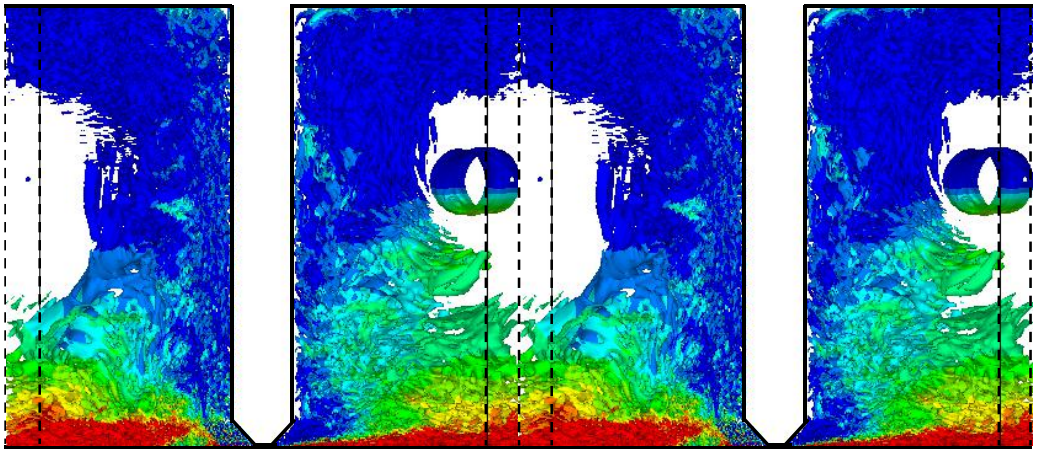

Fig. 6.22 Iso-surface of Q-criterion contours for seals F and C.

jet coalescence can be seen. There are relatively small deviations between different cases as shown in Profile *B*. There is no obvious evidence of the seal affecting the axial velocity, whereas there is a clear impact on the turbulent Reynolds stresses. Larger differences in $\overline{v'v'}$ and $\overline{u'v'}$ can be seen clearly in the figures. This is similar to the development of laminar shear layers, which are known to transition violently. For $\overline{v'v'}$ in Profile *A*, it appears that the curves start to split into two different families: Seals *A* to *D*, and seals *E* and *F*. Seals *E* and *F* tend to have a smaller core region with relatively smaller values for $\overline{v'v'}$ while Seals *A* to *D* have stronger near wall gradients. Similar effects occur around the downstream Profile *B*. Figure 6.23 also shows the turbulent Reynolds stresses. For $\overline{u'v'}$, the profiles for all configurations are quite consistent except for some negative values shown for Seal *C*.

6.4.2 Effects of Clearance Size

Hodkinson [31] suggested that, as would be expected, clearance is one of the major parameters that affects the mass flow coefficient. The results show that keeping the other parameters constant, the mass flow coefficient increases with the increase of tooth clearance. Therefore, the sealing performance is better with smaller clearance. In this study, the results of six typical seal geometries from three pairs are compared in order to better understand the sole effect of clearance. They are *S*6_22 *S*7_29, *S*6_9 *S*7_30, *S*4_8, and *S*8_23, respectively. Here, *S*6_22 represents the 22^{nd} population in the 6^{th} generation. The five geometrical parameters of these typical seals are compared in Table 6.2. We can see from the table that, except for the clearance size, the other parameters for each selected pair are nearly the same.

Table 6.2 The variable parameters of the three selected pairs of seals.

	Seal	$\delta(mm)$	$\theta(^\circ)$	$L(mm)$	$l(mm)$	n	f
Pair 1	S6_22	0.08414	16.88	3.7948	0.5554	7	0.1799
	S7_29	0.08002	16.85	3.7919	0.5614	7	0.1643
Pair 2	S6_9	0.08596	16.67	3.7792	0.4398	8	0.1852
	S7_30	0.08196	16.67	3.7791	0.4556	8	0.1723
Pair 3	S4_8	0.09280	15.12	3.7930	0.5528	7	0.1916
	S8_23	0.08000	15.28	3.7985	0.5537	7	0.1622

The corresponding mass flow results are compared in Figure 6.24. Here, the axial Reynolds number Re_a is defined as $\rho U_{max}\delta/\mu$, where U_{max} represents the maximum axial velocity through the seal, δ represents the seal clearance. Thus, the effect of clearance size can be represented using the axial Reynolds number. As can be seen from Figure 6.24, the mass flow coefficient decreases with the reduction of the clearance size, improving the

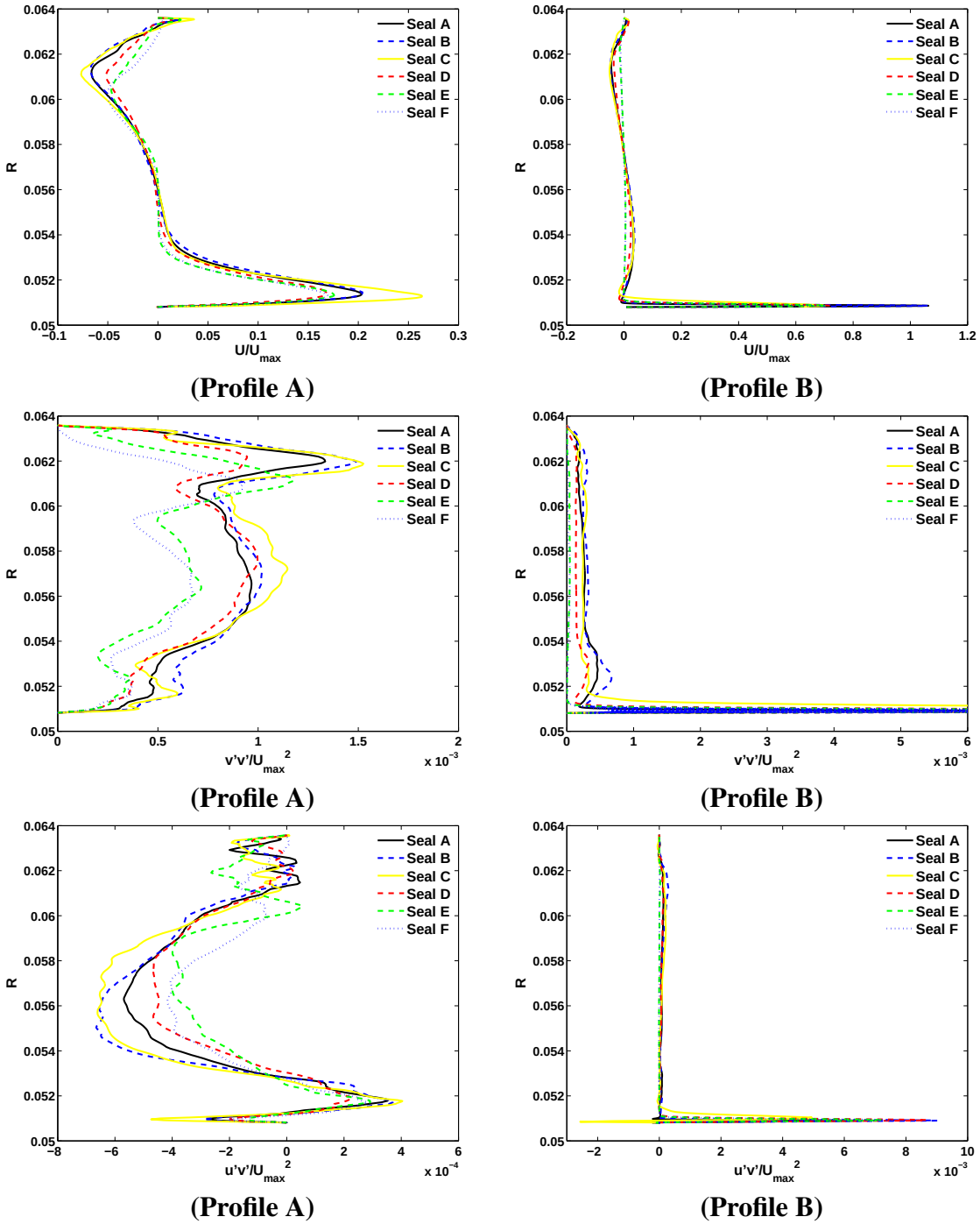

Fig. 6.23 Axial velocity, radial turbulence intensity and shear stress profiles.

sealing effectiveness of the labyrinth seal. The corresponding reason is analysed through studying the velocities extracted along profiles *A* and *B*. Comparisons were made between the selected three pairs. The decrease in the seal clearances causes a slight decrease in the axial velocity (see Figure B.1 in Appendix B). In addition, Rhode and Guidry [80] showed that the turbulence effect in the shear layer is also increased by the decreasing clearance size. Figure 6.25 shows the turbulence intensity between seals with different clearances in this study. Here, the turbulence intensity is the averaged value taken from the shear layer. The results are consistent with Rhode and Guidry [80].

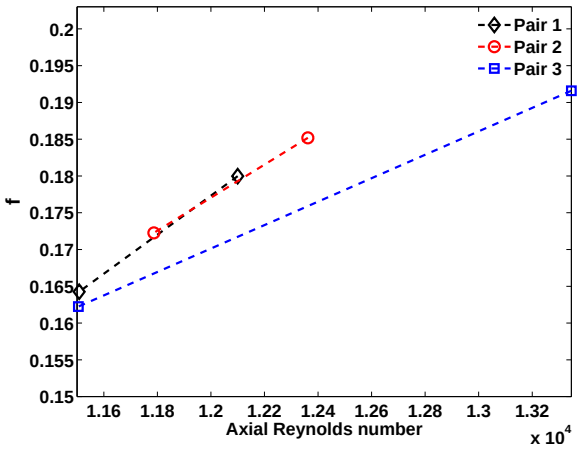

Fig. 6.24 Mass flow results between seals with different clearances.

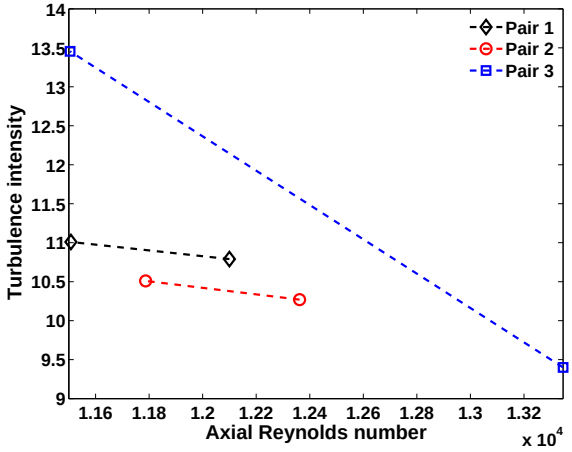

Fig. 6.25 Turbulence intensity between seals with different clearances.

Although beneficial in practical engineering, there is little room to reduce the clearance δ in order to guarantee the safe operation of equipment, as the clearance still has a lower limit to keep the labyrinth seal surfaces from touching each other.

6.4.3 Effects of Tooth Width

In the study of Gamal and Vance [27], doubling the thickness of the blades reduced the leakage rates by up to 20% for certain test configurations. Thus, one pair of seals with different tooth widths (*S*5_11 and *S*4_5) in this study are selected to investigate the effect of tooth width. The variable parameters are shown in Table 6.3. The blades initially had a thickness of 3.175 mm.

Compared to *S*4_5, the carry over coefficient of *S*5_11 decreases by a factor of 1.01 when the tooth width is increased by a factor of 14%. Since the pitch was kept the same, the distance between two adjacent teeth is smaller with a larger tooth width (with 10% changes). The shear layer (expressed as a half width) of *S*5_11 is also thicker (see Figure

Table 6.3 The variable parameters of the selected pair of seals.

Seal	$L(mm)$	$\theta(^\circ)$	$\delta(mm)$	$l(mm)$	n	f
S5_11	3.804	13.68	0.08723	0.5524	7	0.176
S4_5	3.3324	13.60	0.08700	0.4783	7	0.191

6.26), which means *S*5_11 generated a stronger wall bounded jet. As a result, the fluid particle impinges on a higher point of the downstream tooth wall enhancing the circulation in the vortex. Therefore, a smaller portion of the flow is carried over to the next cavity. Figures 6.27 and 6.28 present streamlines and axial velocity contours for seals *S*5_11 and *S*4_5. The recirculation at the seal tip is longer for *S*4_5.

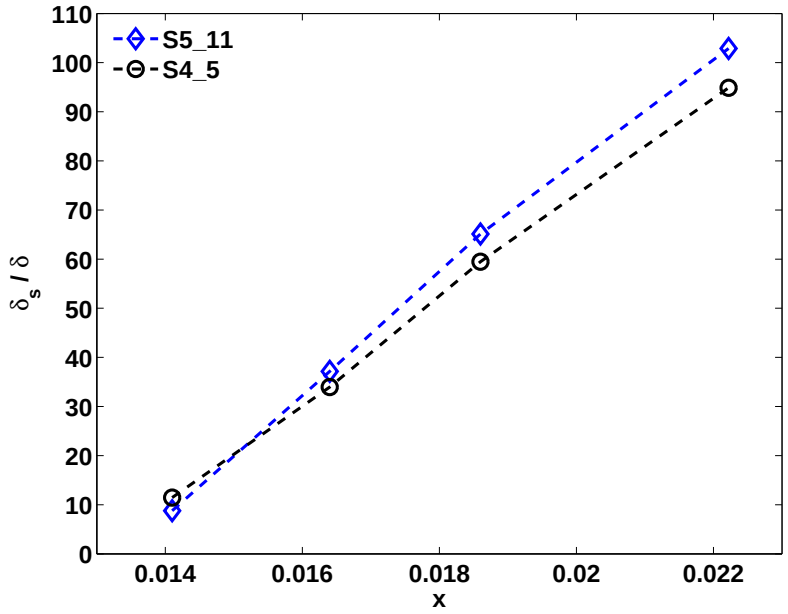

Fig. 6.26 Comparison of shear layer thickness between *S*5_11 and *S*4_5.

6.5 Final Design

6.5.1 Optimised Seal Combined with Honeycomb

As shown in the previous results, the optimised labyrinth seal and a seal with honeycomb both provide better leakage performance. Here, a new configuration has been generated, which combines the advantages of *GA* and honeycomb. The corresponding layouts are shown in Figures 6.29 and 6.30.

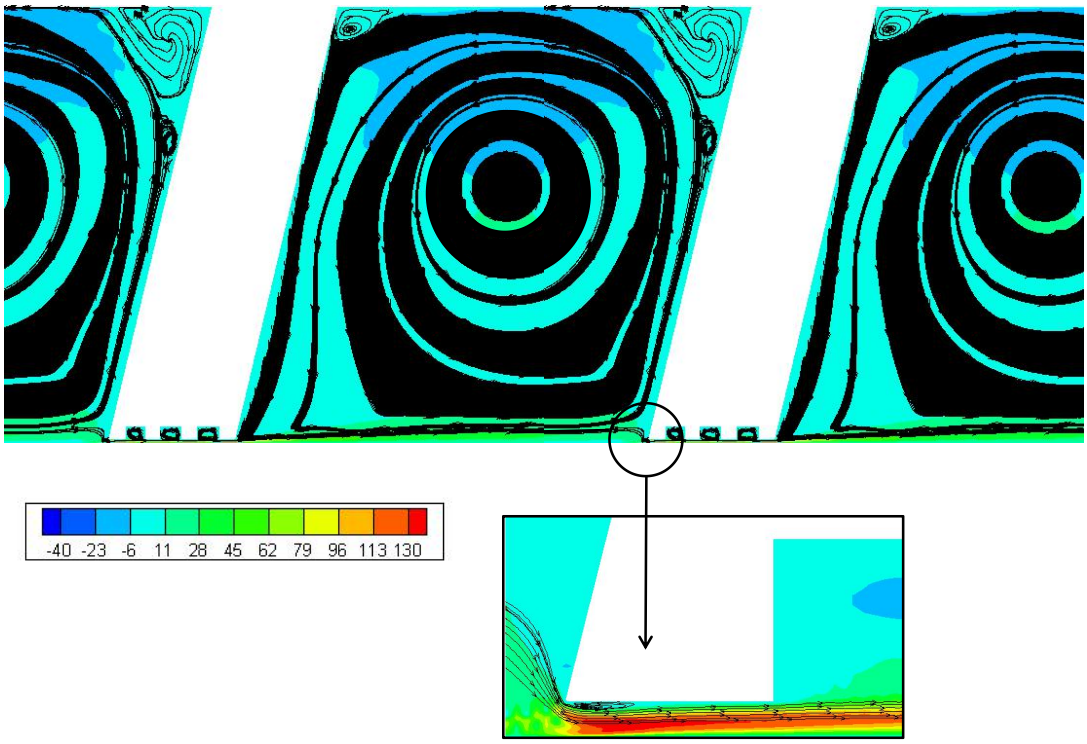

Fig. 6.27 Periodic streamlines, seal tip recirculation and axial velocity contours of *S*5_11.

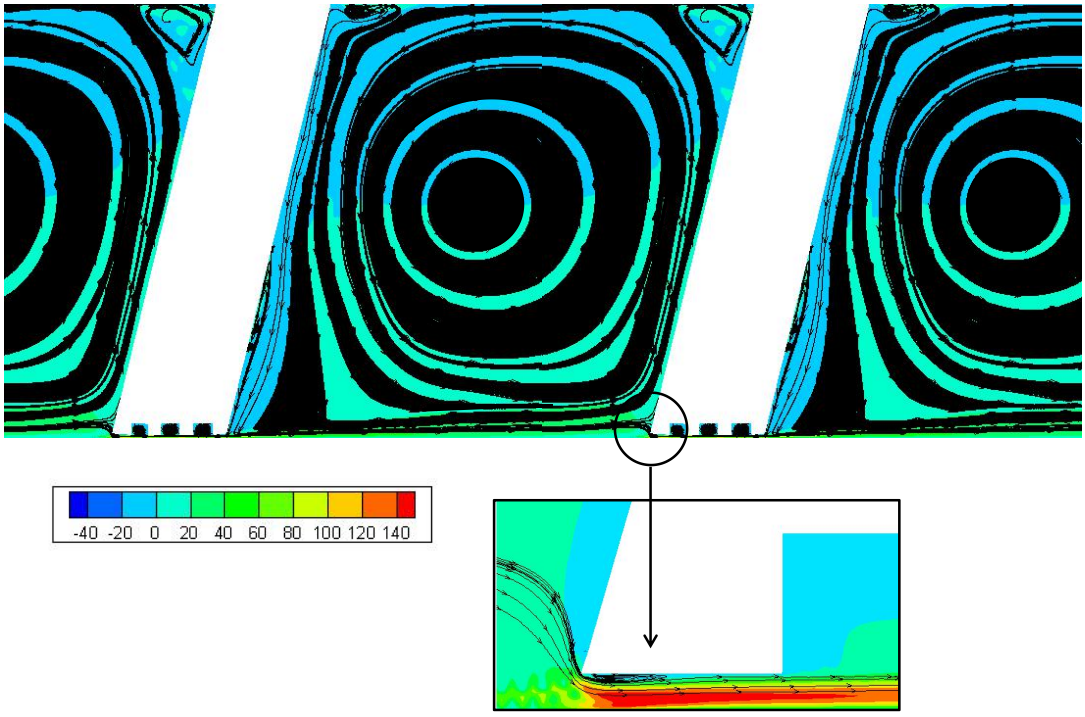

Fig. 6.28 Periodic streamlines, seal tip recirculation and axial velocity contours of *S*4_5.

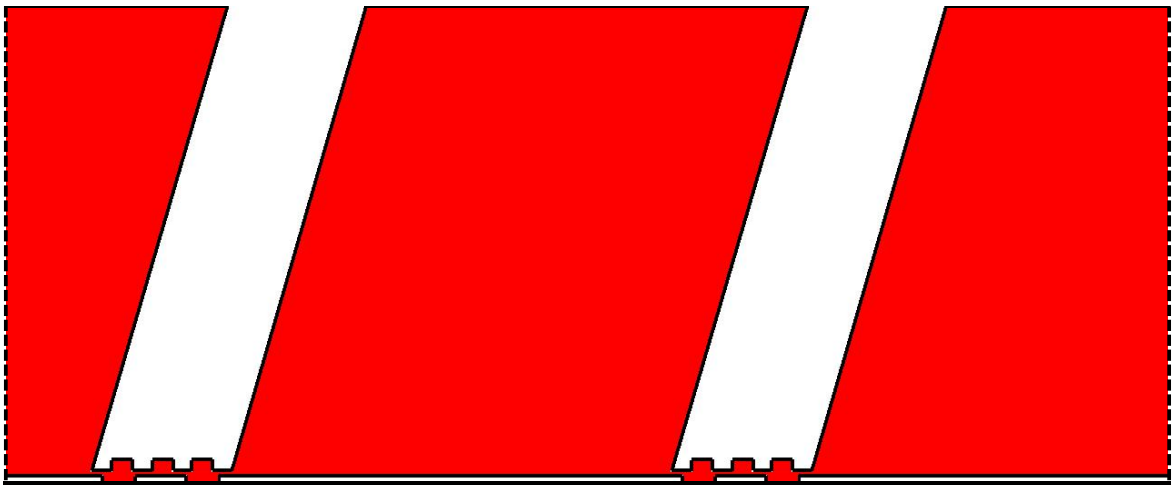

Fig. 6.29 Layout combined with the optimised design and honeycomb seal (mid x–y plane).

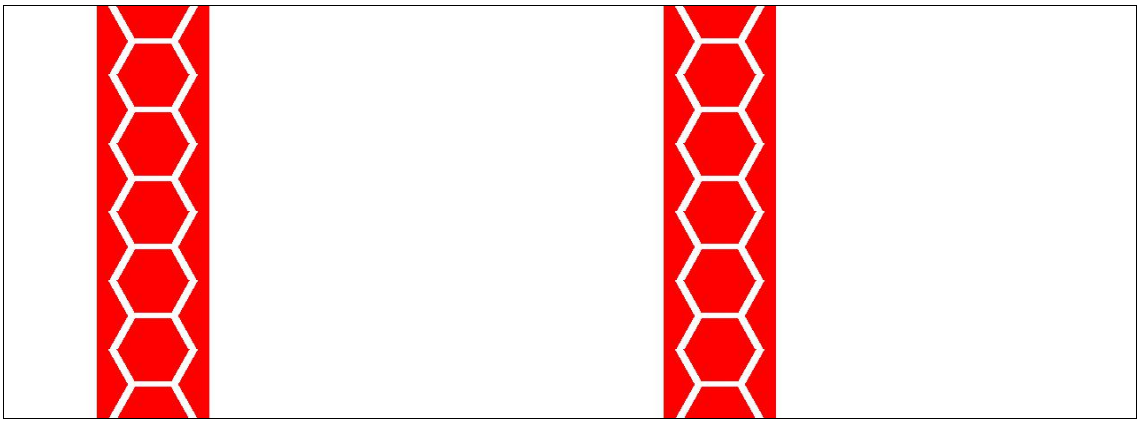

Fig. 6.30 Layout combined with the optimised design and honeycomb seal (mid x–z plane).

6.5.2 Flow Fields

The streamlines and axial velocity contours on the mid-plane of this final configuration are presented in Figure 6.31. A similar process as that of a straight seal can be observed, i.e. large recirculations are formed inside the cavity. With the inclination angle, three vortices are generated near the upper front corner of the tooth (see zone *A*). The carry over coefficient for the final design was 1.0242, which means 95.4% of mean flow kinetic energy is dissipated in the cavity and 4.6% is carried over into the next cavity.

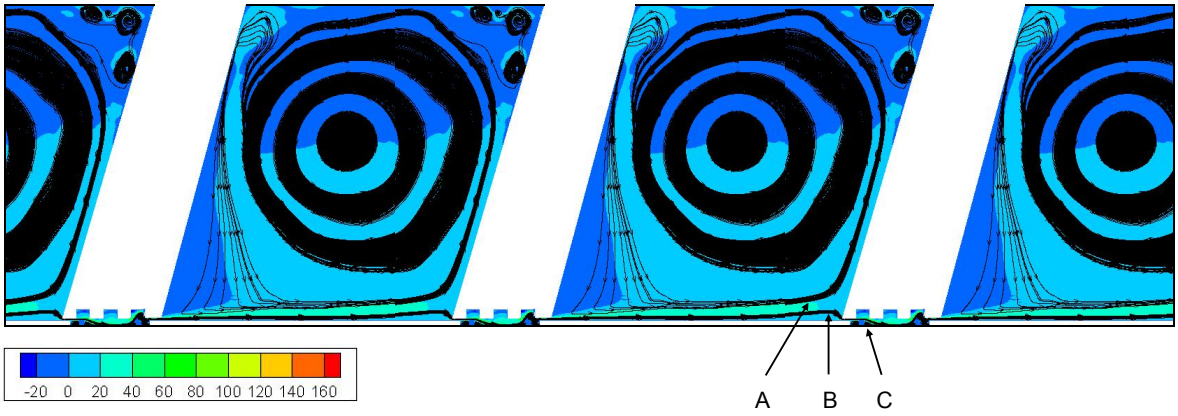

Fig. 6.31 Periodic streamlines and axial velocity contours of the final configuration.

Instantaneous and time-averaged vorticity magnitude contours for this final configuration are presented in Figures 6.32 and 6.33. The flow then begins to reaccelerate, with vortices becoming stretched near the upper part of the seal clearance, generating large recirculations. For the baseline Seal *A*, the recirculation vortex fills the whole cavity (see Figure 6.6). The counter-rotating recirculation zone in this final configuration is deflected towards the next tooth and the bottom of the labyrinth cavity.

Table 6.4 compares the main flowfield parameters between the baseline seal, honeycomb seal, optimised design and the final design. As expected, the final design takes advantages of both the optimised design and the honeycomb seal. As a result, the leakage can be reduced up to 30.6% relative to the baseline Seal *A*.

6.6 Conclusions

In labyrinth seals, highly unstable shear layers are generated after passing through the seal clearance. With the use of *LES*, the important flow physics responsible for the sealing mechanism can be captured. The results show that the sealing mechanism of the flow through labyrinth seals is associated with turbulent mixing and shear which predominantly occur in

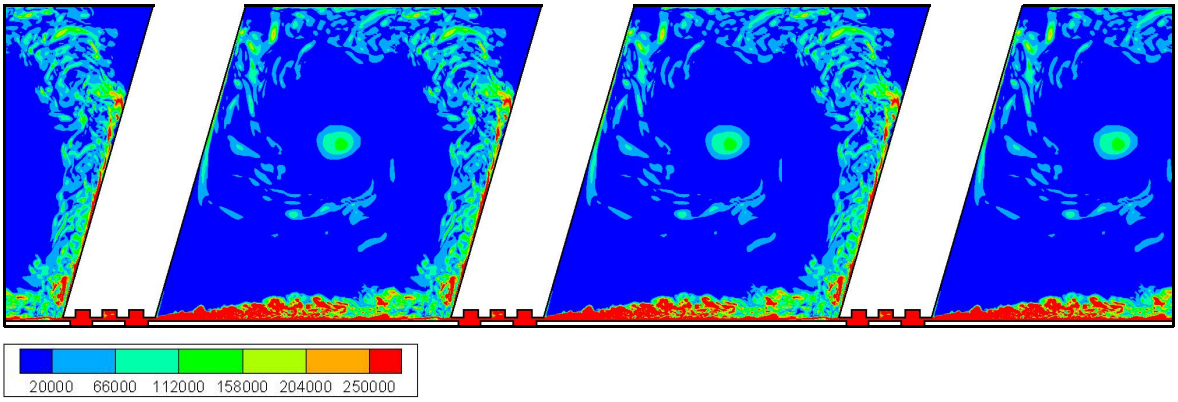

Fig. 6.32 Instantaneous vorticity magnitude contours of the final design.

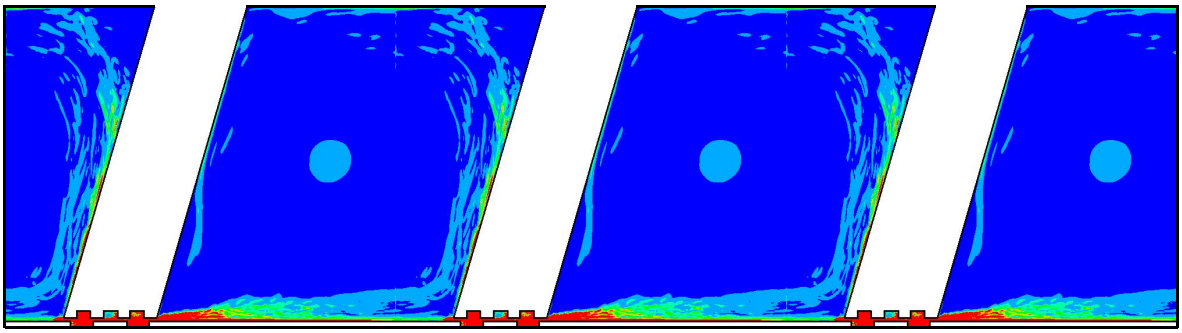

Fig. 6.33 Time-averaged vorticity magnitude contours of the final design.

Table 6.4 Comparison of the main flowfiled parameters.

	Carry over coefficient (χ)	Mass flow results (f)
Baseline Seal A	1.0537	0.224
Honeycomb seal	1.0328	0.215
Optimised design	1.0426	0.167
Final design	1.0242	0.155

the vicinity of the tooth edge, and to a lesser extent after passing through the seal clearance. The mixing of the leakage jet and main flow alters significantly the flow angle at the clearance exit.

For the first time, the turbulent kinetic energy budget was applied in the labyrinth seal study. The production and dissipation terms were found to dominate the kinetic energy equation. There are also significant contributions by the diffusion and convection terms. The turbulent diffusion magnitude is comparable to the production term at the shear layer region. The high value of the turbulent diffusion term has resulted from the higher turbulence generation along the free shear layers after passing through the seal clearance. This process increases the viscous dissipation rates at the wall, hence explaining the more rapid decay of the vortices. The kinetic energy obtained from the flow pressure is also dissipated by the effects of shear stresses along the free shear layers. The results from the TKE budget are consistent with the flow physics obtained from LES, and provide deeper insight into the loss mechanisms during the turbulent mixing process. The advantages of the TKE budgets should be taken and be used to improve the *RANS* model.

The flow structure and mass flow rate results for the baseline Seal A and honeycomb seal have been presented and analysed in detail. Compared to the baseline Seal A, the mass flow rate was reduced by about 4% in the honeycomb seal. This is consistent with the kinetic energy carry over coefficient results. The carry over coefficient for the honeycomb seal was 1.0328 lower than the baseline seal 1.0537, indicating better energy dissipation inside the cavity. As a result, the flow that is carried over into the next cavity is reduced. The mean and turbulent fluctuations in the flow field were measured. As can be expected, the honeycomb seal had higher turbulence intensity, with many more vortices driven by the viscous shear layer resulting from the specific hexagon structure of the honeycomb cell surface.

Additionally, the effect of the parameters used in the optimisation process were analysed. The optimised design from Chapter 5 was then combined with the honeycomb seals, and a reduction of 30.6% of the mass flow rate can be achieved compared to the baseline Seal A.

Chapter 7

Conclusions and Future Work

This thesis focuses on improving the heat transfer performance of internal cooling passages and sealing performance of labyrinth seals. The *CFD* solver, *NEAT*, is described in detail in Chapter 3. As given in the literature review in Chapter 2, it is widely accepted that, *RANS* models are poor at predicting flow and heat transfer in complex geometries with separated flow. Thus *LES* is used to model the complex flows in this study. A mixed nonlinear *SGS* model has been employed in all the simulations for its ability to better capture some of the more complex aspects of the turbulent cascade, like wall and highly strained flows. Equipped with this more capable *LES* solver, the next step is to demonstrate that there are cheaper approaches that can be combined with *LES* to make mesh generation easier, as multiple geometries will be involved in the optimisation design process. The immersed boundary method (*IBM*) is chosen due to its advantage of using a simple Cartesian grid to model the complex geometries of ribs and labyrinth seals. It can further reduce the effort of grid generation and save the computational cost of using *LES*. Three benchmark cases using the *IBM* were validated in Chapter 4.

7.1 Internal Cooling Passages

The square case in the ribbed channel was first carried out to validate the accuracy of this *LES* model. Through the velocity field and heat transfer results, *LES* was found to be able to predict the velocity distribution with good accuracy and to obtain the correct Nusselt number trend within 5% discrepancy. It shows that the structural solver can not only generate the mesh efficiently, but can also help to model the turbulence accurately. The flow and temperature field were examined to better understand the essential features of the complex turbulent flow caused by the rib turbulators.

The thermal characteristics in terms of heat transfer and friction factor of ten different rib shapes have also been investigated: square, perforated, triangular with increasing height in the flow direction, triangular with decreasing height in the flow direction, pentagonal with increasing height in the flow direction, pentagonal with decreasing height in the flow direction, house-shaped, groove-shaped, semi-circular and an arc profile. The formation of a large recirculation bubble was observed for all cases downstream of the rib. Moreover, to better appreciate the flow physics, the two-point correlation coefficients were also calculated. The triangular rib with increasing height in the flow direction, with the largest recirculation bubble and the largest integral length scale, was found to provide the best heat transfer performance with 5% more than the basic square rib. The results also showed that rounded-corners deteriorated the heat transfer performance.

7.2 Labyrinth Seals

The main objective of this study is to investigate the effects of geometry on leakage performance, and to find the optimal seal geometry with the best sealing performance. The use of *LES* for large scale design has become within the reach of modern computational systems recently. With careful selection of the optimisation algorithm, such as the genetic algorithm shown here, significant design improvements can be achieved within relatively short time. *LES* was developed in combination with *IBM* in the study of internal cooling passages, leading to an improved performance. Finally, these advances were combined into an optimisation framework to improve the sealing performance of labyrinth seals.

Three hundred different labyrinth seal geometries were generated using the genetic algorithm, reliant on the selected geometrical parameters and manufacturing constraints. Geometries were generated in sets, representing a population for each evolutionary generation. A hundred individuals were stochastically generated to form the populations of the first generation. By making use of the large number of populations, the design space allowed much faster calculation of the approximate objective function. The range of geometries is represented using an *IBM* on a background Cartesian grid, avoiding the need to laboriously mesh by hand, or to trust in automatic meshing software. As a further benefit, the computational cost of each of the individual simulations could be reduced by the use of this efficient structured solver. Taking the number of simulations into consideration, this good performance of *IBM* translated into considerable savings in computational time. This approach also applied a parallel optimisation heuristic by carrying out several jobs simultaneously.

The combination of *GA* with *LES* proved to be effective, with the best performing seal producing significantly better sealing performance (27.6%) than the baseline seal. The

optimised design consisted of a seal inclined towards the flow direction with grooves at its tip. The honeycomb labyrinth seal was also taken into consideration in this study. Compared to the baseline Seal *A*, a reduction of 4% in the mass flow rate was achieved in the honeycomb seal. This is consistent with the kinetic energy carryover coefficient results. The carryover coefficient for the honeycomb seal was 1.0328 which is lower than the baseline seal 1.0537, indicating better energy dissipation inside the cavity. As a result, the flow that is carried over into the next cavity is reduced. The optimised design was then combined with the honeycomb seals, and a total reduction of 30.6% of the mass flow rate was achieved compared to the baseline Seal *A*.

In labyrinth seals, highly unstable shear layers are generated after passing through the seal clearance. Using *LES*, the important flow physics responsible for the sealing mechanism can be captured. The results showed that the sealing mechanism of the flow through labyrinth seals was associated with turbulent mixing and shear which predominantly occur in the vicinity of the tooth edge, and to a lesser extent after passing through the seal clearance. The mixing of the leakage jet and main flow alters significantly the flow angle at the clearance exit. For the first time, the turbulent kinetic energy budget was applied in the labyrinth seal study. The production and dissipation terms were found to dominate the kinetic energy equation. The results from the *TKE* budget were consistent with the flow physics obtained from *LES*, and provided deeper insight into the loss mechanisms during the turbulent mixing process. The advantages should be taken and can also be used to improve the *RANS* model for the seals studies.

7.3 Recommendations for Future Work

The accuracy of *LES* at prediction of the complex flows in internal cooling passages and labyrinth seals has been proved. *IBM* has also been shown to be a useful tool for rapid calculation of complex geometries. Thus, it would be advantageous to combine the performance gains from these two approaches, and extend the benefits to other critical components of the engines in future research. Engine areas which have highly unsteady or separation flow regions may be suitable. Potential candidates include impinging wake flows behind blade rows, or unsteady flows leaving the combustion chamber.

The potential inherent in combining the low cost of *IBM* with the perfect parallelisation of *GA*s has been shown here for the labyrinth seal case. It is expected that this type of automatic optimisation design will be used in the design process of other engine parts, particularly for flows with strong parameter interactions. For example, in this study the research effort for the ribbed channel focused on geometry with sharp edges, e.g., triangular,

square, pentagonal. Further study could be extended using rib turbulators with more realistic geometries, such as rounded corners and rib inclination angles, which would produce certain effects on the heat transfer performance. In addition, rib inclination angles could be further used to combine with rib geometries, and could be potentially very complex. Thus, the optimisation design should be continued to pursue the best heat transfer performance in the internal cooling passages. It would also be interesting to further test the performance of different population-based metaheuristics, for example, a more advanced optimisation algorithm could be explored. Since the *GA* has been shown to perform well for the labyrinth seals here, it is entirely possible that more advanced methods could considerably enhance the performance of the optimiser.

For the first time, the turbulent kinetic energy (TKE) budget was used to analyse the sealing mechanisms. Future work on the labyrinth seal case should take advantage of the deeper insight gained with *LES*, and calculate the TKE budget in more complex labyrinth seals, such as the honeycomb labyrinth seals. Moreover, the complex phenomenon of an air-cooled turbine blade involves the interaction of hydrodynamics, heat transfer, and stresses in solids. Demirdžić and Muzaferija [19] employed the stress analysis to solve some thermo-elastic problems, and Demirdžić and Martinović [18] further extended this method to thermo-elasto-plastic solid body problems. Therefore, the stress field in the labyrinth seal could also be considered and computed in the future.

References

[1] Acharya, S., Dutta, S., Myrum, T., and Baker, R. (1993). Periodically developed flow and heat transfer in a ribbed duct. *International Journal of Heat and Mass Transfer*, 36(8):2069–2082.

[2] Ahn, J., Choi, H., and Lee, J. S. (2004). Large eddy simulation of flow and heat transfer in a channel roughened by square or semicircle ribs. In *ASME Turbo Expo 2004: Power for Land, Sea, and Air*, pages 411–418. American Society of Mechanical Engineers.

[3] Ahn, S. (2001). The effects of roughness types on friction factors and heat transfer in roughened rectangular duct. *International Communications in Heat and Mass Transfer*, 28(7):933–942.

[4] Amano, R. and Goel, P. (1995). Computation of turbulent flow beyond backward steps using reynolds stress closure. *AIAA J*, 23:1356–1361.

[5] Asok, S., Sankaranarayanasamy, K., Sundararajan, T., Rajesh, K., and Ganeshan, G. S. (2007). Neural network and cfd-based optimisation of square cavity and curved cavity static labyrinth seals. *Tribology International*, 40(7):1204–1216.

[6] Back, T., Hammel, U., and Schwefel, H.-P. (1997). Evolutionary computation: Comments on the history and current state. *IEEE transactions on Evolutionary Computation*, 1(1):3–17.

[7] Benvenuti, E. and Tomasini, E. (1979). Analytical and experimental development of labyrinth seals for process centrifugal compressors. *Performance prediction of centrifugal pumps and compressors*, pages 273–285.

[8] Bergman, T. L. and Incropera, F. P. (1996). *Introduction to heat transfer*. John Wiley & Sons.

[9] Bradshaw, P. (1997). Understanding and prediction of turbulent flow—1996. *International journal of heat and fluid flow*, 18(1):45–54.

[10] Chan, Y., Buggeln, R., and McDonald, H. (1987). 3-d dynamic labyrinth seal analysis aero propulsion laboratory. air force wright aeronautical laboratories. Technical report, AFWAL-TR-87-2009.

[11] Chandra, P. R., Fontenot, M. L., and Han, J.-C. (1998). Effect of rib profiles on turbulent channel flow heat transfer. *Journal of thermophysics and heat transfer*, 12(1):116–118.

[12] Childs, D., Elrod, D., and Hale, K. (1989). Annular honeycomb seals: Test results for leakage and rotordynamic coefficients; comparisons to labyrinth and smooth configurations. *Journal of Tribology*, 111(2):293–300.

[13] Childs, D. W. and Vance, J. M. (1997). Annular gas seals and rotordynamics of compressors and turbines. In *Proceedings of the 26th Turbomachinery Symposium*, pages 201–220.

[14] Cho, H. H., Wu, S. J., and Kim, W. S. (1998). A study on heat transfer characteristics in a rib-roughened rectangular duct. In *Proc. of 11th Int. Symp. on Transport Phenomena*, pages 364–369.

[15] Chung, H., Lee, G., Nine, M., Bae, K., and Jeong, H. (2014). Study on the thermal and flow characteristics on the periodically arranged semi-circular ribs in a rectangular channel. *Experimental Heat Transfer*, 27(1):56–71.

[16] Davis, R. L. and Dannenhoffer, I. J. F. (1994). Three-dimensional adaptive grid-embedding euler technique. *AIAA journal*, 32(6):1167–1174.

[17] Demirdžić, I., Lilek, Ž., and Perić, M. (1992). Fluid flow and heat transfer test problems for non-orthogonal grids: Bench-mark solutions. *International Journal for Numerical Methods in Fluids*, 15(3):329–354.

[18] Demirdžić, I. and Martinović, D. (1993). Finite volume method for thermo-elasto-plastic stress analysis. *Computer Methods in Applied Mechanics and Engineering*, 109(3):331–349.

[19] Demirdžić, I. and Muzaferija, S. (1994). Finite volume method for stress analysis in complex domains. *International Journal for Numerical Methods in Engineering*, 37(21):3751–3766.

[20] Denecke, J., Dullenkopf, K., Wittig, S., and Bauer, H.-J. (2005). Experimental investigation of the total temperature increase and swirl development in rotating labyrinth seals. In *ASME Turbo Expo 2005: Power for Land, Sea, and Air*, pages 1161–1171. American Society of Mechanical Engineers.

[21] Domaradzki, J. and Holm, D. D. (2001). Navier-stokes-alpha model: Les equations with nonlinear dispersion. *arXiv preprint nlin/0103036*.

[22] Driver, D. M. and Seegmiller, H. L. (1985). Features of a reattaching turbulent shear layer in divergent channelflow. *AIAA journal*, 23(2):163–171.

[23] Dubief, Y. and Delcayre, F. (2000). On coherent-vortex identification in turbulence. *Journal of turbulence*, 1(1):011–011.

[24] Fasheh, J. (1972). Review and summary of labyrinth seal theory and design. *TMR Report*, pages 2115–3351.

[25] Floyd, C. (1986). Gas seals for rotating shafts. *Tribology international*, 19(4):204–211.

[26] Fransen, R., Gourdain, N., and Gicquel, L. Y. (2012). Steady and unsteady modeling for heat transfer predictions of high pressure turbine blade internal cooling. In *ASME Turbo Expo 2012: Turbine Technical Conference and Exposition*, pages 563–572. American Society of Mechanical Engineers.

[27] Gamal, A. J. and Vance, J. M. (2008). Labyrinth seal leakage tests: tooth profile, tooth thickness, and eccentricity effects. *Journal of Engineering for Gas Turbines and Power*, 130(1):012510.

[28] Gee, D. and Webb, R. (1980). Forced convection heat transfer in helically rib-roughened tubes. *International Journal of Heat and Mass Transfer*, 23:1127–1136.

[29] Geurts, B. J. and Holm, D. D. (2006). Leray and lans-α modelling of turbulent mixing. *Journal of Turbulence*, (7):N10.

[30] Han, J., Glicksman, L., and Rohsenow, W. (1978). An investigation of heat transfer and friction for rib-roughened surfaces. *International Journal of Heat and Mass Transfer*, 21(8):1143–1156.

[31] Hodkinson, B. (1939). Estimation of the leakage through a labyrinth gland. *Proc. Inst. Mech. Engrs.*, 141:283–288.

[32] Huang, W.-X. and Sung, H. J. (2007). Improvement of mass source/sink for an immersed boundary method. *International journal for numerical methods in fluids*, 53(11):1659–1671.

[33] Hunt, J. C., Wray, A. A., and Moin, P. (1988). Eddies, streams, and convergence zones in turbulent flows.

[34] Hwang, J.-J. (1998). Heat transfer-friction characteristic comparison in rectangular ducts with slit and solid ribs mounted on one wall. *Journal of heat transfer*, 120(3):709–716.

[35] Iacovides, H. and Raisee, M. (1999). Recent progress in the computation of flow and heat transfer in internal cooling passages of turbine blades. *International Journal of Heat and Fluid Flow*, 20(3):320–328.

[36] Jin, R., Chen, W., and Simpson, T. W. (2001). Comparative studies of metamodelling techniques under multiple modelling criteria. *Structural and multidisciplinary optimization*, 23(1):1–13.

[37] Kerr, R. M. and Tucker, P. G. (2005). Mixed nonlinear les for des suitable flows. In *43rd AIAA Aerospace Sciences Meeting and Exhibit*, page 668.

[38] Kim, J., Kim, D., and Choi, H. (2001). An immersed-boundary finite-volume method for simulations of flow in complex geometries. *Journal of Computational Physics*, 171(1):132–150.

[39] Lai, M.-C. and Peskin, C. S. (2000). An immersed boundary method with formal second-order accuracy and reduced numerical viscosity. *Journal of Computational Physics*, 160(2):705–719.

[40] Lakshminarayana, B. (1996). *Fluid Dynamics and Heat Transfer of Turbomachinery*. Wiley Online Library.

[41] Lee, K.-S., Kim, K.-Y., and Samad, A. (2008). Design optimization of low-speed axial flow fan blade with three-dimensional rans analysis. *Journal of mechanical science and technology*, 22(10):1864–1869.

[42] Leonard, A. (1975). Energy cascade in large-eddy simulations of turbulent fluid flows. *Advances in geophysics*, 18:237–248.

[43] Leschziner, M. A. (2002). Turbulence modelling strategies for unsteady flows. *Report on EPSRC visiting fellowship grant*, GR/R04263/01.

[44] Lesieur, M., Bégou, P., Briand, E., Danet, A., Delcayre, F., and Aider, J.-L. (2003). Coherent-vortex dynamics in large-eddy simulations of turbulence. *Journal of turbulence*, 4(016):1–24.

[45] Lesieur, M., Métais, O., and Comte, P. (2005). *Large-eddy simulations of turbulence*. Cambridge University Press.

[46] Lilly, D. K. (1992). A proposed modification of the germano subgrid-scale closure method. *Physics of Fluids A: Fluid Dynamics (1989-1993)*, 4(3):633–635.

[47] Liou, T.-M., Chang, Y., and Hwang, D.-W. (1990). Experimental and computational study of turbulent flows in a channel with two pairs of turbulence promoters in tandem. *Journal of Fluids Engineering*, 112(3):302–310.

[48] Liou, T.-M. and Hwang, J.-J. (1993). Effect of ridge shapes on turbulent heat transfer and friction in a rectangular channel. *International Journal of Heat and Mass Transfer*, 36(4):931–940.

[49] Liu, Y., Tucker, P. G., and Iacono, G. L. (2006). Comparison of zonal rans and les for a non-isothermal ribbed channel flow. *International journal of heat and fluid flow*, 27(3):391–401.

[50] Lockett, J. and Collins, M. W. (1990). Holographic interferometry applied to rib-roughness heat transfer in turbulent flow. *International journal of heat and mass transfer*, 33(11):2439–2449.

[51] Lu, Z., Xie, Y., and Qiu, D. (1992). The finite–difference simulation of flow field in labyrinth seals. *Chinese Journal of Applied Mechanics*.

[52] Michaud, M., Vakili, A., Meganathan, A., Zielke, R., Shuster, L., and Terrell, J. (2003). An experimental study of labyrinth seal flow. In *International Joint Power Generation Conference collocated with TurboExpo 2003*, pages 497–504. American Society of Mechanical Engineers.

[53] Mitchell, M. (1998). *An introduction to genetic algorithms*. MIT press.

[54] Murata, A. and Mochizuki, S. (2000). Large eddy simulation with a dynamic subgrid-scale model of turbulent heat transfer in an orthogonally rotating rectangular duct with transverse rib turbulators. *International Journal of Heat and Mass Transfer*, 43(7):1243–1259.

[55] Murata, A. and Mochizuki, S. (2001). Comparison between laminar and turbulent heat transfer in a stationary square duct with transverse or angled rib turbulators. *International Journal of Heat and Mass Transfer*, 44(6):1127–1141.

[56] Obayashi, S. and Takanashi, S. (1996). Genetic optimization of target pressure distributions for inverse design methods. *AIAA journal*, 34(5):881–886.

[57] Ooi, A., Iaccarino, G., Durbin, P., and Behnia, M. (2002). Reynolds averaged simulation of flow and heat transfer in ribbed ducts. *International Journal of Heat and Fluid Flow*, 23(6):750–757.

[58] Paolillo, R., Wang, C.-Z., Vashist, T., Cloud, D., Bingen, F. M., and Kool, G. A. (2006). Rotating seal rig experiments: test results and analysis modeling. In *ASME Turbo Expo 2006: Power for Land, Sea, and Air*, pages 1551–1559. American Society of Mechanical Engineers.

[59] Patankar, S., Liu, C., and Sparrow, E. (1977). Fully developed flow and heat transfer in ducts having streamwise-periodic variations of cross-sectional area. *Journal of Heat Transfer*, 99(2):180–186.

[60] Patankar, S. V. and Spalding, D. B. (1972). A calculation procedure for heat, mass and momentum transfer in three-dimensional parabolic flows. *International journal of heat and mass transfer*, 15(10):1787–1806.

[61] Peskin, C. S. (1972). *Flow patterns around heart valves: a digital computer method for solving the equations of motion*. UMI.

[62] Pfau, A., Kalfas, A., and Abhari, R. (2007). Making use of labyrinth interaction flow. *Journal of Turbomachinery*, 129(1):164–174.

[63] Pfau, A., Schlienger, J., Rusch, D., Kalfas, A., and Abhari, R. (2005). Unsteady flow interactions within the inlet cavity of a turbine rotor tip labyrinth seal. *Journal of turbomachinery*, 127(4):679–688.

[64] Pfau, A., Treiber, M., Sell, M., and Gyarmathy, G. (2000). Flow interaction from the exit cavity of an axial turbine blade row labyrinth seal. In *ASME Turbo Expo 2000: Power for Land, Sea, and Air*, pages V001T03A051–V001T03A051. American Society of Mechanical Engineers.

[65] Phibel, R., Laroche, E., Casarsa, L., and Arts, T. (2005). Numerical investigation on flow and heat transfer in a ribroughened channel with high blockage ratio. In *6th European Conference on Turbomachinery: Fluid Dynamics and Thermodynamics*.

[66] Pierret, S. (2005). Multi-objective and multi-disciplinary optimization of three-dimensional turbomachinery blades. *Proceedings of the 6th world congresses of structural and multidisciplinary optimization*.

[67] Prakash, C. and Zerkle, R. (1993). Prediction of turbulent flow and heat transfer in a ribbed rectangular duct with and without rotation. In *ASME 1993 International Gas Turbine and Aeroengine Congress and Exposition*, pages V03AT15A057–V03AT15A057. American Society of Mechanical Engineers.

[68] Preece, A. (2008). *An investigation into methods to aid the simulation of turbulent seperation control*. PhD thesis, Warwick.

[69] Ramgadia, A. G. and Saha, A. K. (2012). Large eddy simulation of turbulent flow and heat transfer in a ribbed coolant passage. *Journal of Applied Mathematics*, 2012.

[70] Rau, G., Cakan, M., Moeller, D., and Arts, T. (1996). The effect of periodic ribs on the local aerodynamic and heat transfer performance of a straight cooling channel. In *ASME 1996 International Gas Turbine and Aeroengine Congress and Exhibition*, pages V004T09A061–V004T09A061. American Society of Mechanical Engineers.

[71] Reynolds, O. (1894). On the dynamical theory of incompressible viscous fluids and the determination of the criterion. *Proceedings of the Royal Society of London*, 56(336-339):40–45.

[72] Rhode, D. and Guidry, M. (1993a). A new approach for stabilizing labyrinth seal leakage. *Tribology transactions*, 36(2):219–224.

[73] Rhode, D. and Hibbs, R. (1992). Tooth thickness effect on the performance of gas labyrinth seals. *Journal of tribology*, 114(4):790–795.

[74] Rhode, D., Johnson, J., and Broussard, D. (1997). Flow visualization and leakage measurements of stepped labyrinth seals: Part 1—annular groove. *Journal of turbomachinery*, 119(4):839–843.

[75] Rhode, D., Ko, S., and Morrison, G. (1994). Leakage optimization of labyrinth seals using a navier-stokes code. *Tribology transactions*, 37(1):105–110.

[76] Rhode, D. L. and Adams, R. G. (2004a). Relative axial displacement leakage effects on straight-through labyrinth seals with rub grooves. *40th AIAA/ASME/SAE/ASEE Joint Propulsion Conference and Exhibit,v11-14th July, Fort Lauderdale, Florida, USA, AIAA-2004-3716*.

[77] Rhode, D. L. and Adams, R. G. (2004b). Rub-groove width and depth effects on flow predictions for straight-through labyrinth seals. *Journal of tribology*, 126(4):781–787.

[78] Rhode, D. L. and Allen, B. F. (1998). Visualization and measurements of rub-groove leakage effects on straight-through labyrinth seals. In *ASME 1998 International Gas Turbine and Aeroengine Congress and Exhibition*, pages V004T09A085–V004T09A085. American Society of Mechanical Engineers.

[79] Rhode, D. L. and Allen, B. F. (1999). Measurement and visualization of leakage effects of rounded teeth tips and rub-grooves on stepped labyrinths. In *ASME 1999 International Gas Turbine and Aeroengine Congress and Exhibition*, pages V003T01A092–V003T01A092. American Society of Mechanical Engineers.

[80] Rhode, D. L. and Guidry, M. (1993b). Importance of labyrinth seal through-flow deflection for enlarging clearance without increasing leakage. *Tribology transactions*, 36(3):477–483.

[81] Rigby, D. L. (1998). Prediction of heat and mass transfer in a rotating ribbed coolant passage with a 180 degree turn. In *ASME 1998 International Gas Turbine and Aeroengine Congress and Exhibition*, pages V004T09A065–V004T09A065. American Society of Mechanical Engineers.

[82] Rogallo, R. S. and Moin, P. (1984). Numerical simulation of turbulent flows. *Annual Review of Fluid Mechanics*, 16(1):99–137.

[83] Sagaut, P. (2006). *Large eddy simulation for incompressible flows: an introduction*. Springer Science & Business Media.

[84] Saidi, A. and Sundén, B. (2001). On prediction of thermal-hydraulic characteristics of square-sectioned ribbed cooling ducts. *Journal of turbomachinery*, 123(3):614–620.

[85] Schäfer, M., Turek, S., Durst, F., Krause, E., and Rannacher, R. (1996). *Benchmark computations of laminar flow around a cylinder*. Springer.

[86] Scharrer, J. K. (1987). *A comparison of experimental and theoretical results for labyrinth gas seals*. Texas A & M University, Turbomachinery Laboratories, Mechanical Engineering Department.

[87] Schramm, V., Denecke, J., Kim, S., and Wittig, S. (2004). Shape optimization of a labyrinth seal applying the simulated annealing method. *International Journal of Rotating Machinery*, 10(5):365–371.

[88] Schramm, V., Willenborg, K., Kim, S., and Wittig, S. (2000). Influence of a honeycomb facing on the flow through a stepped labyrinth seal. In *ASME Turbo Expo 2000: Power for Land, Sea, and Air*, pages V003T01A092–V003T01A092. American Society of Mechanical Engineers.

[89] Sewall, E. A. and Tafti, D. K. (2008). Large eddy simulation of flow and heat transfer in the developing flow region of a rotating gas turbine blade internal cooling duct with coriolis and buoyancy forces. *Journal of Turbomachinery*, 130(1):011005.

[90] Sewall, E. A., Tafti, D. K., Graham, A. B., and Thole, K. A. (2006). Experimental validation of large eddy simulations of flow and heat transfer in a stationary ribbed duct. *International journal of heat and fluid flow*, 27(2):243–258.

[91] Smagorinsky, J. (1963). General circulation experiments with the primitive equations: I. the basic experiment*. *Monthly weather review*, 91(3):99–164.

[92] Soto, E. A. and Childs, D. W. (1999). Experimental rotordynamic coefficient results for (a) a labyrinth seal with and without shunt injection and (b) a honeycomb seal. *Journal of Engineering for Gas Turbines and Power*, 121(1):153–159.

[93] Spalart, P., Jou, W., Strelets, M., Allmaras, S., et al. (1997). Comments on the feasibility of les for wings, and on a hybrid rans/les approach. *Advances in DNS/LES*, 1:4–8.

[94] Stocker, H. (1975). Advanced labyrinth seal design performance for high pressure ratio gas turbines. In *ASME 1975 Winter Annual Meeting: GT Papers*, pages V001T01A005–V001T01A005. American Society of Mechanical Engineers.

[95] Stocker, H., Cox, D., and Holle, G. (1977). Aerodynamic performance of conventional and advanced design labyrinth seals with solid-smooth abradable, and honeycomb lands.[gas turbine engines.

[96] Sturgess, G. and Datta, P. (1988). Application of cfd to gas turbine engine secondary flow systems- the labyrinth seal. In *AIAA, ASME, SAE, and ASEE, Joint Propulsion Conference, 24 th, Boston, MA*, page 1988.

[97] Tafti, D. (2005). Evaluating the role of subgrid stress modeling in a ribbed duct for the internal cooling of turbine blades. *International Journal of Heat and Fluid Flow*, 26(1):92–104.

[98] Taslim, M. and Korotky, G. (1997). Low-aspect-ratio rib heat transfer coefficient measurements in a square channel. In *ASME 1997 International Gas Turbine and Aeroengine Congress and Exhibition*, pages V003T09A077–V003T09A077. American Society of Mechanical Engineers.

[99] Taslim, M., Li, T., and Kercher, D. (1994). Experimental heat transfer and friction in channels roughened with angled, v-shaped and discrete ribs on two opposite walls. In *ASME 1994 International Gas Turbine and Aeroengine Congress and Exposition*, pages V004T09A018–V004T09A018. American Society of Mechanical Engineers.

[100] Taslim, M. and Wadsworth, C. (1997). An experimental investigation of the rib surface-averaged heat transfer coefficient in a rib-roughened square passage. *Journal of turbomachinery*, 119(2):381–389.

[101] Taylor, G. I. (1935). Statistical theory of turbulence. In *Proceedings of the Royal Society of London A: Mathematical, Physical and Engineering Sciences*, volume 151, pages 421–444. The Royal Society.

[102] Tennekes, H. and Lumley, J. L. (1972). *A first course in turbulence*. MIT press.

[103] Theil, H. (1992). A rank-invariant method of linear and polynomial regression analysis. In *Henri Theil's Contributions to Economics and Econometrics*, pages 345–381. Springer.

[104] Tseng, Y.-H. and Ferziger, J. H. (2003). A ghost-cell immersed boundary method for flow in complex geometry. *Journal of computational physics*, 192(2):593–623.

[105] Tucker, P., Eastwood, S., Klostermeier, C., Jefferson-Loveday, R., Tyacke, J., and Liu, Y. (2010a). Hybrid les approach for practical turbomachinery flows: part 1—hierarchy and example simulations. In *ASME Turbo Expo 2010: Power for Land, Sea, and Air*, pages 997–1009. American Society of Mechanical Engineers.

[106] Tucker, P., Eastwood, S., Klostermeier, C., Xia, H., Ray, P., Tyacke, J., and Dawes, W. (2010b). Hybrid les approach for practical turbomachinery flows: part 2—further applications. In *ASME Turbo Expo 2010: Power for Land, Sea, and Air*, pages 1055–1067. American Society of Mechanical Engineers.

[107] Tucker, P. and Pan, Z. (2000). A cartesian cut cell method for incompressible viscous flow. *Applied Mathematical Modelling*, 24(8):591–606.

[108] Tucker, P. G. (2001). *Computation of unsteady internal flows: fundamental methods with case studies*. Springer Science & Business Media.

[109] Tyacke, J. (2009). Low reynolds number heat transfer prediction employing large eddy simulation for electronics geometries. *D.Phil. Thesis, Civil and Computational Engineering Centre, Swansea University*.

[110] Tyacke, J., Jefferson-Loveday, R., and Tucker, P. (2013). On the application of les to seal geometries. *Flow, turbulence and combustion*, 91(4):827–848.

[111] Tyacke, J., Jefferson-Loveday, R., and Tucker, P. G. (2011). Application of les to labyrinth seals. In *Proceedings of the AIAA CFD Conference, AIAA Paper no. AIAA-2011-3861*.

[112] Tyacke, J. and Tucker, P. (2012). Les of heat transfer in electronics. *Applied Mathematical Modelling*, 36(7):3112–3133.

[113] Tyacke, J. and Tucker, P. (2015). Large eddy simulation of turbine internal cooling ducts. *Computers & Fluids*, 114:130–140.

[114] Vakili, A., Meganathan, A., Michaud, M., and Radhakrishnan, S. (2005). An experimental and numerical study of labyrinth seal flow. In *ASME Turbo Expo 2005: Power for Land, Sea, and Air*, pages 1121–1128. American Society of Mechanical Engineers.

[115] Van Driest, E. R. (1956). On turbulent flow near a wall. *Journal of the Aeronautical Sciences*.

[116] Vermes, G. (1961). A fluid mechanics approach to the labyrinth seal leakage problem. *Journal of engineering for power*, 83(2):161–169.

[117] Viswanathan, A. K. and Tafti, D. K. (2006). Detached eddy simulation of turbulent flow and heat transfer in a two-pass internal cooling duct. *International Journal of Heat and Fluid Flow*, 27(1):1–20.

[118] Wang, L. and Sundén, B. (2007). Experimental investigation of local heat transfer in a square duct with various-shaped ribs. *Heat and Mass Transfer*, 43(8):759–766.

[119] Waschka, W., Wittig, S., and Kim, S. (1992). Influence of high rotational speeds on the heat transfer and discharge coefficients in labyrinth seals. *Journal of turbomachinery*, 114(2):462–468.

[120] Watson, R. (2013). Large eddy simulation of cutback trailing edges for film cooling turbine blades. *D.Phil. Thesis, Department of Engineering, Cambridge University*.

[121] Watson, R. and Tucker, P. (2016). Perfectly parallel optimization for cutback trailing edges. *AIAA Journal*, pages 1–10.

[122] Webb, R. and Eckert, E. (1972). Application of rough surfaces to heat exchanger design. *International Journal of Heat and Mass Transfer*, 15:1647–1658.

[123] Webb, R., Eckert, E., and Goldstein, R. (1971). Heat transfer and friction in tubes with repeated-rib roughness. *International Journal of Heat and Mass Transfer*, 14(4):601–617.

[124] Wittig, S., Dorr, L., and Kim, S. (1983). Scaling effects on leakage losses in labyrinth seals. *Journal of Engineering for Power*, 105(2):305–309.

[125] Yan, X., Li, J., Song, L., and Feng, Z. (2009). Investigations on the discharge and total temperature increase characteristics of the labyrinth seals with honeycomb and smooth lands. *Journal of Turbomachinery*, 131(4):041009.

[126] Yoshizawa, A. (1993). Bridging between eddy-viscosity-type and second-order turbulence models through a two-scale turbulence theory. *Physical Review E*, 48(1):273.

[127] Yu, Z. and Childs, D. (1995). Experimental rotordynamic coefficient and static characteristic results for a labyrinth rotor running against a grooved stator with l/d= 0.466, c r/r= 0.0036. *Mechanical Engineering Department, Turbomachinery Laboratories, Texas A&M University*.

[128] Yun, G., Choi, H., and Kim, D. (2003). Turbulent flow past a sphere at re= 3700 and 104. *Physics of Fluids (1994-present)*, 15(9):S6–S6.

[129] Zabriskie, W. and Sternlicht, B. (1959). Labyrinth seal leakage analysis. *Journal of Basic Engineering*, 81(3):332–340.

[130] Zimmerman, H., Kammerer, A., and Wolff, K. (1994). Performance of worn labyrinth seals. In *ASME 1994 International Gas Turbine and Aeroengine Congress and Exposition*, pages V001T01A042–V001T01A042. American Society of Mechanical Engineers.

[131] Zimmermann, H. (1990). Some aerodynamic aspects of engine secondary air systems. *Journal of Engineering for Gas Turbines and Power*, 112(2):223–228.

Appendix A

LES Governing Equations

A.1 Filtering Functions

The *LES* governing equations are obtained by means of a filtering operation as follows:

$$\overline{\phi}(x,t) = \int_{-\infty}^{\infty} G(x,x',\Delta)\phi(x',t)dx' \tag{A.1}$$

where $\overline{\phi}$ is the filtered function, ϕ is the original function. Here the overbar indicates spatial filtering, not time–averaging. Δ is the corresponding filter width, which is taken as an indicative measure of the size of eddies.

The scale separation is illustrated in Figure A.1. k_c is the cutoff wave number to separate eddies with resolved and unresolved scales, and can be expressed as $k_c = \pi/\Delta$.

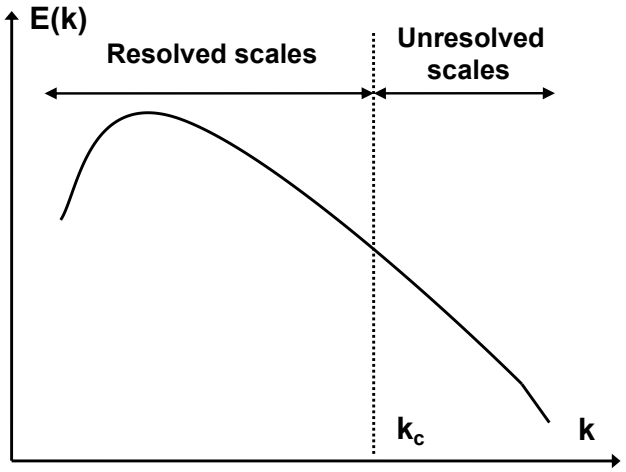

Fig. A.1 Energy spectrum.

A.2 Filtered Governing Equations

For incompressible flow with constant viscosity, the following governing equations can be obtained by applying a filtering operation:

$$\frac{\partial \overline{u}_j}{\partial x_j} = 0 \tag{A.2}$$

$$\rho \frac{\partial \overline{u}_i}{\partial t} + \rho \frac{\partial \overline{u_i u_j}}{\partial x_j} = -\frac{\partial \overline{p}}{\partial x_i} + \frac{\partial}{\partial x_j}[\mu \frac{\partial \overline{u}_i}{\partial x_j}] \tag{A.3}$$

$$\rho \frac{\partial \overline{T}}{\partial t} + \rho \frac{\partial \overline{u_j t}}{\partial x_j} = \frac{\partial}{\partial x_j}[\frac{\mu}{Pr} \frac{\partial \overline{T}}{\partial x_j}] \tag{A.4}$$

The velocities can be divided into the filtered and fluctuating parts: $u_i = \overline{u}_i + u'_i$, as suggested by Leonard [42]. The non–linear term $u_i u_j$ in Eq. (A.3) can be rearranged as:

$$\begin{aligned} \overline{u_i u_j} &= \overline{(\overline{u}_i + u'_i)(\overline{u}_j + u'_j)} \\ &= \overline{\overline{u}_i \overline{u}_j} + \overline{\overline{u}_i u'_j} + \overline{\overline{u}_j u'_i} + \overline{u'_i u'_j} \\ &= \overline{\overline{u}_i \overline{u}_j} - \overline{u}_i \overline{u}_j + \overline{u}_i \overline{u}_j + \overline{\overline{u}_i u'_j} + \overline{\overline{u}_j u'_i} + \overline{u'_i u'_j} \end{aligned} \tag{A.5}$$

which reflects interactions between the stress tensor and subgrid scales. Substituting Eq. (A.5) into Eq. (A.3) results in the equation

$$\rho \frac{\partial \overline{u}_i}{\partial t} + \rho \frac{\partial \overline{u_i u_j}}{\partial x_j} = -\frac{\partial \overline{p}}{\partial x_i} + \frac{\partial}{\partial x_j}[\mu \frac{\partial \overline{u}_i}{\partial x_j}] - \rho \frac{\partial \tau_{ij}}{\partial x_j} \tag{A.6}$$

where

$$\tau_{ij} = \overline{u_i u_j} - \overline{u}_i \overline{u}_j \tag{A.7}$$

τ_{ij} is the subgrid–scale stress tensor and is attributable to convective momentum transport due to interactions between the unresolved or *SGS* eddies, these stresses are commonly termed the sub–grid–scale stresses.

In a similar manner, the governing equation for temperature can be expressed as

$$\rho \frac{\partial \overline{T}}{\partial t} + \rho \frac{\partial \overline{u}_j \overline{T}}{\partial x_j} = \frac{\partial}{\partial x_j}[\frac{\mu}{Pr} \frac{\partial \overline{T}}{\partial x_j}] - \rho \frac{\partial h_j}{\partial x_j} \tag{A.8}$$

where h_j is the sub–grid scale heat flux and has the form

$$h_j = \overline{u_j t} - \overline{u}_j \, \overline{T} \tag{A.9}$$

It is τ_{ij} and h_j that need to be modelled.

Appendix B

Effects of Clearance Size

Figure B.1 compares the axial velocity between seals with different clearances.

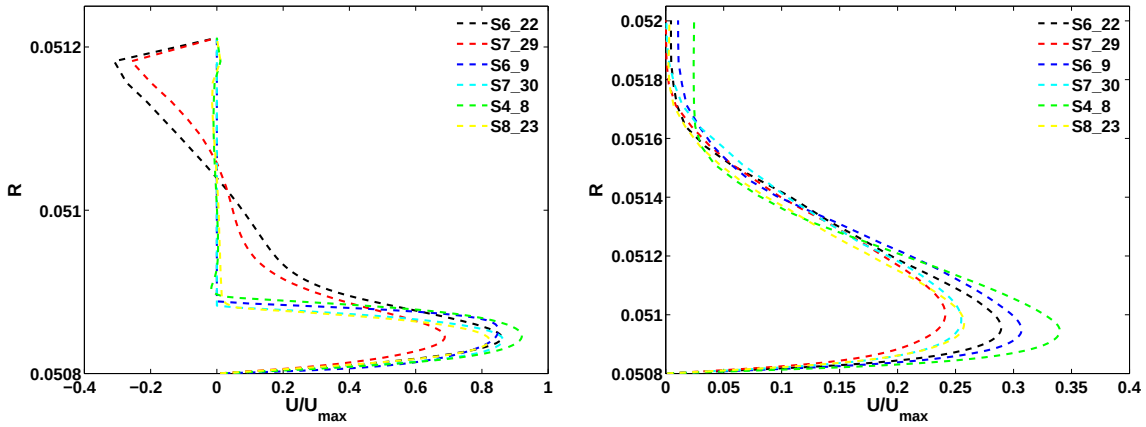

(Profile A) **(Profile B)**

Fig. B.1 Axial velocity profiles between seals with different clearances.